Vniversitat de València

Departament de Física Aplicada i Electromagnetisme

Doctoral Programme in Physics

Whispering Gallery Modes:
Advanced Photonic Applications

Doctoral Thesis

Xavier Roselló Mechó

Valencia, May 2019

Supervisors:

Prof. Miguel V. Andrés Bou
Dr. Martina Delgado Pinar

Dr. Miguel V. ANDRÉS BOU, Catedrático de Física Aplicada y Electromagnetismo, y Dra. Martina DELGADO PINAR, Profesora Asociada del Departamento de Física Aplicada y Electromagnetismo, ambos de la Universitat de València

CERTIFICAN que la presente memoria *"Whispering Gallery Modes: Advanced Photonic Applications"* resume el trabajo de investigación realizado bajo su dirección, por D. Xavier ROSELLÓ MECHÓ y constituye su Tesis para optar al Grado de Doctor en Físicas.

Y para que conste y en cumplimiento de la legislación vigente, firman el presente certificado en Valencia a

Fdo. Dr. Miguel V. Andrés Bou **Fdo. Dra. Martina Delgado Pinar**

Abstract

Whispering Gallery Modes (WGMs) based microresonators have attracted a great interest in the last decades due to their strong confinement of the light. Such microresonators can be fabricated with different geometries and materials. They exhibit high Q-factors and small mode volumes, which allows a great number of fundamental studies and applications, as for example the study of nonlinear phenomena. The narrow linewidths that the WGM resonances present enable the measurement of small perturbations of the microresonator parameters, with a low detection limit.

This thesis provides an experimental characterization of the properties of different optical fiber devices by means of WGMs. The operational principle is based on exploiting the tunability of the WGM resonances by means of variations in the parameters that define the material and the geometry of the microresonators. This feature enables the study of the microresonator properties by measuring the optical spectral position of the WGM resonances. The variation of the microresonator's parameters can be induced by strain, a temperature change, or an external magnetic field. The characterization of the strain-optic effect in silica and PMMA axially stretched optical fibers allowed the determination of the strain-optic coefficients of both materials. Commonly, an axial strain generates a uniaxial anisotropy that can be measured directly with our approach. Analogously, the characterization of the thermo-optic effect in different optical fiber

devices, illuminated with different optical signals, enables the measurement of a variety of parameters: the contributions of absorption and scattering to the loss coefficient in UV-irradiated photosensitive fibers, thermal profiles in long period gratings, and the heating induced optically in active doped fibers. The main features of the implemented experimental technique are its low detection limit, its spatial resolution, and its capability to perform the measurements in a broad range of optical wavelengths.

Locking techniques are necessary in experiments involving WGMs, to generate stable, nonlinear phenomena. This work provides two novel active locking techniques to stabilize the system at constant laser wavelength, which were experimentally tested. Both of them are based on the tuning of the spectral position of the WGM resonances either by means of axial strain, or temperature variations of the microresonators. Finally, optomechanical phenomena are a nonlinear effect induced by the high optical circulating power of the WGM, which results in the excitation of the acoustic modes of a microresonator. Vibrational resonant modes with high mechanical Q-factors were identified and characterized in bubble microresonators, and it was observed the transition to a chaotic behavior of this system, as the circulating power was increased.

Acknowledgements

I would like to thank all the people that contributed to this thesis. First, I would like to thank Dr. Miguel V. Andrés for the support and guidance that he has provided me, from my time as a student, to these last years as a researcher. I would also like to thank Dr. Martina Delgado Pinar for all her help and supervision throughout this work, and for her teachings in the experimental techniques that I employed in this thesis. They always showed patience and dedicated time to solve and discuss my countless doubts and questions. I am sincerely grateful to both of them. I also owe many thanks to Dr. Antonio Díez and Dr. José Luis Cruz for their help and good advices. In the course of this thesis, I enjoyed working with a lot of people, thanks to Erica, Javi, Iván, Abraham, Saúl, Luis, Tomás, Manuel, Diego, and to all those I am not naming but spent some time with me during these years. I am specially grateful to Antonio Carrascosa, Emmanuel, Lorena, Martina, Luis and Nathália. It was a pleasure to share conversations and travels to conferences with all of them. I would also want to thank the people that I met during my stay in Florence: Dr. Gualtiero Nunzi Conti for providing me great insights, Gabriele, Alberto, and specially Dr. Silvia Soria for her supervision and her help during my four months in Italy.

I would like to thank the Ministerio de Economía y Competitividad for the FPI contract that I enjoyed during the last four years and that allowed me to develop this thesis.

Finalment, també m'agradaria agrair a totes les persones que no estan relacionades directament amb aquesta tesi però han fet que aquests anys de treball siguen més feliços. Als meus amics, pels molts moments de diversió i per fer-me desconnectar d'aquest treball que moltes vegades t'acompanya a casa, i, sobretot, a la meua família per la seua ajuda i confiança incondicional durant tots aquests anys.

Contents

Resumen en español

Objetivos de la tesis

La implementación de micro-cavidades ópticas se ha extendido en las últimas décadas, teniendo un papel fundamental en aplicaciones de fotónica, tanto en investigación teórica como aplicada. Algunos ejemplos son: fabricación de fuentes láser, diseño de filtros dinámicos, diseño de sensores, estudio de fenómenos no-lineales, entre otros. El principio operacional de las micro-cavidades se basa en confinar la luz dentro de su estructura a través del fenómeno de resonancia. Las cavidades se pueden diferenciar dependiendo de su mecanismo de confinamiento: las cavidades Fabry-Perot o los cristales fotónicos son dos ejemplos. Otra familia de estas micro-cavidades ópticas son las basadas en ondas electromagnéticas superficiales, conocidas como *Whispering Gallery Modes (WGMs)* debido a su análogo acústico, que fue descrito por Rayleigh a finales del siglo XIX.

Los *WGMs* son ondas superficiales que se propagan ligadas a la interfase de micro-cavidades con simetría circular. La luz circula en dirección azimutal en la superficie interior de la cavidad óptica, quedando confinada por reflexión total interna. Estos modos superficiales interfieren con ellos mismos dando lugar a resonancias a longitudes de onda ópticas determinadas por la geometría, tamaño y material de la micro-cavidad. Estas micro-cavidades presentan varias ventajas comparadas con las cavidades Fabry-Perot o los cristales fotónicos. De entre ellas destacan la miniaturización, la sencillez de fabricación, su bajo coste, su fácil integración en circuitos fotónicos, etc. Además, pueden ser fabricadas con distintas geometrías: cilíndrica, esférica, o toroidal, siendo posible utilizar diferentes materiales con baja absorción para su fabricación, lo que permite obtener resonancias de gran calidad. Algunos ejemplos de estos materiales son: polímeros, materiales cristalinos, o, el más usual, la sílice.

Se han desarrollado a lo largo de los últimos años diferentes aplicaciones basadas en micro-cavidades *WGMs*, entre las que destacan: filtros fotónicos sintonizables a partir de la aplicación de tensión mecánica o de un incremento de la temperatura de la micro-cavidad; biosensores de onda evanescente; medida de las propiedades del material de la micro-cavidad; etc. Todas estas aplicaciones son posibles gracias al alto factor de calidad, Q, que presentan las resonancias en micro-resonadores ópticos basados en *WGMs*. Este alto valor de Q, junto con volúmenes modales muy pequeños, convierten a estos micro-resonadores en candidatos óptimos para el diseño de láseres con umbrales de potencia bajos, y para el estudio de fenómenos no-lineales a baja potencia.

En el marco actual de investigación de micro-cavidades ópticas basadas en *WGMs*, los objetivos de esta tesis se pueden diferenciar en dos bloques: el desarrollo de nuevas técnicas para el estudio y caracterización de distintos dispositivos basados en fibras ópticas, y la excitación y observación de efectos no-lineales en micro-resonadores fabricados en sílice.

El primer bloque engloba tanto el estudio teórico y diseño de los dispositivos a analizar, como las técnicas de medida que permiten la caracterización de los mismos. Entre los objetivos específicos destacan (i) la caracterización de micro-resonadores cilíndricos constituidos por secciones de fibras ópticas con propiedades especiales: fibras de sílice dopadas, fibras irradiadas con luz ultravioleta y fibras de polímero PMMA; (ii) los micro-resonadores fabricados con polímeros mediante la técnica de fotopolimerización de dos fotones; y (iii) la caracterización de componentes de fibra óptica como son las redes de periodo largo. El principio que permite usar los *WGMs* como técnica de caracterización de los diferentes dispositivos mencionados es la dependencia de las resonancias *WGM* con los parámetros que definen el material y la geometría de los micro-resonadores. Este hecho abre la posibilidad de extraer información de los mismos a partir de la medida de las longitudes de onda de resonancia cuando dichos parámetros experimentan algún cambio. Las características que presentan las resonancias *WGMs* permiten una medida de los parámetros caracterizados con una alta precisión, así como la observación de comportamientos inducidos por distintos efectos, el efecto elasto-óptico y el termo-óptico por ejemplo, que no es posible con otras técnicas de medida más convencionales.

El segundo bloque se centra principalmente en el desarrollo de técnicas experimentales de estabilización de las resonancias *WGM*, las cuales permiten resolver los problemas que surgen al intentar sintonizar la longitud de onda de emisión del láser que excita el *WGM*, con la longitud de onda de resonancia. Estas técnicas de estabilización son conocidas en la bibliografía como técnicas de *locking*, y se dividen en técnicas pasivas y activas. Uno de los objetivos ha sido la descripción y caracterización de los efectos no-lineales térmicos que se inducen durante el proceso de sintonización del laser con una resonancia *WGM*. A partir del estudio de estas no-linealidades térmicas, se ha implementado un *locking* pasivo basado en este efecto no-lineal. Además, aprovechando el estudio de los efectos elasto-óptico y termo-óptico, se han desarrollado técnicas novedosas de *locking* activo, las cuales permiten trabajar a una longitud de onda de emisión del láser constante. El desarrollo de estas técnicas de *locking* permite llevar a cabo diferentes experimentos centrados en el estudio de efectos no-lineales en micro-resonadores *WGM*. Las grandes densidades de energía confinada en los micro-resonadores permiten la observación de efectos no-lineales, tanto ópticos como opto-mecánicos, para potencias de bombeo láser relativamente bajas. Como último objetivo de las tesis, se han caracterizado las vibraciones mecánicas inducidas por los *WGMs* en micro-resonadores de sílice con geometría esférica, centrándonos en cavidades con forma de burbuja.

Fundamentos teóricos de los *WGMs*

Los micro-resonadores basados en *WGMs* son estructuras con simetría rotacional, generalmente formados por un material dieléctrico. Aunque los materiales más empleados son isótropos, como por ejemplo la sílice o los polímeros, existen micro-resonadores fabricados a partir de materiales con cierta anisotropía. Además, es posible inducir una anisotropía en un material isótropo mediante diferentes mecanismos. Así pues, en este trabajo se ha llevado a cabo una descripción teórica de la propagación de los *WGMs* en micro-resonadores cilíndricos con diversas anisotropías, con el fin de describir los diferentes efectos estudiados a lo largo de la tesis.

De los distintos modos de propagación existentes en este tipo de estructuras, entre los que se incluyen los modos de propagación convencionales de las fibras ópticas, el estudio se ha basado en las ondas que se propagan puramente en dirección azimutal, es decir, los *WGMs*. Las propiedades de los modos ópticos guiados por reflexión total interna se han calculado resolviendo las ecuaciones de Maxwell e incluyendo las distintas anisotropías en la forma del tensor permitividad. Se han estudiado dos casos de especial interés, una anisotropía uniaxial, y una girotrópica, las cuales describen el comportamiento de los *WGMs* cuando los micro-resonadores están sometidos al efecto elasto-óptico y al magneto-óptico.

Debido a la simetría cilíndrica de la estructura, las soluciones de los campos a las ecuaciones de Maxwell son separables en dos funciones, una dependiente de la coordenada azimutal, y otra de la coordenada radial. No hay dependencia con la coordenada axial ya que a lo largo del desarrollo teórico se ha asumido que la estructura cilíndrica es infinitamente larga. La parte angular debe satisfacer que el campo electromagnético confinado interfiera constructivamente con él mismo después de cada vuelta dentro del micro-resonador, lo que confiere el carácter resonante a este tipo de modos. En consecuencia, el valor de la constante de propagación de los modos queda discretizado. De hecho, cada modo queda inequivocamente identificado por una serie de números enteros, que tradicionalmente se conocen como los órdenes azimutales y radiales. Respecto la parte radial, la solución es una combinación de funciones de Bessel que debe cumplir una serie de condiciones de contorno para tener significado físico. Teniendo en cuenta las soluciones de la función angular y radial, se obtiene el campo electromagnético de los *WGMs* al completo.

Aplicando las condiciones de contorno al campo electromagnético en la interfase de los dos medios tratados, se llega a la obtención de dos ecuaciones características, referentes a cada una de las polarizaciones de los *WGMs*. De esta manera, cada modo, representado por sus órdenes azimutal y radial, tiene a su vez dos modos de polarización, TE y TM. La forma de las ecuaciones características depende del tipo de anisotropía considerada en el tensor permitividad. En cualquiera de los casos, la solución a estas viene dada por las longitudes de onda de resonancia de los *WGMs*. Las soluciones consisten en una serie discreta de longitudes de onda cuyo valor está determinado por el orden azimutal y radial de las resonancias.

Las curvas de dispersión de las resonancias *WGM* son diferentes a las que normalmente se obtiene para los modos convencionales de una fibra óptica. Además del comportamiento discretizado de las soluciones, en este tipo de modos se estudia cómo varía la longitud de onda de resonancia de los *WGMs* en función del orden azimutal y radial de los modos. A medida que ambos órdenes aumentan, la longitud de onda de resonancia de los modos disminuye. Respecto al índice efectivo de los *WGMs*, este muestra una variación suave con el orden azimutal, mientras que el cambio entre órdenes radiales es significativo.

El campo electromagnético de los *WGMs* se encuentra fuertemente confinado en la interfase para los micro-resonadores caracterizados a lo largo de esta tesis: a mayor tamaño, mayor confinamiento. En general, el orden azimutal dicta el número de oscilaciones que sufre el campo a lo largo del perímetro del micro-resonador, mientas que el orden radial provee información respecto al número de oscilaciones del campo en el interior del resonador en la dirección radial: para órdenes radiales bajos el campo está más confinado. En el medio exterior del micro-resonador, generalmente aire, el campo se describe como una onda evanescente que radia hacia el infinito.

En esta tesis se ha llevado a cabo el estudio de uno de los parámetros que describen el rendimiento de cualquier resonador, su factor de calidad, así como las distintas fuentes de pérdidas que presentan este tipo de micro-resonadores. De los distintos tipos que existen, tanto intrínsecas a la cavidad como fuentes externas, únicamente dos de ellas, en condiciones experimentales, son limitantes del valor de Q: las pérdidas que se inducen al acoplar la luz al micro-resonador, y los contaminantes superficiales. Estas fuentes de pérdidas limitan el valor de Q a $\sim 10^8 - 10^9$, en estructuras de sílice. Estos valores son extremadamente altos comparados con otros resonadores electromagnéticos, y es el parámetro clave que permite obtener gran precisión en las medidas realizadas usando *WGMs*.

Por último, en la parte teórica, se ha estudiado el acoplamiento de energía desde una micro-fibra a un micro-resonador, configuración que ha sido empleada experimentalmente a lo largo de todo el trabajo. La cola evanescente del campo electromagnético de una micro-fibra dispuesta cerca de un micro-resonador es capaz de excitar sus modos *WGM*. Además, la existencia de pequeñas inhomogeneidades en la superficie de la cavidad permiten la excitación de *WGMs* contra-propagantes que se re-acoplan a la micro-fibra con sentido opuesto al campo inicial y, por lo tanto, permiten realizar medidas tanto en transmisión como en reflexión. La eficiencia del acoplamiento depende de las pérdidas intrínsecas del micro-resonador y de la distancia relativa entre ambas estructuras. En el caso ideal en el que no existen inhomogeneidades en la superficie, el acoplamiento crítico se da cuando las pérdidas del micro-resonador son iguales a la energía acoplada.

Procedimientos experimentales

A lo largo de la tesis, se ha usado un montaje experimental básico para excitar y medir los *WGMs* que, en función del efecto concreto que se ha querido caracterizar, se modificaba convenientemente.

Este montaje común consta de, en primer lugar, una fuente de luz, generalmente un láser sintonizable, que se emplea para excitar las resonancias. El láser incorpora un sistema de barrido en longitud de onda basado en un piezoeléctrico que permite realizar un barrido continúo con una resolución dada por la anchura de línea del láser ($< 300\,\mathrm{kHz}$). El barrido se controla con una señal triangular externa suministrada por un generador de funciones de frecuencia y amplitud variable. Un controlador de polarización situado después del láser permite seleccionar la polarización de la luz emitida. En algunos experimentos con microresonadores que presentan factores de calidad demasiado bajos para la técnica descrita, se han utilizado fuentes de luz de banda ancha como sustituto del láser sintonizable.

Con el fin de acoplar la luz al micro-resonador, la señal óptica se inyecta en una micro-fibra auxiliar de unas 2 μm de diámetro, colocada perpendicularmente al micro-resonador. La posición relativa entre la micro-fibra y el micro-resonador se controla mediante un sistema de posicionamiento que permite seleccionar, por un lado, la distancia relativa entre ellos. En la mayoría de experimentos, sin embargo, se trabaja con ambos elementos en contacto. En segundo lugar, el sistema permite también controlar el punto del micro-resonador al cual se acerca la microfibra: de esta manera, se pueden hacer medidas en diferentes puntos del microresonador. Las micro-fibras empleadas para la excitación de los *WGMs* se fabrican empleando el equipo de post-procesado por fusión y estrechamiento disponible en el grupo de investigación de fibras ópticas de la Universidad de Valencia. Los parámetros típicos de las micro-fibras utilizadas en la mayoría de experimentos son: 2 μm de diámetro de cuello y 6 mm de longitud.

La señal transmitida a la salida de la micro-fibra se monitoriza con un fotodiodo conectado a un osciloscopio, que está sincronizado con la señal eléctrica del generador de funciones. Utilizando un circulador situado antes de la micro-fibra, es posible medir de igual forma la señal reflejada. Las trazas temporales obtenidas en el osciloscopio son en la práctica, espectros en longitud de onda de las resonancias *WGM*

Respecto a los micro-resonadores, dependiendo del experimento, el material o la geometría se ha ido variando. En los experimentos de caracterización de propiedades de fibras, o de distintos dispositivos fabricados en fibra óptica, la propia fibra actuaba como micro-resonador. En algunos casos, la fibra se estrechó ligeramente utilizando el equipo de fusión y estiramiento para suavizar la superficie del micro-resonador y así aumentar el factor de calidad. Además de los micro-resonadores cilíndricos de sílice, con factores Q entre 10^6 y 10^7, se han caracterizado otras micro-cavidades fabricadas a partir de polímeros: micro-resonadores cilíndricos de PMMA, y estructuras vasiformes fabricadas con un método de fotopolimerización con dos fotones. En la última parte de la tesis, también se han utilizado micro-cavidades esféricas de sílice: esferas y burbujas, para excitar los *WGMs*. Por tanto, este montaje es capaz de excitar y medir *WGMs* en distintos materiales y geometrías.

Resultados

Efecto magneto-óptico

Cuando un micro-resonador cilíndrico fabricado con un material dieléctrico e isótropo se somete a un campo magnético externo constante orientado a lo largo de su dirección axial, se induce una anisotropía girotrópica en el material, que será tanto más pronunciada como alta sea su constante de Verdet. A partir del desarrollo teórico de la propagación de los *WGMs* en micro-resonadores con este tipo de anisotropía, se ha estudiado la variación de la posición espectral de las resonancias *WGM* en función de la intensidad del campo magnético. De este desarrollo teórico se ha concluido que solo la polarización TE se ve afectada por la presencia del campo externo, mientras que la polarización TM se comporta como lo haría en el caso de un material isótropo. Las resonancias de la polarización TE experimentan un desplazamiento en su longitud de onda hacia longitudes de onda cortas o largas dependiendo del sentido de propagación de los *WGMs*: en la dirección azimutal, horario o anti-horario. Desde un punto de vista experimental, el sentido de propagación de los modos está determinado en función de si es un WGM propagante o contra-propagante.

En micro-resonadores fabricados con sílice, las simulaciones predicen que el desplazamiento que sufren las resonancias *WGM* para un campo magnético externo de $1\,\mathrm{T}$ es mucho más pequeño que la anchura de línea típica que presentan, debido al pequeño valor de la constante de Verdet de este material. Así pues, la resolución de la técnica no permite, con el montaje de que disponemos, medir experimentalmente este efecto en este tipo de materiales por medio de resonancias *WGM*. Sin embargo, existen materiales dieléctricos que presentan una constante de Verdet ~ 57 veces superior a la del sílice, lo que abre la posibilidad de medir este efecto si se dispusiera del micro-resonador adecuado. Además, midiendo el desplazamiento relativo entre dos *WGMs* contra-propagantes entre sí, el desplazamiento inducido por el campo externo se duplica, lo que facilitaría la medida del efecto. Desafortunadamente, micro-resonadores fabricados con materiales con una contante de Verdet alta no estaban disponibles durante la realización de esta tesis. En todo caso, hemos proporcionado las herramientas teóricas necesarias para predecir los cambios en la respuesta espectral de los *WGMs* que induciría este efecto.

Efecto elasto-óptico

Cuando un micro-resonador cilíndrico e isótropo sufre un estiramiento axial se induce una anisotropía uniaxial en el tensor permitividad debido al efecto elasto-óptico, la cual varía dependiendo del material. En un micro-resonador de sílice, las simulaciones predicen que se induce una fuerte anisotropía y que afecta de forma distinta a cada una de las polarizaciones, debido a los coeficientes elasto-ópticos de la sílice. Esto, junto con una variación del tamaño del micro-resonador, provoca un desplazamiento espectral de las resonancias *WGM* al aplicar una tensión axial. El desplazamiento afecta en mayor medida a las resonancias TE que a las TM: las primeras experimentan un corrimiento hacia al azul ~ 1.66 veces mayor que las últimas.

Hemos observado este comportamiento experimentalmente, excitando las dos polarizaciones de los *WGMs* de un micro-resonador cilíndrico de sílice (en nuestro caso, una sección de fibra óptica convencional) y midiendo su respuesta espectral cuando la fibra se somete a una deformación axial. Esta técnica basada en los *WGMs*, además de posibilitar la observación del comportamiento anisótropo del material, permite la medida y determinación de los coeficientes elasto-ópticos del medio caracterizado. En el caso de la sílice, los coeficientes obtenidos fueron: $p_{11} = 0.116$ y $p_{12} = 0.255$ a $1531\,\mathrm{nm}$, valores que son compatibles con los presentados anteriormente en la bibliografía. Hasta donde sabemos, esta es la primera vez que se ha observado la respuesta anisótropa de las resonancias *WGM* inducida por tensión axial en fibras ópticas, lo que ha permitido proponer un nuevo método experimental de medida de los coeficientes elasto-ópticos en estos sistemas. La novedad de este resultado radica en que los modos ópticos convencionales, que se propagan axialmente en las fibras, son esencialmente transversales a la dirección de propagación, y por tanto, no son sensibles a las variaciones que experimenta el tensor permitividad en esta dirección debido a tensiones axiales. Por otro lado, otra de las grandes ventajas de esta técnica es la posibilidad de determinar con facilidad los coeficientes elasto-ópticos a diferentes longitudes de onda, siempre que el material presente pocas pérdidas. Esta característica ha sido empleada para medir la dispersión de los coeficientes elasto-ópticos de la sílice a 1064 y 1531 nm, y los resultados muestran que presentan una respuesta plana.

Aprovechando la técnica de medida, y la posibilidad de excitar eficientemente las resonancias *WGM* en micro-resonadores fabricados con polímeros, se ha llevado a cabo una caracterización para determinar los coeficientes elasto-ópticos del PMMA. La medida se ha realizado para el rango del infrarrojo cercano, entre 800 y 2000 nm. Como en el caso de la sílice, la respuesta de la dispersión de los coeficientes ha sido plana. Los valores de los coeficientes obtenidos en todo el rango son compatibles con los publicados previamente para 633 nm. La medida en todo el rango de infrarrojo cercano es de alto interés debido al gran número de aplicaciones de diseño de sensores de tensión en 1550 nm basados en dispositivos fabricados con este material. Hasta donde sabemos, esta es la primera vez que se miden los coeficientes elasto-ópticos del PMMA en un rango de longitudes de onda tan amplio.

Efecto termo-óptico

Cuando un micro-resonador experimenta una variación de temperatura, se induce una variación en su índice de refracción que viene determinada por el efecto termo-óptico en ese material. A diferencia del efecto elasto-óptico, el cambio que se induce no introduce ninguna anisotropía en el tensor permitividad. Esta variación del índice de refracción, y la consecuente expansión térmica de la cavidad provocan un desplazamiento hacia el rojo de las resonancias *WGM*, en el caso de un calentamiento. A partir de la medida de este desplazamiento espectral, es posible cuantificar el incremento de temperatura en el material.

Se ha estudiado el calentamiento en distintos dispositivos basados en fibra óptica, bombeando el núcleo dopado de la fibra. La potencia absorbida de las señales de bombeo, típicamente de $\sim$ 1 W, se transforma en calor por procesos de relajación no-radiativos. Dependiendo del dopante, la fracción de potencia absorbida convertida en calor varía, siendo del 100% para fibras no-activas. La técnica de medida, se basa en analizar el desplazamiento de las resonancias *WGM* debido al incremento de temperatura, y presenta un límite de detección bajo, $\sim 0.03\,^{\circ}$C, además de una resolución axial de ~ 200 µm. Esta última propiedad es importante ya que permite caracterizar los perfiles térmicos de fibras irradiadas, redes de periodo largo y fibras activas, a lo largo del dispositivo.

En un primer estudio, se midieron los cambios en el coeficiente de absorción en fibras fotosensibles tras ser irradiadas con luz ultravioleta (UV). Cuando este tipo de fibras son irradiadas con luz UV, se induce una variación en el índice de refracción del núcleo de la fibra, que es el proceso clave que permite la fabricación de dispositivos tan extendidos en los sistemas de comunicación actual como son las redes de Bragg y de periodo largo. Además, debido a la altas potencias de irradiación, se generan cambios estructurales como consecuencia de la densificación del material. Estos dos efectos provocan que las pérdidas totales de la fibra irradiada, tanto la absorción como el *scattering*, aumenten. Dado el interés tecnológico de los dispositivos fabricados mediante este método, es importante disponer de una técnica que permita cuantificar este aumento. Iluminando el núcleo de la fibra irradiada, y midiendo el consecuente desplazamiento de las resonancias *WGM*, es posible calcular el incremento de la absorción a partir de un sencillo modelo de distribución del calor en la fibra. En esta sección hemos combinado esta caracterización con la medida convencional de las pérdidas totales introducidas durante el proceso de irradiación UV, y hemos sido capaces de discriminar la contribución de la absorción y el *scattering* a las pérdidas totales. Este proceso se ha llevado a cabo para varias fibras fotosensibles, tanto comerciales como hidrogenadas en nuestro laboratorio, con diferentes dopantes y concentraciones. En todas ellas se ha observado un incremento significativo de la absorción. Además, hemos podido concluir que las pérdidas por *scattering* crecen más rápido que las de absorción en el proceso de irradiación UV.

En segundo lugar, se ha estudiado el perfil de temperatura inducido en redes de periodo largo cuando se las ilumina con una señal de potencia moderada, a diferentes longitudes de onda. En este caso, se han observado perfiles de temperatura no constantes a lo largo de la dirección axial. El gradiente de temperatura depende de la fracción de luz guiada por el modo fundamental en cada punto. El láser de iluminación se sintonizó en diferentes posiciones espectrales dentro del ancho de banda del pico de atenuación de la de la red de periodo largo, de esta manera se controlaba la proporción de luz guiada por el modo fundamental y el modo de la cubierta. Ya que la variación en la absorción se genera principalmente en el núcleo durante la irradiación, y puesto que solo un 2% de la intensidad del modo de la cubierta de nuestro experimento está localizada en el núcleo, la fracción de luz guiada por el modo fundamental (confinado en el núcleo) es la responsable del calentamiento. Estos perfiles de temperatura pueden llegar a afectar las propiedades espectrales de sistemas de alta potencia en fibra óptica que incluyan redes de periodo largo en su configuración.

Por último, se ha estudiado el calentamiento que sufren fibras activas co-dopadas con holmio e iterbio al ser bombeadas dentro de su banda de absorción. Estas fibras son de interés porque se emplean en la fabricación de láseres en fibra óptica con longitudes de onda de emisión por encima de las $2\,\mu\text{m}$, lo cual es un tema de interés en la actualidad. Se ha estudiado el calentamiento que experimentan cuando se iluminan con bombeos a dos longitudes de onda diferentes, dentro de la banda de absorción de estos dopantes. La caracterización se ha realizado en función de la concentración de dopante, y de los dopantes empleados. Mientras que las fibras dopadas únicamente con holmio sufren un calentamiento proporcional a la concentración de dopante, cuando las fibras son co-dopadas con iterbio para poder utilizar la banda de absorción de este último en $980\,\text{nm}$ (en la que se dispone de mayor variedad de láseres de bombeo económicos), se alcanzan temperaturas significativamente altas, que pueden llegar a ser críticas para el correcto funcionamiento de estos dispositivos integrados en cavidades láser.

Técnicas de *locking* y aplicaciones

Para excitar efectos ópticos no-lineales en micro-resonadores basados en resonancias *WGM*, es necesario que la longitud de onda de emisión del láser y de la resonancia *WGM* mantengan su posición espectral relativa constante, es decir, que permanezcan sintonizadas la una con la otra durante intervalos temporales amplios. En caso contrario, el acoplamiento de energía al micro-resonador puede fluctuar, haciendo imposible la excitación de efectos no-lineales de forma estable. Durante el proceso de sintonización, se inducen efectos térmicos no-lineales debido a que la energía que circula en micro-resonadores con Q alta alcanza valores muy elevados. Dependiendo del sentido del barrido del láser, hacia longitudes de onda largas o cortas, se observa un ensanchamiento o estrechamiento, respectivamente, de la forma espectral de la resonancia *WGM*.

Existen diferentes técnicas que permiten estabilizar la posición relativa del láser y la resonancia, y así compensar los efectos térmicos no-lineales y las posibles perturbaciones externas. En este trabajo, se han implementado técnicas de *locking* tanto pasivas como activas. En particular, se proponen dos técnicas activas novedosas, basadas en los efectos elasto- y termo-óptico.

En primer lugar, se ha estudiado el comportamiento dinámico de los *WGMs* cuando se excitan con un láser barriendo un cierto rango espectral que incluye la resonancia, tanto hacia longitudes de onda mayores, como menores. A partir de la descripción teórica, se ha desarrollado la implementación de una técnica pasiva de *locking* en la cual el láser se detiene durante el barrido al llegar a una cierta longitud de onda en la que se alcanza un régimen térmico meta-estable. Cuando el sistema se encuentra en este régimen operacional, el *locking* pasivo es capaz de compensar pequeñas perturbaciones de la longitud de onda de resonancia, que pueden ser resultado de vibraciones indeseadas en el montaje experimental.

Para poder implementar las técnicas de *locking* activo, se ha desarrollado un sistema electrónico de realimentación que puede actuar sobre diferentes elementos del montaje para estabilizar la transmitancia del sistema. En la primera de ellas, el sistema de realimentación modula la longitud de onda de emisión del láser para corregir los efectos térmicos no-lineales y las perturbaciones externas. Una vez se estudió y caracterizó completamente esta técnica más convencional, utilizamos las conclusiones obtenidas para implementar dos técnicas de *locking* activo que permiten la estabilización mediante la sintonización de la longitud de onda de resonancia de los *WGMs*. La diferencia entre estas técnicas y la convencional es que, en nuestro caso, la señal de realimentación no se aplica al láser, sino al propio micro-resonador. Esto permite trabajar a longitud de onda constante, lo cual es una gran ventaja para distintos experimentos, especialmente aquellos centrados en efectos ópticos no-lineales que presentan condiciones de ajuste de fase estrictas. La sintonización de las resonancias se consigue bien mediante el estiramiento axial del micro-resonador cilíndrico (efecto elasto-óptico), o a través de una variación de la temperatura del micro-resonador (efecto termo-óptico). Ambas técnicas activas muestran varias ventajas respecto al *locking* pasivo: principalmente, permiten la selección de la resonancia específica que se sintoniza con el láser, y el control sobre la distancia espectral relativa entre el láser y la resonancia, lo que permite seleccionar la energía acoplada a la cavidad. Para caracterizar el desempeño de ambas técnicas, se ha medido su respuesta ante dos tipos de perturbaciones externas controladas: un cambio en escalón del punto de trabajo, y la respuesta ante una modulación armónica de la longitud de onda de emisión del láser.

Aprovechando las técnicas de *locking* desarrolladas, se han excitado efectos ópticos no-lineales en micro-resonadores con geometría esférica: esferas y burbujas de sílice. Además, se ha estudiado su estabilidad temporal, mostrando que cuando la técnica *locking* empleada es activa, la estabilidad del efecto se ve incrementada respecto de cuando se utiliza una técnica pasiva.

Por último, se ha aprovechado la técnica de *locking* pasivo que se describió en primer lugar para realizar experimentos de opto-mecánica. Debido a la gran densidad energética que existe dentro del resonador cuando se ha realizado el *locking*, la presión de radiación es significativa. Como consecuencia, existe un acoplamiento opto-mecánico que es capaz de excitar vibraciones del propio micro-resonador, que soporta tanto modos resonantes ópticos (*WGMs*), como mecánicos. Las vibraciones inducen deformaciones mecánicas que modulan la longitud de onda de las resonancias ópticas a la frecuencia propia del modo mecánico. Para medir las frecuencias propias de los modos mecánicos, así como la amplitud de vibración, se monitoriza la transmitancia del sistema con un analizador de espectros eléctrico y un osciloscopio. Estos experimentos se han realizado con micro-burbujas de sílice, cuyos modos mecánicos presentan factores de calidad relativamente altos, 10^3. Las estructuras caracterizadas han mostrado dos rangos de frecuencias de vibración: un rango de altas frecuencias, MHz, que se corresponde con la vibración de las paredes de la propia micro-burbuja; y un rango de bajas frecuencias, kHz, consecuencia de la vibración de toda la estructura, formada por micro-burbuja y el capilar que la sostiene.

Cuando las potencias ópticas acopladas al micro-resonador se incrementan por encima de cierto umbral, los modos vibracionales excitados por los *WGMs* empiezan a comportarse de forma caótica. Esta ruta hacia el caos muestra el mismo comportamiento ya publicado en anteriores trabajos realizados en micro-resonadores con otras geometrías: un cuasi-doblamiento de las frecuencias de vibración que, para potencias altas, lleva a un régimen caótico en el que las vibraciones presentan un continuo de frecuencias. Este tipo de comportamiento es la primera vez que se observa en micro-burbujas de sílice.

Conclusiones

En este trabajo de tesis se comenzó describiendo la propagación y confinamiento de los *WGMs* en micro-resonadores cilíndricos fabricados con materiales con distintas anisotropias: anisotropía uniaxial y girotrópica. A partir de estos desarrollos teóricos, se han proporcionado las herramientas para estudiar cómo afecta a la posición espectral de las resonancias WGM un campo magnético, una deformación axial, o un incremento de temperatura en el micro-resonador: estos fenómenos se conocen como efectos magneto-, elasto- y termo-óptico, respectivamente.

La técnica experimental de medida, basada en la sintonizabilidad de las resonancias *WGMs* con los parámetros del micro-resonador, nos ha permitido caracterizar distintos dispositivos fabricados en fibra óptica con un bajo límite de detección, con resolución axial, y en un rango amplio de longitudes de onda. En particular, se ha medido la anisotropía inducida por tensión en micro-resonadores cilíndricos de sílice, al igual que los coeficientes elasto-ópticos de fibras de sílice y PMMA, y se han comparado los resultados experimentales con las simulaciones teóricas. También se han caracterizado las pérdidas por absorción y *scattering* en fibras fotosensibles irradiadas con luz UV. Este proceso de irradiación es ampliamente utilizado en el campo de las fibras ópticas para la fabricación de dispositivos tan extendidos en los sistemas de comunicaciones como son las redes de Bragg, por lo que conocer en detalle sus efectos resulta de gran utilidad. Por otro lado, la resolución axial de la técnica ha posibilitado la medida de los perfiles de temperatura, además del calentamiento, generados por señales ópticas de potencia moderada en LPGs y fibras activas dopadas con Ho y Yb. La información obtenida de estos experimentos permite el diseño de nuevos dispositivos y fibras dopadas con características optimizadas.

Se han implementado técnicas activas y pasivas de *locking* que permiten estabilizar la respuesta espectral de las resonancias. Dos de estas propuestas, hasta donde sabemos, no han sido presentadas anteriormente, y están basadas en la sintonización de los parámetros del micro-resonador. Estas dos técnicas activas, están basadas en los efectos elasto- y termo-óptico, y abren la posibilidad de trabajar a longitud de onda del láser constante, algo que no permiten las técnicas más convencionales. Gracias a esta característica es posible excitar efectos ópticos no-lineales con una mayor estabilidad temporal

Por último, empleando una técnica pasiva de *locking* basada en efectos térmicos no-lineales, se han generado y caracterizado efectos opto-mecánicos en micro-burbujas de sílice. En estos experimentos los WGMs de alta potencia excitan los modos mecánicos de estas estructuras, gracias a la presión de radiación. Además, hemos estudiado la dinámica de estos modos de vibración, observándose una transición al caos a medida que la potencia óptica aumenta.

Para terminar este resumen, quiero señalar que en los resultados presentados he pretendido resaltar todas las aportaciones de los distintos desarrollos teóricos y experimentos realizados a lo largo de la tesis, señalando las más novedosas.

1 | Introduction

Optical microcavities play a fundamental role in modern photonic technologies. The operational principle of the microcavities is based on the phenomenon of resonance, which enables the confinement of the light within its structure. The light traveling in the optical cavity interferes with itself enhancing specific optical frequencies. This feature is exploited in both fundamental and applied research applications, such as: novel laser sources fabrication, dynamic filters design, optical sensors, integrated optics, study of nonlinear phenomena or quantum optical applications.

The different optical microcavities can be identified according to the confinement mechanism, Fabry-Perot or photonic crystals for example. One specific family are those based on Whispering Gallery Modes (WGMs), that are modes confined in circular shaped microcavities. These microcavities, generally made of a dielectric material, possess a structure with rotational symmetry: toroidal, spherical or cylindrically shaped. The light circulating azimuthally in the inner surface of the optical cavity by total internal reflection is named WGMs, analogously to the acoustic scenario. These surface modes are resonant in optical wavelength, and the spectral location of the resonances depends on the geometry, size, shape and composition of the optical cavity. In addition, the microcavities exhibit low losses, high Q-factors, and small cavity mode volumes. These aspects allow the use of WGMs-based microresonators for different applications, since they enable specific features that are not easily available with other techniques. For example, the properties of the resonator material can be characterized with ultra-low detection limits by exploiting the tunability of WGMs caused by the microresonator parameters variation. Development of laser sources with low-thresholds is feasible due to the large confinement of the electromagnetic field and the high Q-factor of these resonators. Additionally, the small mode-volumes of the microcavities, together with their low losses, allow the observation of nonlinear phenomena, such as optomechanic effects, even when low power signals are used.

1.1 Historical background

At the end of the XIX century, in 1878, John William Strutt (Lord Rayleigh) explained the phenomenon of traveling whispers in the doom of the St Paul's Cathedral in London [1]. He attributed this phenomenon to the acoustic waves propagating around the curved surface of the gallery, and proposed a method to solve the problem based upon the calculations employed in geometrical optics; it was years later when he solved the problem from a wave-propagation point of view [2, 3]. It was Rayleigh himself who proposed the application of his theory to electromagnetic waves.

Later in 1908, Mie developed his theory for electromagnetic plane waves dispersed by spheres with diameters of the order of the optical wavelength [4]. One year later, Debye, from Mie's dispersion theory, established the equations for the resonant eigenfrequencies of dielectric and metallic spheres, which naturally include those of WGMs [5]. Shortly after this, in 1909 and 1910, the same Debye, together with Hondros, developed the theory of electromagnetic waves transmission along dielectric wires [6, 7], which was experimentally confirmed by Zhan [8]. It was not until 1939 when Richtmyer, who studied the electromagnetic wave propagation in dielectric rods, proposed the employment of dielectric structures to confine electromagnetic waves by total internal reflection. He showed that

Whispering Gallery Mode Resonators (WGMRs) could exhibit high Q-factors values [9]. A more detailed study of WGMRs was performed shortly after by Stratton [10]. In the following years, more advances were accomplished in the theory of acoustic-WGMs, and several applications were proposed in the microwave domain of WGM resonances.

The first observation of WGM resonances in the optical domain was in 1961. Garret *et al.* observed that crystalline CaF_2 spherical resonators could be used as laser resonators. They observed pulsed laser oscillations in spheres with diameters in the millimeters range [11]. Optical WGM resonances were observed in other applications such as optical-levitation [12], fluorescence experiments [13], measurement of spherical resonator parameters [14], or observation of Raman scattering [15].

Until 1989, WGM resonances with high Q-factors were indirectly observed in many experiments of light scattering, even though no practical optical devices were reported based on them. The experiments with WGMs in liquid resonators presented many manipulation difficulties and instabilities. On the other hand, the solid resonators reported up to that moment, exhibited a variety of inconveniences such as high refractive index, low Q-factors or inefficient coupling techniques. It was in that year when Braginsky *et al.* achieved the direct excitation of ultra-high Q-factor optical-WGM resonances in fused-silica microspheres [16]. The light of a He-Ne laser was coupled into the silica microsphere by means of a prism, enabling the excitation of the resonant modes and reaching a coupling efficiency $\sim 80\%$. After this demonstration, different techniques were designed to increase the efficiency of excitation. Knight *et al.* proposed the use of tapered optical fibers to increase the efficiency even higher, up to 90% [17]. Some years later, Spillane *et al.* showed that with the taper-resonator coupling technique, efficiencies as high as 99.97% can be achieved [18].

All these advances in the excitation of WGM resonances in microcavities, especially in fused-silica resonators, enable the feasibility of designing practical devices with different applications based on these kind of microresonators. In the last years, WGMRs have attracted an increasing attention, especially in the areas of optical communications, for the generation of combs of optical frequencies [19], for lasing [20], for the observation of nonlinear phenomena [21], or their application in sensing and biosensing [22].

1.2 Microresonators for WGMs

The different types of microresonators can be classified according to the confinement method [23]: Fabry-Perot, WGMs, and photonic crystals. Conventional Fabry-Perot microresonators are employed in most of the branches of modern photonics, but, despite their versatility, they are usually complex and expensive devices, with large sizes that present problems of miniaturization. Photonic crystal cavities, although they can provide extremely small mode volumes, generally present low Q-values. Meanwhile, fabrication of WGMRs can be very simple and inexpensive. Their small sizes also lead to an excellent mechanical stability and accurate control, which is of great interest for certain applications [24]. Moreover, they can also be integrated easily in complex photonic devices.

Several geometries have been investigated for the fabrications of WGMRs: cylindrical [25], spherical [26], or toroidal [27]. Due to their feasibility to be integrated in photonic circuits, geometries such as disk microresonators have been also studied [28]. Besides the geometry, different materials have been investigated for their fabrication. In order to have high Q-factors, a low optical attenuation is required. In the past, WGMs were studied in liquid droplets [29], but they showed major limitations for its implementation in practical photonic devices. In the case of solid WGMRs, apart from fused silica, other amorphous materials have been studied, for example polymers [30]. In the last years, the use of crystalline microresonators has increased due to their wider transparency window, higher nonlinearities, and lower attenuation losses, leading to microresonators with ultra-high Q-factors [31]. Despite of these advantages, the fabrication processes are more complex than for those based on fused silica, and it is not so easy to obtain different geometries for the WGMRs.

Several applications have been developed by employing different types of geometries and materials. One of the most developed devices are the photonic tunable filters, whose performance is usually achieved by means of applying strain or variations of temperature to the microresonators [32]. WGMRs are also used as the platform for evanescent wave biosensors due to their low detection limit and applicability to different biological analytes [22]. Besides, WGM resonances have been employed to measure properties of the microresonators geometry or material, such as radius fluctuations or thermal variations in optical fibers and optical fiber devices [25, 33]. In addition to the use of WGMRs as passive devices for sensing or metrology, different applications for lasing have been developed based on WGM resonances. The high Q-factors and small mode volumes make these devices suitable for the design of, for example, low threshold lasers [20]. In the last years, a great variety of nonlinear phenomena on WGMRs have been studied. The unique characteristics of theses devices allow to excite and observe optical nonlinear effects [21], and optomechanical effects [34].

1.3 Aims of this thesis

The aims of this thesis can be distinguished in two parts. In the first part, we develop new techniques for the characterization of optical fibers and fiber componentes based on the study of the WGMs. In the second part, we investigate the feasibility of WGMRs to excite and observe different nonlinear effects, optical and optomechanical.

First, we study the propagation and confinement, the spectral properties, and the coupling techniques of WGMs in anisotropic cylindrical microresonators. These studies are basic to develop a theoretical description of the following experiments that we will carry out to characterize the different optical fiber devices. The theoretical description will be presented in Chapter 2, while in Chapter 3 we will show the general experimental procedures.

One objective of this work is to characterize silica, and polymer optical fibers under axial strain, to obtain the strain-optic coefficients of these materials. The idea is to exploit the tunability of WGM resonances as a function of the applied strain, and relate the change in the spectral position of the resonances with the microresonator properties variation induced by the strain. In the past, this measurement has been carried out by employing a combination of polarimetric and interferometric measurements, but our technique will provide new advantages when compared to the conventional one. The theoretical description and the experiments related to the strain-optic effect in WGMRs are detailed in Chapter 4.

We are also interested in exploiting the thermal sensitivity of the WGMs to characterize photosensitive and active doped fibers when they are in operation, this is, when an optical signal propagates through them. We will use WGMs to determine the effect of UV-processing of photosensitive fibers: the conventional methods to fabricate fiber Bragg grating and long period gratings involve the irradiation of those fibers with UV light, which increases their losses. WGMs allow an accurate, point to point, measure of such effects. Also, when signals of moderate power propagate in optical fibers, they may suffer from some heating that can be characterized using the WGM-based technique. This is of special interest when considering fiber devices that can be part of laser cavities, which confine considerable amounts of optical power. The low detection and the strong spatial localization of the WGMs, allow the thermal characterization of these devices point to point, with high sensitivity and using short length devices, while the conventional techniques provide averaged values, and usually require of long fibers. The study of the thermo-optic effect in fibers and fiber devices using WGMs will be presented in Chapter 5.

The last chapter of this thesis, Chapter 6, is denoted to the study of locking techniques to stabilize the relative spectral position between the laser and the WGM resonances. In the recent years, the implementation of different locking techniques has been reported with the objective of overcoming the difficulties of matching the laser wavelength to the WGM resonance. We will present novel techniques based on the effects previously studied, the strain-optic and thermo-optic effects. We will develop an all-optical active locking system that will allow us exciting, controlling, and observing optical and optomechanical nonlinear effects in silica microresonators of different geometries, such as spheres and bubbles.

References

[1] L. Rayleigh. "*The theory of sound*", 1st edition, Macmillan, London (1878).

[2] L. Rayleigh. "*CXII. The problem of the whispering gallery*", Philosophical Magazine, **20**, pp. 1001–1004 (1910).

[3] L. Rayleigh. "*IX. Further applications of Bessel's functions of high order to the Whispering Gallery and allied problems*", Philosophical Magazine, **27**, pp. 100–109 (1914).

[4] G. Mie. "*Beiträge zur Optik trüber Medien, speziell kolloidaler Metallösungen*", Annalen der Physik, **330**, pp. 377–445 (1908).

[5] P. Debye. "*Der Lichtdruck auf Kugeln von beliebigem Material*", Annalen der Physik, **335**, pp. 57–136 (1909).

[6] D. Hondros. "*Über elektromagnetische Drahtwellen*", Annalen der Physik, **335**, pp. 905–950 (1909).

[7] D. Hondros and P. Debye. "*Elektromagnetische Wellen an dielektrischen Drähten*", Annalen der Physik, **337**, pp. 465–476 (1910).

[8] H. Zahn. "*Über den Nachweis elektromagnetischer Wellen an dielektrischen Drähten*", Annalen der Physik, **354**, pp. 907–933 (1916).

[9] R. D. Richtmyer. "*Dielectric Resonators*", Journal of Applied Physics, **10**, pp. 391–398 (1939).

[10] J. A. Stratton. "*Electromagnetic theory*", 1st edition, McGraw-Hill New York (1941).

[11] C. G. B. Garrett, W. Kaiser, and W. L. Bond. "*Stimulated Emission into Optical Whispering Modes of Spheres*", Physical Review, **124**, pp. 1807–1809 (1961).

[12] A. Ashkin and J. M. Dziedzic. "*Observation of Resonances in the Radiation Pressure on Dielectric Spheres*", Physical Review Letters, **38**, pp. 1351–1354 (1977).

[13] R. E. Benner, P. W. Barber, J. F. Owen, and R. K. Chang. "*Observation of Structure Resonances in the Fluorescence Spectra from Microspheres*", Physical Review Letters, **44**, pp. 475–478 (1980).

[14] P. Chylek, V. Ramaswamy, A. Ashkin, and J. M. Dziedzic. "*Simultaneous determination of refractive index and size of spherical dielectric particles from light scattering data*", Applied Optics, **22**, pp. 2302–2307 (1983).

[15] J. B. Snow, S.-X. Qian, and R. K. Chang. "*Stimulated Raman scattering from individual water and ethanol droplets at morphology-dependent resonances*", Optics Letters, **10**, pp. 37–39 (1985).

[16] V. Braginsky, M. Gorodetsky, and V. Ilchenko. "*Quality-factor and nonlinear properties of optical whispering-gallery modes*", Physics Letters A, **137**, pp. 393–397 (1989).

[17] J. C. Knight, G. Cheung, F. Jacques, and T. A. Birks. "*Phase-matched excitation of whispering-gallery-mode resonances by a fiber taper*", Optics Letters, **22**, pp. 1129–1131 (1997).

[18] S. Spillane, T. Kippenberg, O. Painter, and K. Vahala. "*Ideality in a Fiber-Taper-Coupled Microresonator System for Application to Cavity Quantum Electrodynamics*", Physical Review Letters, **91**, p. 043902 (2003).

[19] P. Del'Haye, T. Herr, E. Gavartin, M. L. Gorodetsky, R. Holzwarth, and T. J. Kippenberg. "*Octave Spanning Tunable Frequency Comb from a Microresonator*", Physical Review Letters, **107**, p. 063901 (2011).

[20] N. B. Tomazio, L. D. Boni, and C. R. Mendonca. "*Low threshold Rhodamine-doped whispering gallery mode microlasers fabricated by direct laser writing*", Scientific Reports, **7**, p. 8559 (2017).

[21] D. Farnesi, A. Barucci, G. C. Righini, S. Berneschi, S. Soria, and G. Nunzi Conti. "*Optical Frequency Conversion in Silica-Whispering-Gallery-Mode Microspherical Resonators*", Physical Review Letters, **112**, p. 093901 (2014).

[22] F. Vollmer and S. Arnold. "*Whispering-gallery-mode biosensing: label-free detection down to single molecules*", Nature Methods, **5**, (2008).

[23] K. J. Vahala. "*Optical microcavities*", Nature, **424**, pp. 839–846 (2003).

[24] A. B. Matsko and V. S. Ilchenko. "*Optical resonators with whispering-gallery modes-part I: basics*", IEEE Journal of Selected Topics in Quantum Electronics, **12**, pp. 3–14 (2006).

[25] T. A. Birks, J. C. Knight, and T. E. Dimmick. "*High-resolution measurement of the fiber diameter variations using whispering gallery modes and no optical alignment*", IEEE Photonics Technology Letters, **12**, pp. 182–183 (2000).

[26] A. Chiasera, Y. Dumeige, P. Féron, M. Ferrari, Y. Jestin, G. Nunzi Conti, S. Pelli, S. Soria, and G. Righini. "*Spherical whispering-gallery-mode microresonators*", Laser & Photonics Reviews, **4**, pp. 457–482 (2010).

[27] T. J. Kippenberg, S. M. Spillane, and K. J. Vahala. "*Kerr-Nonlinearity Optical Parametric Oscillation in an Ultrahigh-Q Toroid Microcavity*", Physical Review Letters, **93**, p. 083904 (2004).

[28] M. Borselli, K. Srinivasan, P. E. Barclay, and O. Painter. "*Rayleigh scattering, mode coupling, and optical loss in silicon microdisks*", Applied Physics Letters, **85**, pp. 3693–3695 (2004).

[29] H.-B. Lin, J. D. Eversole, and A. J. Campillo. "*Continuous-wave stimulated Raman scattering in microdroplets*", Optics Letters, **17**, pp. 828–830 (1992).

[30] M. Kuwata-Gonokami and K. Takeda. "*Polymer whispering gallery mode lasers*", Optical Materials, **9**, pp. 12–17 (1998).

[31] A. A. Savchenkov, V. S. Ilchenko, A. B. Matsko, and L. Maleki. "*Kilohertz optical resonances in dielectric crystal cavities*", Physical Review A, **70**, p. 051804 (2004).

[32] A. L. Huston and J. D. Eversole. "*Strain-sensitive elastic scattering from cylinders*", Optics Letters, **18**, pp. 1104–1106 (1993).

[33] M. Delgado-Pinar, I. L. Villegas, A. Díez, J. L. Cruz, and M. V. Andrés. "*Measurement of temperature profile induced by the optical signal in fiber Bragg gratings using whispering-gallery modes*", Optics Letters, **39**, pp. 6277–6280 (2014).

[34] T. Kippenberg and K. Vahala. "*Cavity Opto-Mechanics*", Optics Express, **15**, pp. 17172–17205 (2007).

2 | WGMs theory

In this chapter, we will describe the main theoretical aspects of the WGMs for the purpose of this work. The propagation of WGMs in anisotropic cylindrical microresonators, their confinement, and the resonant conditions will be studied. We will calculate the dispersion curves, together with the electromagnetic field distribution of the modes. An analysis of the theoretical results will be presented in order to characterize the spectral and field properties of the modes. To properly describe the performance of the resonators treated in this work, we will characterize the quality factor and the different loss sources. In addition, we will study the coupling mechanism between a microfiber and a microresonator in terms of energy. Last, we will show that the WGMs are a particular solution of the guided modes that a cylindrical dielectric waveguide can support.

2.1 WGMs in uniaxial cylindrical microresonators

WGM microresonators (MRs) are generally made of dielectric materials. Although the most employed material is fused silica, an isotropic medium, in some cases, the fabrication material can be anisotropic [1]. In addition, it is possible to introduce an anisotropy in an isotropic material by means of different effects, as it will be shown afterwards in this work. In consequence, in this section, the description of the WGMs propagation in anisotropic dielectric MRs is provided.

The structure of the MR can be distinguished in two regions. Region I consists on a dielectric rod of infinite length and radius a with anisotropic permittivity, $\varepsilon_0\bar{\varepsilon}_1$, while region II is a dielectric infinite medium (typically air) with isotropic permittivity, $\varepsilon_0\varepsilon_2$, which is surrounding the MR. Both media are homogeneous, source-free, lossless, and with a magnetic permeability of μ_0. In Fig. 2.1, it is shown a scheme of the two regions. Due to the geometry of the problem, it is appropriate to employ a cylindrical coordinate system. The solution to the problem of the WGMs propagating in cylindrical MRs can be found by solving the Maxwell's equations in each one of the two different regions and applying the proper boundary conditions.

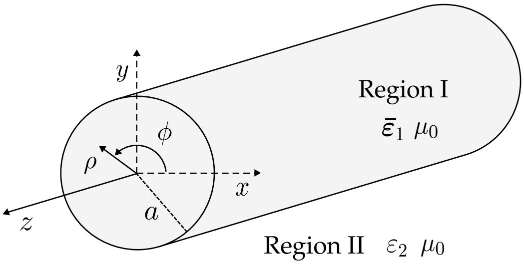

Figure 2.1: Scheme of a solid cylindrical microresonator.

The described structure supports several guided modes. We study here those that propagate circularly around the cylinder, the so-called WGMs. The direction of propagation is purely azimuthal. Therefore, the dependence of both the electric ($\mathbf{E}$) and magnetic ($\mathbf{H}$) fields as a function of the coordinate ϕ can be described in terms of $e^{-\jmath\beta_\phi\phi}$, where β_ϕ is the propagation constant of the modes. Besides, a harmonic time-dependence of the fields is considered, $e^{\jmath\omega t}$, where ω is the angular frequency.

Following the typical technique employed to solve waveguides invariant under axial translation [2], the electromagnetic field can be written as:

$$\begin{aligned}\mathbf{E}(\mathbf{r},t) &= \mathbf{e}(\rho)e^{-\jmath\beta_\phi\phi}e^{\jmath\omega t}\\ \mathbf{H}(\mathbf{r},t) &= \mathbf{h}(\rho)e^{-\jmath\beta_\phi\phi}e^{\jmath\omega t}\end{aligned} \tag{2.1}$$

where

$$\begin{aligned} \mathbf{e}(\rho) &= e_\rho(\rho)\hat{\boldsymbol{u}}_\rho + e_\phi(\rho)\hat{\boldsymbol{u}}_\phi + e_z(\rho)\hat{\boldsymbol{u}}_z \\ \mathbf{h}(\rho) &= h_\rho(\rho)\hat{\boldsymbol{u}}_\rho + h_\phi(\rho)\hat{\boldsymbol{u}}_\phi + h_z(\rho)\hat{\boldsymbol{u}}_z \end{aligned} \tag{2.2}$$

being $\hat{\boldsymbol{u}}_\rho$, $\hat{\boldsymbol{u}}_\phi$ and $\hat{\boldsymbol{u}}_z$ the unit vectors in the cylindrical coordinate system. As it can be seen in Eqs. (2.2), the amplitude of the electromagnetic field only depends on the coordinate ρ. Since the length of the cylinder is considered infinite, and there is a translational symmetry, the electromagnetic field will not show dependence with the z coordinate. It is worth to note that, even though there is not a mechanism that confines the WGMs in the axial direction, in practical conditions they are localized in z [3], as we will discuss in the following chapter.

To obtain the WGMs guided in the MR, the Maxwell's equations must be solved for the fields described in Eqs. (2.1).

$$\begin{aligned} \nabla \cdot (\bar{\varepsilon}\mathbf{E}) &= 0 \\ \nabla \cdot \mathbf{H} &= 0 \\ \nabla \times \mathbf{E} &= -\jmath\omega\mu_0\mathbf{H} \\ \nabla \times \mathbf{H} &= \jmath\omega\varepsilon_0\bar{\varepsilon}\mathbf{E} \end{aligned} \tag{2.3}$$

where the relative dielectric constant $\bar{\varepsilon}$ is a tensor. Depending on the material or the effect that induces the anisotropy, the expression of the tensor varies. We will consider here a uniaxial medium [4], since the WGMs response of the experiments that we will describe in Chapters 4 and 5 can be theoretically derived from this anisotropy. Two diagonal elements of the tensor are equal and the other one is different, and can be written as follows:

$$\bar{\varepsilon} = \begin{pmatrix} \varepsilon_t & & \\ & \varepsilon_t & \\ & & \varepsilon_z \end{pmatrix}; \qquad \begin{cases} \varepsilon_t : & \text{transversal to the } z \text{ coordinate} \\ \varepsilon_z : & \text{parallel to the } z \text{ coordinate} \end{cases} \tag{2.4}$$

By expanding the Maxwell's equations with the expression of the fields, and the permittivity tensor, the wave equations for the electric and magnetic fields are obtained:

$$\begin{aligned}\nabla \times (\nabla \times \mathbf{E}) &= \omega^2 \mu_0 \varepsilon_0 \bar{\boldsymbol{\varepsilon}} \mathbf{E} \\ \nabla \times \left(\bar{\boldsymbol{\varepsilon}}^{-1} \nabla \times \mathbf{H}\right) &= \omega^2 \mu_0 \varepsilon_0 \mathbf{H}\end{aligned} \tag{2.5}$$

To solve the two vectorial wave equations, we carried out the same analysis employed to obtain the conventional modes in optical fibers. The axial components of the differential wave equations, Eqs. (2.5), are calculated. After solving both expressions, the E_z and H_z components of the fields are obtained, which allows to calculate all the transversal components of the electromagnetic field by exploiting the Maxwell's equations.

Therefore, the axial components of the wave equations can be written as:

$$\begin{aligned}\left[\rho^2 \partial_\rho^2 + \rho \partial_\rho + \left(\rho^2 k_0^2 \varepsilon_z - \beta_\phi\right)\right] e_z(\rho) = 0 \\ \left[\rho^2 \partial_\rho^2 + \rho \partial_\rho + \left(\rho^2 k_0^2 \varepsilon_t - \beta_\phi\right)\right] h_z(\rho) = 0\end{aligned} \tag{2.6}$$

where $k_0 = \omega\sqrt{\mu_0 \varepsilon_0} = 2\pi/\lambda_0$ is the wave number in vacuum. Both differential equations have the same form, which can be identified as Bessel equations [5]. Before applying boundary conditions at the interface between the two media, we study the conditions that the propagation constant, β_ϕ, must fulfill to have WGM resonances.

WGMs propagate in the azimuthal direction, which leads to the fact that the confined wave will interfere with itself after a round trip. A constructive interference is needed to observe a WGM resonance. In the opposite scenario, the loaded energy in the resonator is of the same order as the energy lost by radiation and the resonances do not show up. To observe constructive interference, the phase of the confined wave must be the same with a difference of a multiple of 2π after every round trip. This constraints the values of the azimuthal propagation constant, β_ϕ, to integers.

$$\beta_\phi = m \in \mathbb{Z} \tag{2.7}$$

The physical mechanism that confine the WGMs inside the resonator can be described qualitatively by means of the total internal reflection. The electromagnetic wave propagates around the inner surface of the microcavity suffering multiple reflections, Fig. 2.2.

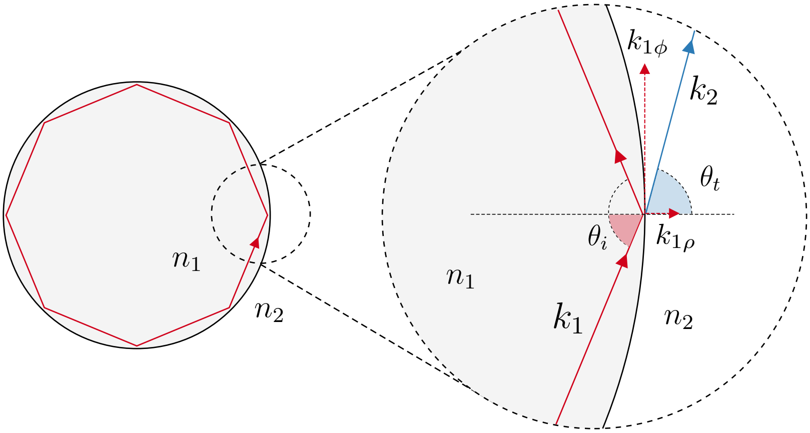

Figure 2.2: Geometrical ray representation of the total internal reflection at the interface between the resonator and the external medium.

The propagation constant is related with the azimuthal component of the WGM wave vector by $\beta_\phi = k_{1\phi}a$. Thus, its value must be smaller than the wave vector in the region I, k_1, which can be written as:

$$k_1^2 = k_{1\rho}^2 + k_{1\phi}^2; \quad \rightarrow \quad k_{1\phi} < k_1 \tag{2.8}$$

Besides, taking into account the Snell's law, in order to have total internal reflection, the incidence angle must be larger than the critical angle ($\theta_i > \theta_c$) [6]. This condition implies that the value of $k_{1\phi}$ must be larger than the wave vector in the outer medium:

$$\sin\theta_i > \frac{n_2}{n_1}; \quad \rightarrow \quad k_{1\phi} > k_2 \tag{2.9}$$

Therefore, the allowed values of the propagation constant to have WGM resonances are constricted as follows:

$$k_2 a < m < k_1 a \tag{2.10}$$

Once we have established the restrictions for the propagation constant, β_ϕ, of the WGM resonances, the differential wave equations, Eqs. (2.6), can be solved in each region. In region I (the MR), $\rho < a$, it is necessary to consider the tensorial behavior of the permittivity due to the anisotropy. Each one of the wave equations depends on a different component of the relative dielectric constant tensor, see Eqs. (2.6). In region II (the outer medium), $\rho > a$, both equations depend on the same value of the permittivity, given by ε_2, since the medium is isotropic.

Finally, it is necessary to establish some constraints to the mathematical solutions of the amplitude of the fields to obtain an electromagnetic wave with physical meaning. The general solution to the Bessel equation can be written as: $\psi(z) = CJ_m(z) + DY_m(z)$, where J_m is the Bessel function of first kind, and Y_m is the Bessel function of second kind [5]. The constraints that we impose to this general solution are two: (i) Because both media are source-free, the field must have a finite value in all the space. That implies that in region I, the solution of the amplitude is given only by the Bessel function J_m, since Y_m is singular at the origin ($\rho = 0$). (ii) In region II, the two Bessel functions are well-behaved. If both are studied when ρ tends to infinite, the electromagnetic field can be described in this region as the sum of two types of modes: one mode of radial radiation inward-going and one outward-going.

$$\psi(z \to \infty) \propto \underbrace{\underbrace{e^{\jmath z}}_{\text{inward}} \left(C + \frac{1}{\jmath} D\right)}_{=0} + \underbrace{e^{-\jmath z}}_{\text{outward}} \left(C - \frac{1}{\jmath} D\right) \tag{2.11}$$

Here, we will only consider an outward-going radiation field. This can be described by the asymptotic form of the Hankel function of second kind, $H_m^{(2)}$, which is a linear superposition of the functions J_m and Y_m [7]. Applying this two restrictions to the general solution, the expression of the electromagnetic field for the WGMs is derived.

In an axial waveguide, the guided modes can be grouped attending to their polarization. In general, the modes supported by a dielectric waveguide can be classified in TE, TM and hybrid modes (TEM modes are not allowed) [2]. For WGMs, although the propagation is in the azimuthal direction, the classical notation in which the fields are transversal to the axial direction is preserved. Besides, in the case of isotropic dielectric cylinders, hybrid modes with pure azimuthal propagation can not exist [8]. Therefore, the WGMs are classified into two families, TE and TM. This behavior is also satisfied for the case of uniaxial anisotropic media, which is described in this section. Thus, from this moment and throughout this work, we will consider separately the two states of polarization of the WGMs. The electromagnetic fields will be written as follows:

TM modes

- *Region I* ($\rho < a$):

$$\begin{aligned} E_z^I &= A_1 J_m(k_0 n_z \rho) e^{-\jmath m \phi} e^{\jmath \omega t} \\ H_\rho^I &= \frac{m}{\omega \mu_0} \frac{1}{\rho} A_1 J_m(k_0 n_z \rho) e^{-\jmath m \phi} e^{\jmath \omega t} \\ H_\phi^I &= \frac{k_0 n_z}{\jmath \omega \mu_0} A_1 J_m'(k_0 n_z \rho) e^{-\jmath m \phi} e^{\jmath \omega t} \\ E_\rho^I &= E_\phi^I = H_z^I = 0 \end{aligned} \tag{2.12}$$

- *Region II* ($\rho > a$):

$$
\begin{aligned}
E_z^{II} &= A_2 H_m^{(2)}(k_0 n_2 \rho) e^{-\jmath m\phi} e^{\jmath\omega t} \\
H_\rho^{II} &= \frac{m}{\omega\mu_0}\frac{1}{\rho} A_2 H_m^{(2)}(k_0 n_2 \rho) e^{-\jmath m\phi} e^{\jmath\omega t} \\
H_\phi^{II} &= \frac{k_0 n_2}{\jmath\omega\mu_0} A_2 H_m^{(2)'}(k_0 n_2 \rho) e^{-\jmath m\phi} e^{\jmath\omega t} \\
E_\rho^{II} &= E_\phi^{II} = H_z^{II} = 0
\end{aligned}
\tag{2.13}
$$

TE modes

- *Region I* ($\rho < a$):

$$
\begin{aligned}
H_z^{I} &= B_1 J_m(k_0 n_t \rho) e^{-\jmath m\phi} e^{\jmath\omega t} \\
E_\rho^{I} &= -\frac{m}{\omega\varepsilon_0\varepsilon_t}\frac{1}{\rho} B_1 J_m(k_0 n_t \rho) e^{-\jmath m\phi} e^{\jmath\omega t} \\
E_\phi^{I} &= -\frac{k_0 n_t}{\jmath\omega\varepsilon_0\varepsilon_t} B_1 J_m'(k_0 n_t \rho) e^{-\jmath m\phi} e^{\jmath\omega t} \\
H_\rho^{I} &= H_\phi^{I} = E_z^{I} = 0
\end{aligned}
\tag{2.14}
$$

- *Region II* ($\rho > a$):

$$
\begin{aligned}
H_z^{II} &= B_2 H_m^{(2)}(k_0 n_2 \rho) e^{-\jmath m\phi} e^{\jmath\omega t} \\
E_\rho^{II} &= -\frac{m}{\omega\varepsilon_0\varepsilon_2}\frac{1}{\rho} B_2 H_m^{(2)}(k_0 n_2 \rho) e^{-\jmath m\phi} e^{\jmath\omega t} \\
E_\phi^{II} &= -\frac{k_0 n_2}{\jmath\omega\varepsilon_0\varepsilon_2} B_2 H_m^{(2)'}(k_0 n_2 \rho) e^{-\jmath m\phi} e^{\jmath\omega t} \\
H_\rho^{II} &= H_\phi^{II} = E_z^{II} = 0
\end{aligned}
\tag{2.15}
$$

where $n_i = \sqrt{\varepsilon_i}$ is each refractive index component; J_m' and $H_m^{(2)'}$ are the derivative of the Bessel function of first kind and the Hankel function of second kind, respectively; A_i and B_i are constants that do not depend on any spatial coordinate or time. The above equations, Eqs. (2.12)-(2.15), describe the electromagnetic field of the WGMs completely. Once the fields are obtained, boundary conditions that force the continuity of the tangential components of the electromagnetic field at the interface ($\rho = a$) are applied:

$$\begin{aligned} &\textbf{TM:} \quad E_z^I(\rho = a) = E_z^{II}(\rho = a); \qquad H_\phi^I(\rho = a) = H_\phi^{II}(\rho = a); \\ &\textbf{TE:} \quad H_z^I(\rho = a) = H_z^{II}(\rho = a); \qquad E_\phi^I(\rho = a) = E_\phi^{II}(\rho = a); \end{aligned} \tag{2.16}$$

These conditions lead to two equations with two unknown variables, the constants A_i and B_i, for each polarization state. Nontrivial solutions for the 2x2 equation system exist only if the determinant vanishes. Thus, the characteristic equations for the TM and TE modes are:

$$\begin{aligned} &\textbf{TM:} \quad n_z \frac{J'_m(k_0 n_z a)}{J_m(k_0 n_z a)} = n_2 \frac{H_m^{(2)'}(k_0 n_2 a)}{H_m^{(2)}(k_0 n_2 a)} \\ &\textbf{TE:} \quad \frac{1}{n_t} \frac{J'_m(k_0 n_t a)}{J_m(k_0 n_t a)} = \frac{1}{n_2} \frac{H_m^{(2)'}(k_0 n_2 a)}{H_m^{(2)}(k_0 n_2 a)} \end{aligned} \tag{2.17}$$

In both characteristic equations, the left-hand side term is given by the Bessel function J_m and its derivative, and the right-hand side term by the Hankel function $H_m^{(2)}$ and its derivative. If the argument is real, both equations can not be solved since a real value is obtained for J_m and a complex one for $H_m^{(2)}$ [7]. Therefore, the argument (the solution) must be a complex number. As it has been assumed that both media are lossless, the only option is that the resonance frequencies present an imaginary part different from zero.

$$\omega = \omega' + \jmath\omega''; \qquad e^{\jmath\omega t} = e^{\jmath\omega' t} e^{-\omega'' t} \tag{2.18}$$

From a physical point of view, that implies that the WGMs are inherently leaky, since there exists an exponential attenuation of the electromagnetic field with the time. This is in accordance with the fact that the radial part of the field in region II is a radiation mode. For the purposes of this work, only the real part of the characteristic equations, which gives information of the resonance frequencies, is studied in detail. The complex part is used to estimate the intrinsic radiation losses.

From Eqs. (2.17), each polarization state is ruled by its own transcendental equation that must be solved numerically for k_0. Thus, for a given azimuthal order, set by the m-value, the solutions consist on a series of discrete wavelengths, which correspond to different radial orders, l. While the value of m is the number of wavelengths that matches the optical path in one round trip, the value of l refers to the radial distribution of the WGMs electromagnetic field in the MR.

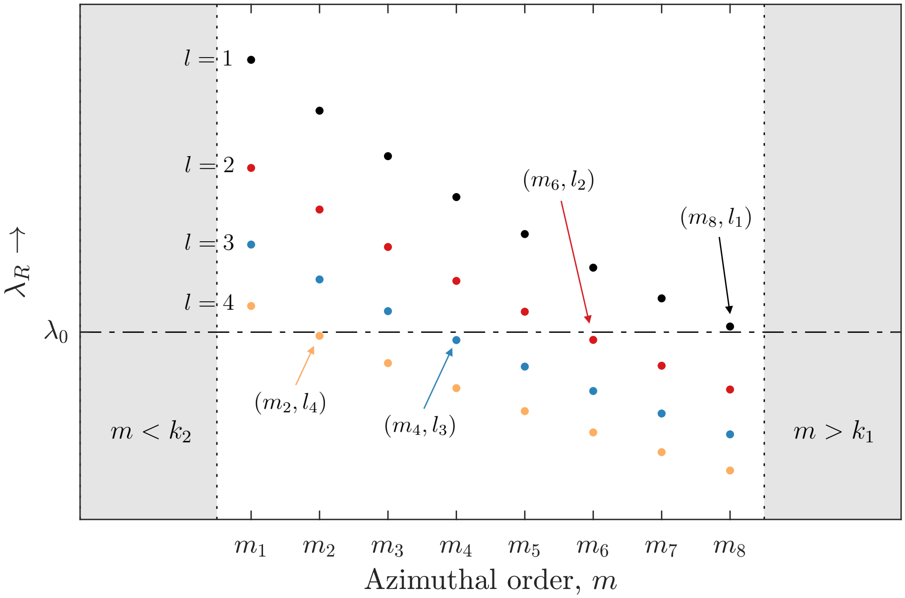

Figure 2.3: Typical dispersion curve of a cylindrical dielectric MR. WGMs resonant wavelengths as a function of the azimuthal order, m, for the first four radial orders, l.

When we solve the characteristic equations for a typical cylindrical dielectric MR, we obtain the dispersion curves of the WGM resonances, as it is shown in Fig. 2.3. To analyze these curves, first, we rewrite the resonant condition of the modes attending to the discretization of the azimuthal propagation constant β_ϕ, given by the Eq. (2.7):

$$\lambda_R = \frac{2\pi}{m} n_{\text{eff}} a \tag{2.19}$$

where n_{eff} is the effective refractive index of the WGM resonance [9], i. e., the mode refractive index determined by the phase velocity of the mode at $\rho = a$. We will make some remarks by taking into account Eq. (2.19):

(i) For a given radial order, l, the resonant wavelength decreases with the azimuthal order, m. This can be clearly understood when we consider that the field distribution of the modes for a particular radial order is similar, as it was pointed out before. This implies that their effective indices are also similar, see Fig. 2.4.

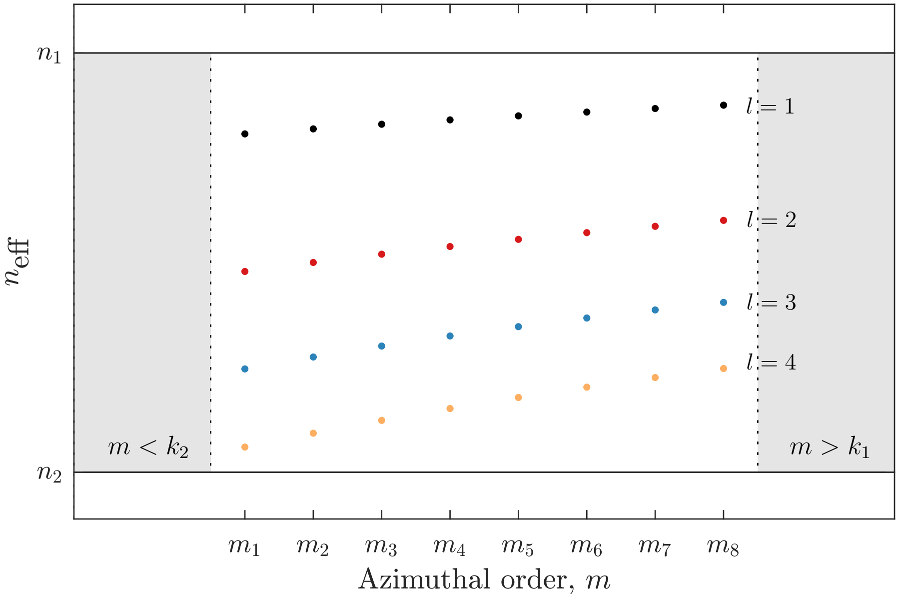

Figure 2.4: Effective index curves for a typical cylindrical microresonator.

(ii) For a given azimuthal order, m, the resonant wavelength decreases as a function of the radial order, l. Higher radial orders mean fields more spread in the outer medium, which leads to a lower effective index, see Fig. 2.4.

(iii) For a particular wavelength, λ_0, there exist different resonances with different azimuthal and radial orders (m_i, l_i), whose resonant wavelengths are centered at the vicinities of λ_0. The resonances with lower radial order are those with an azimuthal order close to the upper limit of m for λ_0, Eq. (2.8). Generally, the resonances with the highly confined fields present lower losses, thus, they are the most interesting ones. The equation of the allowed values of the propagation constant, Eq. (2.10), for the WGMs with the lowest losses, can be rewritten as it follows:

$$k_2 a \ll m \lesssim k_1 a \tag{2.20}$$

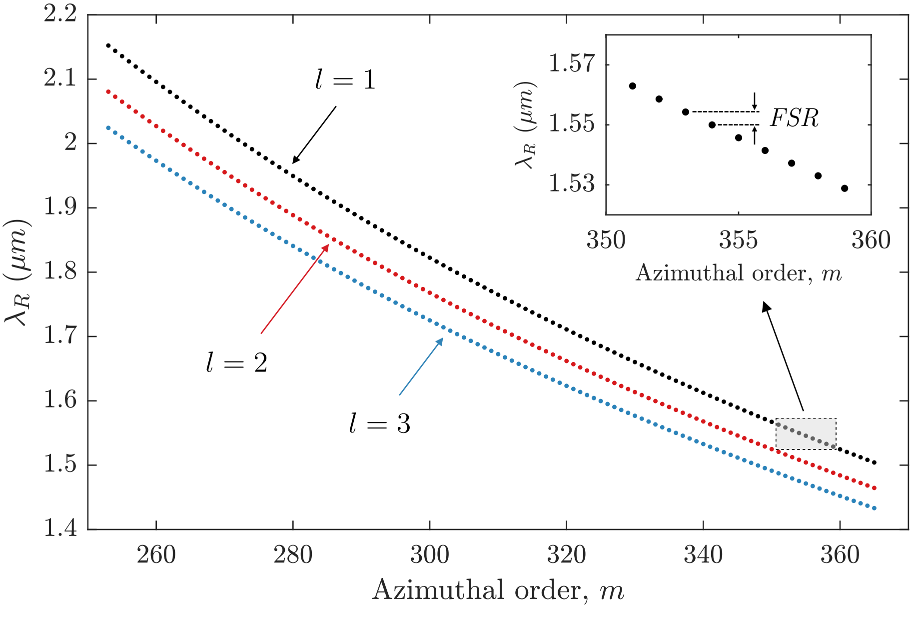

Figure 2.5: Resonant wavelengths of the TM-WGMs of a silica cylindrical MR with a diameter of 125 µm. The first three radial orders, l, are shown.

In this work, the MRs are usually silica cylindrical dielectric rods with a diameter of 125 µm (a bare optical fiber) immersed in air. For the simulations of the dispersion curves and the field distribution, the medium of the resonator is considered isotropic. Although a discussion with an anisotropic permittivity is carried out in the following chapters. Figure 2.5 shows the resonant wavelengths for the first three radial orders, as a function of the azimuthal order m, for TM polarization. For the calculations of the dispersion curves, Sellmeier dispersion of silica is taken into account for the refractive index of the material, n_1 [10]. The curves of the TE polarization follow the same trend, but the values of the resonant wavelengths are slightly shifted. Thus, the resonances for each polarization are not usually overlapped in wavelength. For example, for the azimuthal order $m = 354$ and the first radial order, $l = 1$, the resonant wavelengths of both polarization families are: $\lambda^{\mathrm{TM}} = 1549.98$ nm, $n_{\mathrm{eff}}^{\mathrm{TM}} = 1.3972$; $\lambda^{\mathrm{TE}} = 1546.96$ nm, $n_{\mathrm{eff}}^{\mathrm{TE}} = 1.3945$.

As it has been mentioned, the field of the first radial orders is well confined at the interface of the MR. This implies that the effective refractive index of the modes, n_{eff}, is very close to the refractive index of the material, n_1. By taking into account this assumption, the equation of the resonant condition, Eq. (2.19), can also be rewritten as:

$$\lambda_R \left(l \sim 1\right) \approx \frac{2\pi}{m} n_1 a \tag{2.21}$$

The above equation is very useful to estimate the spectral position of the WGM resonances without solving the characteristic equations. With Eq. (2.21), it is easy to demonstrate that the Free Spectral Range (FSR) can be described by the expression:

$$\mathrm{FSR} \left(l \sim 1\right) \approx \frac{\lambda_R^2}{2\pi n_1 a} \tag{2.22}$$

For the particular case of a silica microresonator of $125\,\mu\mathrm{m}$, Fig. 2.5, the wavelength separation of two consecutive azimuthal orders is: FSR ~ 4 nm. It is important to point out that the shift between the TE and TM modes is lower than the FSR.

Once we calculated the resonant wavelengths, and the constants A_i and B_i derived from the boundary conditions, Eqs. (2.16), the distribution of the fields can be obtained. Figure 2.6 shows the amplitude of the electric field of a TM-WGM.

The azimuthal order of the mode is $m = 354$, and the radial order is $l = 1$; the resonant wavelength is $\lambda^{\mathrm{TM}} = 1549.98\,\mathrm{nm}$. As it can be seen, the field is tightly confined at the MR boundary: it spreads along $4\,\mu\mathrm{m}$ inside, and $0.5\,\mu\mathrm{m}$ outside. For a MR of this size and $1550\,\mathrm{nm}$ of optical wavelength, the azimuthal orders are relatively high. The optical fields vary sinusoidally in the azimuthal direction according to the value of m, thus a fast oscillation of the amplitude can be observed along the ϕ coordinate.

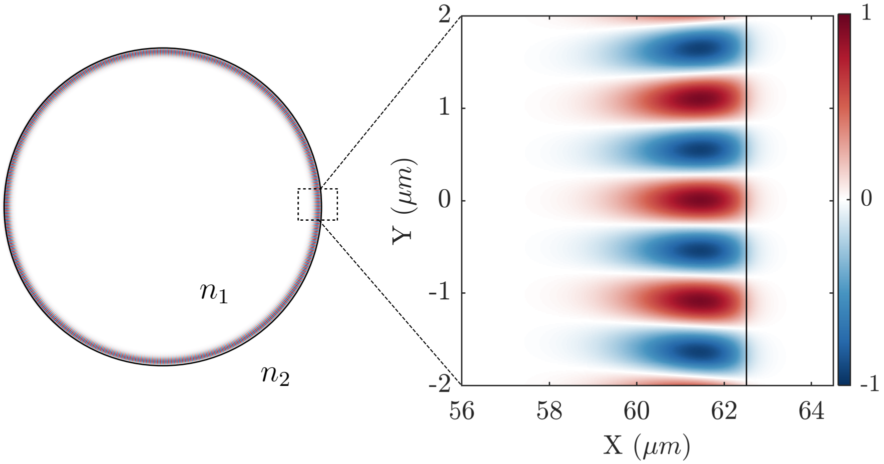

Figure 2.6: Electric field amplitude of the $m = 354$, $l = 1$ TM-WGM in a cylindrical silica MR of $125\,\mu\mathrm{m}$ diameter ($n_2 = 1$). The black circumference and line represent the interface $\rho = a$.

Figure 2.7 shows the electric field amplitude of several TM-WGMs as a function of the radial coordinate, for $m = 354$ and several radial orders. As it can be observed, for the first radial orders ($l = 1, 2, 3$), the optical field is localized close to the interface of the MR, and shows a weak evanescent tail in the outer region. A high radial order ($l = 23$) is represented to show the radiating behavior of the WGM in the outer medium. Also, it should be noted that, as the radial order increases, the field spreads inside the resonator, and the evanescent tail (and the radiative contribution) in the outer medium becomes larger, which leads to higher losses of the WGM.

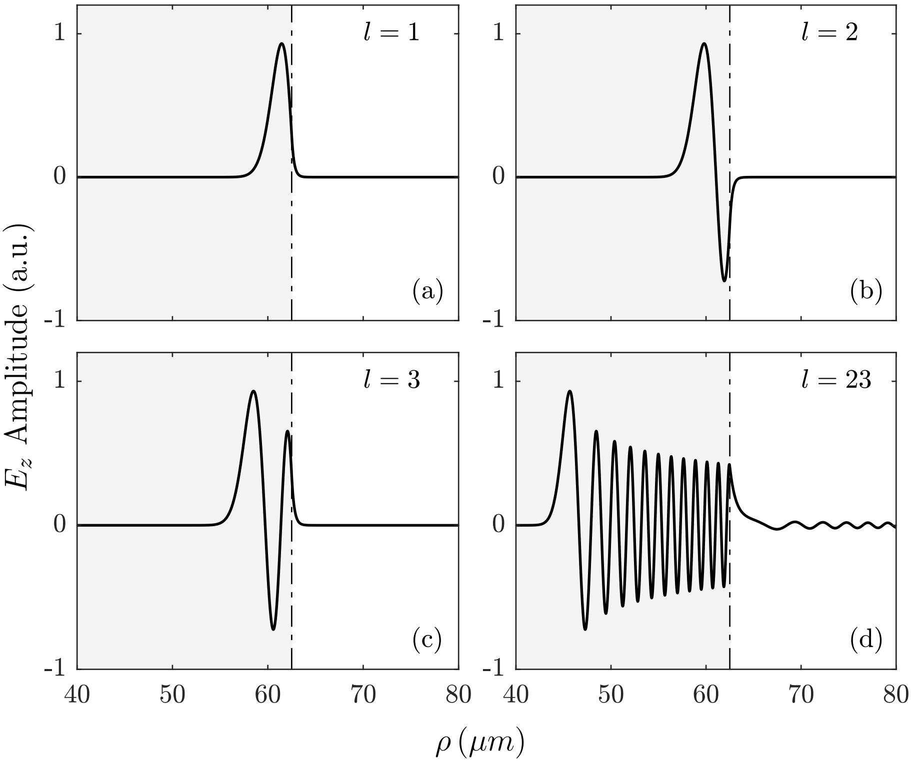

Figure 2.7: Electric field amplitude of the $m = 354$ TM-WGM as a function of the radial coordinate ρ in a cylindrical silica MR of 125 µm diameter ($n_2 = 1$). Radial order: (a) $l = 1$, (b) $l = 2$, (c) $l = 3$, (d) $l = 23$.

In order to show the details of the field as a function of the azimuthal coordinate, the field of a TM-WGM of low azimuthal order ($m = 25$) in a cylindrical silica MR of 10 µm diameter is calculated. This configuration allows an easy visualization of the field oscillations in the interface, and its evanescent and radiating components. Figure 2.8a shows the amplitude of the mode $m = 25$ and $l = 1$ in the cross section of the MR. Figure 2.8b shows the radial distribution of the same mode inside and outside of the MR.

Regarding the size of the MRs, the smaller the radius, the higher the radiation losses, since the EM field is pourer confined. In addition, as the MR size decreases, the efficient resonances shift to the blue side of the spectrum.

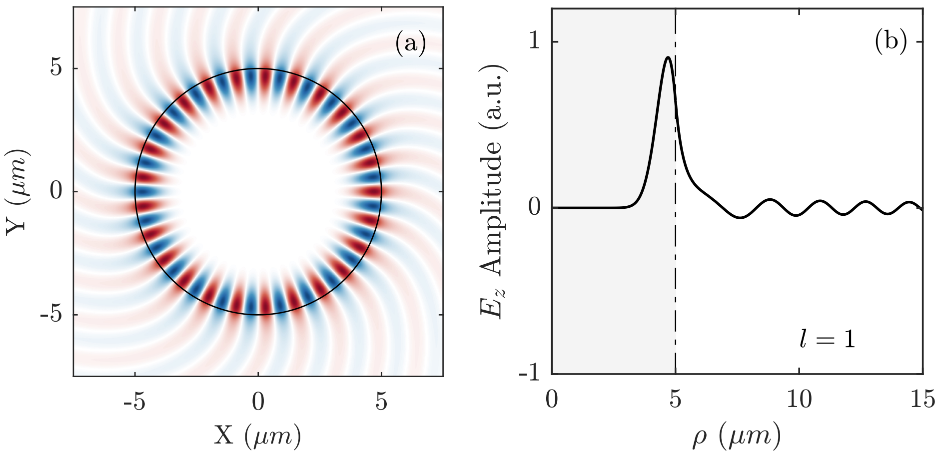

Figure 2.8: Electric field amplitude of the $m = 25$, $l = 1$ TM-WGM in a cylindrical silica MR of $10\,\mu\text{m}$ diameter ($n_2 = 1$). (a) Cross section field; (b) Amplitude as a function of the radial coordinate.

2.2 WGMs in gyrotropic cylindrical microresonators

In this section, we describe the propagation of WGMs in materials with optical activity, also known as gyrotropic materials. Historically, the optical activity, or rotatory power, it is known as the ability of some media (crystals, liquids or gases) to rotate the plane of polarization of light propagating through it. This phenomenon was discovered at the beginning of the XIX century by Arago. From a macroscopic point of view, the optical activity has its origin in the spatial dispersion of the permittivity tensor, that implies that the polarization of the light at a given point depends on more than one component of the wavevector. The general expression of the gyrotropic anisotropy of the permittivity tensor can be written as follows [11]:

$$\Delta\bar{\varepsilon} = \begin{pmatrix} 0 & \jmath G_{33} & -\jmath G_{23} \\ -\jmath G_{33} & 0 & \jmath G_{13} \\ \jmath G_{23} & -\jmath G_{13} & 0 \end{pmatrix} \tag{2.23}$$

where G_{ij} are the components of the gyrotropic tensor. The number of non-zero components depends on the spatial dispersion of the medium.

In dielectric isotropic materials, such as fused silica (which is the material we use for our experiments), there does not exist a natural optical activity, but the same type of anisotropy can be induced by the presence of an external magnetic field (magneto-optic effect). The anisotropy introduced by the magneto-optic effect depends on the direction of the magnetic field [12]:

$$\varepsilon_{ij}(\mathbf{B}) = \varepsilon_{ij}^{(0)} + \Delta\varepsilon_{ij}(\mathbf{B}) = \varepsilon_{ij}^{(0)} + \jmath \sum_{k} f_{ijk} B_k \tag{2.24}$$

where f_{ijk} are the magneto-optic coefficients of first order, and $\varepsilon_{ij}^{(0)}$ is the isotropic permittivity tensor. In the case of a magnetic field in the axial direction of the cylindrical MR, the Eq. (2.23) can be rewritten as follows:

$$\bar{\boldsymbol{\varepsilon}} = \begin{pmatrix} \varepsilon_1 & \jmath\xi & \\ -\jmath\xi & \varepsilon_1 & \\ & & \varepsilon_1 \end{pmatrix} \tag{2.25}$$

where $\xi = f_z B_z$ is the anisotropy induced by the magnetic field in the axial direction (we will consider a linear dependence of the anisotropy with the external magnetic field). The value of ξ depends on the material studied (this is, on the value of the magneto-optical coefficient), and on the intensity of the magnetic field. The coefficient f_z is directly related with the Verdet constant, v, which describes the rotatory strength of the medium. The relation is given by: $f_z = \lambda/\pi \cdot n_1 v(\lambda)$.

Analogously to the previous section, we will solve Maxwell's equations using the expression of the WGM fields, see Eqs. (2.1), and the permittivity tensor given by Eq. (2.25). By solving the two wave equations, and considering the constraints required to have WGM resonances, we will obtain the electromagnetic field for both polarization states:

TM modes

- *Region I* ($\rho < a$):

$$\begin{aligned}
E_z^I &= A_1 J_m(k_0 n_1 \rho) e^{-\jmath m\phi} e^{\jmath\omega t} \\
H_\rho^I &= \frac{m}{\omega\mu_0}\frac{1}{\rho} A_1 J_m(k_0 n_1 \rho) e^{-\jmath m\phi} e^{\jmath\omega t} \\
H_\phi^I &= \frac{k_0 n_1}{\jmath\omega\mu_0} A_1 J_m'(k_0 n_1 \rho) e^{-\jmath m\phi} e^{\jmath\omega t} \\
E_\rho^I &= E_\phi^I = H_z^I = 0
\end{aligned} \tag{2.26}$$

- *Region II* ($\rho > a$):

$$\begin{aligned}
E_z^{II} &= A_2 H_m^{(2)}(k_0 n_2 \rho) e^{-\jmath m\phi} e^{\jmath\omega t} \\
H_\rho^{II} &= \frac{m}{\omega\mu_0}\frac{1}{\rho} A_2 H_m^{(2)}(k_0 n_2 \rho) e^{-\jmath m\phi} e^{\jmath\omega t} \\
H_\phi^{II} &= \frac{k_0 n_2}{\jmath\omega\mu_0} A_2 H_m^{(2)\prime}(k_0 n_2 \rho) e^{-\jmath m\phi} e^{\jmath\omega t} \\
E_\rho^{II} &= E_\phi^{II} = H_z^{II} = 0
\end{aligned} \tag{2.27}$$

TE modes

- *Region I* ($\rho < a$):

$$\begin{aligned}
H_z^I &= B_1 J_m(k_0 n_1 \rho) e^{-\jmath m\phi} e^{\jmath\omega t} \\
E_\rho^I &= \frac{B_1}{(\varepsilon_1^2 - \xi^2)}\frac{1}{\jmath\omega\varepsilon_0}\left[\frac{-\jmath m\varepsilon_1}{\rho} J_m(k_0 n_1 \rho) + \jmath\xi k_0 n_1 J_m'(k_0 n_1 \rho)\right] e^{-\jmath m\phi} e^{\jmath\omega t} \\
E_\phi^I &= \frac{B_1}{(\varepsilon_1^2 - \xi^2)}\frac{1}{\jmath\omega\varepsilon_0}\left[\frac{\xi m}{\rho} J_m(k_0 n_1 \rho) - \varepsilon_1 k_0 n_1 J_m'(k_0 n_1 \rho)\right] e^{-\jmath m\phi} e^{\jmath\omega t} \\
H_\rho^I &= H_\phi^I = E_z^I = 0
\end{aligned} \tag{2.28}$$

- *Region II* ($\rho > a$):

$$\begin{aligned} H_z^{II} &= B_2 H_m^{(2)}(k_0 n_2 \rho) e^{-\jmath m\phi} e^{\jmath\omega t} \\ E_\rho^{II} &= -\frac{m}{\omega\varepsilon_0\varepsilon_2}\frac{1}{\rho} B_2 H_m^{(2)}(k_0 n_2 \rho) e^{-\jmath m\phi} e^{\jmath\omega t} \\ E_\phi^{II} &= -\frac{k_0 n_2}{\jmath\omega\varepsilon_0\varepsilon_2} B_2 H_m^{(2)'}(k_0 n_2 \rho) e^{-\jmath m\phi} e^{\jmath\omega t} \\ H_\rho^{II} &= H_\phi^{II} = E_z^{II} = 0 \end{aligned} \tag{2.29}$$

As it can be observed, only the TE polarization is affected by the gyrotropic anisotropy induced by the external magnetic field in the axial direction. The behavior of the TM polarization is the same than in an isotropic medium, independently of the value of ξ (this is, of B_z). Thus, the magneto-optic phenomenon in a WGM MR with an external magnetic field in the axial direction does not show up for TM polarization. By applying the boundary conditions that forces the continuity of the tangential components of the electromagnetic field at the interface ($\rho = a$), Eq. (2.16), we obtain the characteristic equations for both polarizations:

$$\begin{aligned} &\textbf{TM:} \quad n_1 \frac{J_m'(k_0 n_1 a)}{J_m(k_0 n_1 a)} = n_2 \frac{H_m^{(2)'}(k_0 n_2 a)}{H_m^{(2)}(k_0 n_2 a)} \\ &\textbf{TE:} \quad \frac{1}{(n_1^4 - \xi^2)} n_1^3 \frac{J_m'(k_0 n_1 a)}{J_m(k_0 n_1 a)} + \frac{1}{(n_1^4 - \xi^2)} \frac{\xi m}{k_0 a} = \frac{1}{n_2} \frac{H_m^{(2)'}(k_0 n_2 a)}{H_m^{(2)}(k_0 n_2 a)} \end{aligned} \tag{2.30}$$

Since TM modes are not affected by the presence of a B_z external field, the description for the TM-WGMs presented in the previous section is still valid. However, for the TE-WGMs, the gyrotropic anisotropy must be taken into account. As we mentioned before, the value of ξ is a small coefficient for dielectric materials as silica. This allows us to introduce the external magnetic field as a perturbation in the TE-WGMs characteristic equation. Thus, we can write the first-order approximation for the relative shift of the resonances:

$$\Delta\lambda_R \propto f_z \cdot m \cdot \Delta B_z \tag{2.31}$$

As it can be observed in Eq. (2.31), for a given direction of the external magnetic field, the sign of m (direction of propagation of the WGMs) changes the sign of the resonant wavelength shift, showing up the non-reciprocal nature of the magneto-optic effect. In Fig. 2.9 is depicted an example of the different shifts suffered by the two counter-propagating WGM resonances due to a magnetic field in the axial direction, B_z. Depending on whether the resonances propagate in the $+\hat{\boldsymbol{u}}_\phi$ or $-\hat{\boldsymbol{u}}_\phi$ direction, the shift is towards longer or shorter wavelengths respectively. In a practical application, WGM resonances will be excited in one of these directions (for example $+\hat{\boldsymbol{u}}_\phi$), but because of scattering on the surface of the MR, the counter-propagating WGM will be excited as well, as we will describe in further sections.

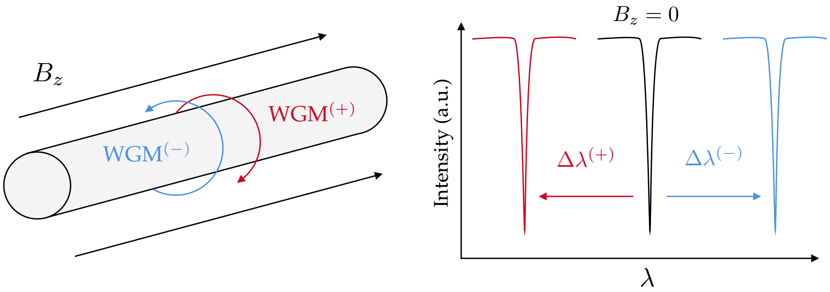

Figure 2.9: Schematic representation of two counter-propagating WGM resonances shift due to an external magnetic field.

If we solve the TE-WGM characteristic equation for a cylindrical, silica MR with: $a = 62.5\,\mu\text{m}$, $n_2 = 1$, $v = 0.54\,\text{rad}\cdot\text{m}^{-1}\cdot\text{T}^{-1}$ (Verdet constant at 1523 nm) [13]; as a function of the external magnetic field, we obtain, for a given value of B_z, a different shift depending on the sign of m. This is in accordance with the behavior predicted from Eq. (2.31). Figure 2.10 shows the shift of the mode with azimuthal order $m = \pm 366$ and radial order $l = 1$ as a function of the external magnetic field. As it can be observed, according to our calculations, the WGM resonances shift $\sim 0.4\,\text{fm}$ in a silica MR, for an external magnetic field of $B_z = 1\,\text{T}$. This value results to be much lower than the bandwidth of a typical WGM resonance in an optical fiber, thus it is not possible to measure it in standard experimental conditions.

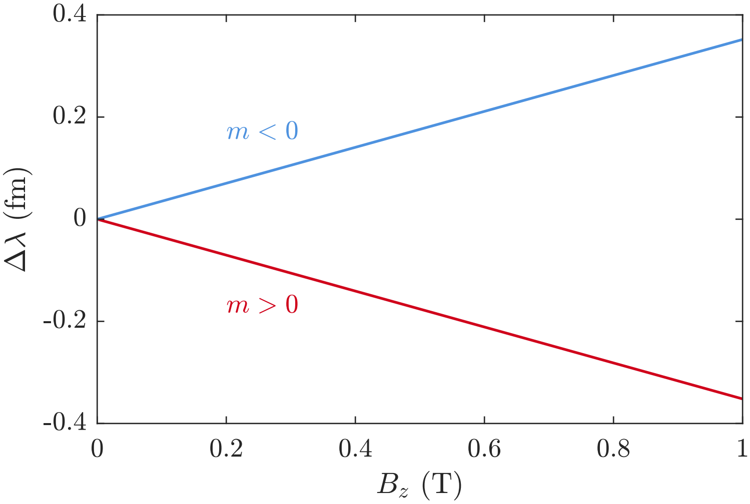

Figure 2.10: Wavelength shift of two counter-propagating TE-WGM resonances ($m = \pm = 366$, $l = 1$) in a silica MR due to an external magnetic field, B_z.

To observe experimentally the magneto-optic effect by means of the WGM resonances shift, it would be necessary to use a resonator material with a higher Verdet constant than the silica, which is the main limitation for the measurement. It has been reported that TGG (Terbium Gallium garnet) materials, a silicate with low absorption coefficient in the visible and infrared spectral ranges, show a high Verdet constant. For example, a TGG material doped with Dy^{3+} presents $v = 256.8\,\mathrm{rad} \cdot \mathrm{m}^{-1} \cdot \mathrm{T}^{-1}$ at 532 nm [14], which is ~ 57 times larger than the value for the silica at a similar wavelength. This v constant would lead to a wavelength shift of $\sim 160\,\mathrm{fm/T}$. In this case, we would obtain a shift of the WGM resonances that could be observed be means of our experimental technique. In addition, one could measure the relative shift of two counter-propagating WGM resonances to double the total $\Delta\lambda$. This is, the wavelength distance between the transmitted and reflected resonance.

Unfortunately, at the moment, we do not have available MRs of these material, thus the experimental characterization of this effect will be left for future works.

2.3 WGMs Quality factor

One of the most important parameters that describes the performance of any resonator is the quality factor, which is defined as the ratio between energy stored in the resonator, U_{loaded}, and the energy dissipated per cycle, U_{loss}:

$$Q = \omega_0 \frac{U_{\text{loaded}}}{U_{\text{loss}}} = \omega_0 \tau = \frac{\omega_0}{\Delta\omega} \tag{2.32}$$

where τ is the time required for the energy stored to decay a factor e, and $\Delta\omega = \tau^{-1}$ is the full width at half maximum of the resonance.

The energy can be dissipated due to many loss sources, wether intrinsic or external to the resonator. By considering the independent contributions, the Q-factor can be written as [15]:

$$Q^{-1} = Q_0^{-1} + Q_{\text{ext}}^{-1} = \left(Q_{\text{rad}}^{-1} + Q_{\text{mat}}^{-1} + Q_{\text{scatt}}^{-1} + Q_{\text{cont}}^{-1}\right) + Q_{\text{ext}}^{-1} \tag{2.33}$$

where Q_{rad}^{-1} denotes radiative losses; Q_{mat}^{-1} accounts for the material absorption; Q_{scatt}^{-1} refers to scattering losses due to residual surface inhomogeneities; Q_{cont}^{-1} represents the losses introduced by surface contaminants; Q_{ext}^{-1} considers the external losses such as coupling losses. The Q-factor value is limited by the largest loss source. Although a detailed theoretical or experimental study is not pretended in this work, we will give an estimation of the different loss sources.

The value for Q_{rad} can be obtained by solving both the real and imaginary parts of the characteristic equations, Eqs. (2.17).

$$Q_{\text{rad}} = \frac{1}{2}\left(\frac{\omega'}{\omega''}\right) \tag{2.34}$$

where ω' and ω'' are given in the Eq. (2.18). Since the value of the Q_{rad} is associated to the radiation due to frustrated total internal reflection in a curved surface, the radiation losses will decrease as the radius of the resonator increases. Figure 2.11 shows how the Q-factor increases dramatically (note the logarithmic scale) as the radius of the MR becomes larger (the curvature of the surface decreases). For the MRs treated in this work ($a = 62.5\,\mu\text{m}$), the losses associated to the radiation are negligible.

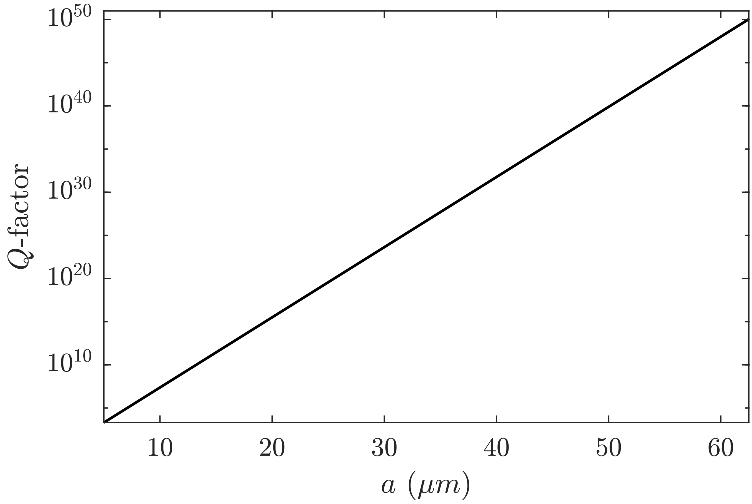

Figure 2.11: Value of Q_{rad} as a function of the radius for a cylindrical, silica MR.

The value of the Q_{mat} is related with the absorption of the resonator material. For silica, at a working wavelength of $\lambda_0 = 1.55\,\mu\text{m}$, the absorption is $\alpha = 0.17\,\text{dB/km}$. The Q-factor can be calculated with:

$$Q_{\text{mat}} = \frac{2\pi n_1}{\alpha\lambda} \tag{2.35}$$

The value for the resonators employed in this work is estimated to be in the order of $Q_{\text{mat}} \sim 10^{11}$.

The value of Q_{scatt} is associated with Rayleigh scattering by molecular-sized inhomogeneities, and can be estimated as follows:

$$Q_{\text{scatt}} = \frac{\lambda^2 a}{\pi^2 \sigma^2 B} \tag{2.36}$$

where σ is the rms size and B is the correlation length of surface inhomogeneities. For a fused silica resonator ($\sigma = 0.3\,\text{nm}$, $B = 3\,\text{nm}$), $Q_{\text{scatt}} \sim 10^{10}$.

The value of the Q_{cont} depends on the losses introduced by surface contaminants, mainly OH groups chemically bound to the surface due to the absorption of atmospheric water. The value is limited to: $Q_{\text{cont}} \sim 10^9$.

The last contribution, Q_{ext}, refers to any loss that is not present if the resonator is studied as an isolated system. Usually, it is associated with the coupling losses and, in the experiments, it will determine the fraction of energy coupled from the optical source to the MR.

As it can be observed, the loss sources that limit the highest value of the Q-factor of our MR (silica resonator with $125\,\mu\text{m}$ diameter) are the surface contaminants and the existent coupling losses.

2.4 Coupling microfiber-microresonator

As it has been shown in the previous section, silica MRs exhibit intrinsically high Q-factors. Achieving an efficient coupling is crucial to observe high-Q WGM resonances. There exists different techniques to couple light from a waveguide structure to a resonator. In this work, we will consider a theoretical approach where a microfiber is employed to couple the energy into the MR. Figure 2.12 shows a scheme of the coupling structure. The system consists on an input field, E_i, guided in the microfiber coupled to the MR. The coupling strength between the cavity and the waveguide is given by η and depends on the overlapping of the microfiber and MR fields. Due to the coupling, a WGM propagating in the counter-clockwise direction is excited, E_{ccw}. Besides, as a result of inhomogeneities distributed in the surface of the resonator, the counter-clockwise WGM excites a WGM propagating in the clockwise direction, E_{cw} [16]. The coupling coefficient between the two counter propagating WGM due to the inhomogeneities is given by g. The transmitted field of the microfiber is E_t, while the reflected field, excited by the coupling of the backscattered clockwise WGM, is E_r.

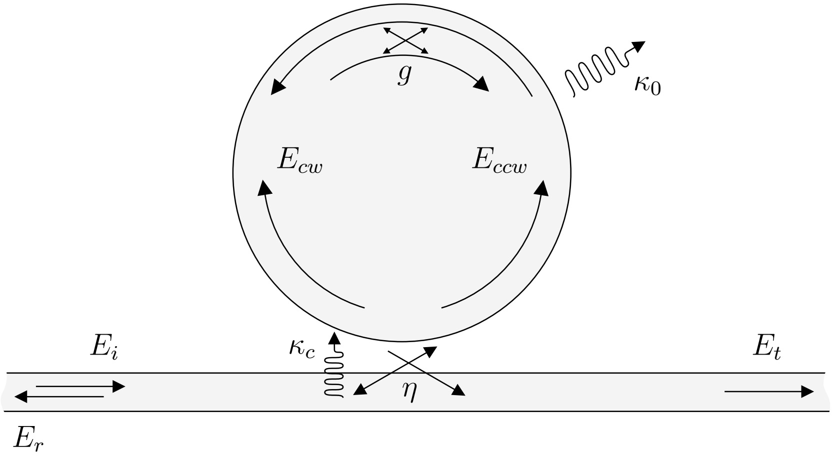

Figure 2.12: Scheme of the phenomena occurring in the coupling between the fields of a microfiber and WGMs in a MR.

In a silica MR of 125 μm diameter, the intrinsic Q-factor is mainly affected by the material, scattering and surface contaminants losses. In the following calculations, an exponential decay of the WGMs field with the time is considered, $E_{\text{WGM}} \propto e^{-\kappa_0 t}$, where $\kappa_0 = \omega/2Q_0$ is defined as the cavity decay rate [17]. The coupling rate is described by $\kappa_c = \eta^2/2\tau = \omega/2Q_c$. Besides, the phase of the field is given by the resonant frequency and its detuning, $E_{\text{WGM}} \propto e^{\jmath(\omega_R+\delta\omega)t}$. Each roundtrip phase shift, since constructive interference is assumed, can be written as: $\theta = \delta\omega\tau$, where τ is the circulating time.

Therefore, the coupled mode equations for the fields can be expressed as follows, [18]:

$$\begin{aligned}
E_{ccw}(t) &= \jmath\eta E_i(t) + \sqrt{1-\eta^2}E_{ccw}(t-\tau)e^{-\kappa_0\tau}e^{\jmath\delta\omega\tau} + \jmath g\tau E_{cw}(t)\\
E_{cw}(t) &= \jmath g\tau E_{ccw}(t) + \sqrt{1-\eta^2}E_{cw}(t-\tau)e^{-\kappa_0\tau}e^{\jmath\delta\omega\tau}\\
E_r(t) &= \jmath\eta E_{cw}(t)\\
E_t(t) &= \sqrt{1-\eta^2}E_i(t) + \jmath\eta E_{ccw}(t)
\end{aligned} \tag{2.37}$$

Now, if $\psi(t-\tau) \approx \psi(t) - \tau(d\psi/dt)$, and considering small values for the losses, the coupling strength and the circulating time, the above equations can be rewritten as:

$$\begin{aligned}
\frac{dE_{ccw}}{dt} &= -\left(\kappa_0 + \kappa_c - \jmath\delta\omega\right)E_{ccw}(t) + \jmath\frac{\eta}{\tau}E_i + \jmath g E_{cw}(t)\\
\frac{dE_{cw}}{dt} &= -\left(\kappa_0 + \kappa_c - \jmath\delta\omega\right)E_{cw}(t) + \jmath g E_{ccw}(t)\\
E_r(t) &= \jmath\eta E_{cw}(t)\\
E_t(t) &= \sqrt{1-\eta^2}E_i(t) + \jmath\eta E_{ccw}(t)
\end{aligned} \tag{2.38}$$

In the case of the stationary solution, the transmittance and reflectivity of the system can be derived:

$$\begin{aligned}
T(\omega) &= \left|\frac{E_t}{E_i}\right|^2 = \left|\sqrt{1-\eta^2} - \frac{2\kappa_c\left(\kappa_0+\kappa_c-\jmath\delta\omega\right)}{\left(\kappa_0+\kappa_c-\jmath\delta\omega\right)^2+g^2}\right|^2\\
R(\omega) &= \left|\frac{E_r}{E_i}\right|^2 = \left|\frac{2\kappa_c g}{\left(\kappa_0+\kappa_c-\jmath\delta\omega\right)^2+g^2}\right|^2
\end{aligned} \tag{2.39}$$

In experimental conditions, the value of κ_0 is given by the intrinsic losses of the resonator, and the value of g by the inhomogeneities of the surface. Therefore, the value of κ_c is the one that can be controlled experimentally, generally by changing the distance between the microfiber and the MR.

When considering that there is no surface roughness ($g = 0$), it is easy to identify three different coupling scenarios:

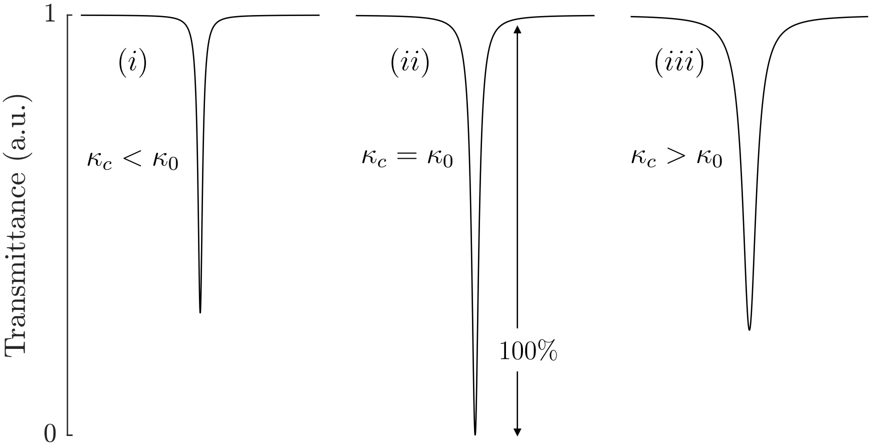

Figure 2.13: Example of different coupling regimes: (i) undercoupling; (ii) critical coupling; (iii) overcoupling.

(i) When $\kappa_c < \kappa_0$: undercoupling. The energy coupled from the microfiber to the MR is smaller than the energy lost by the different loss sources. The value of the transmittance is: $0 < T(\omega_R) < 1$.

(ii) When $\kappa_c = \kappa_0$: critical coupling. The coupling rate is equal to the resonator losses. The energy transfered from the microfiber to the MR is maximal. The value of the transmittance at the resonant wavelength is: $T(\omega_R) = 0$. However, if the transmittance in Eq. (2.39) is calculated for $g = 0$, $\kappa_c = \kappa_0$, $T(\omega_R)$ is not exactly null. This is because, in our theoretical approach, the losses, the coupling strength, and the circulating time have been approximated by Taylor to first order. If we had not considered such approximation, the value of $T(\omega)$ in ω_R would be exactly zero [19].

(iii) When $\kappa_c > \kappa_0$: overcoupled. The energy coupled is greater that the losses and is re-coupled to the microfiber. The value of the transmittance is: $0 < T(\omega_R) < 1$.

For those cases where the surface inhomogeneities are considered ($g \neq 0$), the critical coupling is obtained when $k_c = \sqrt{k_0^2 + g^2}$.

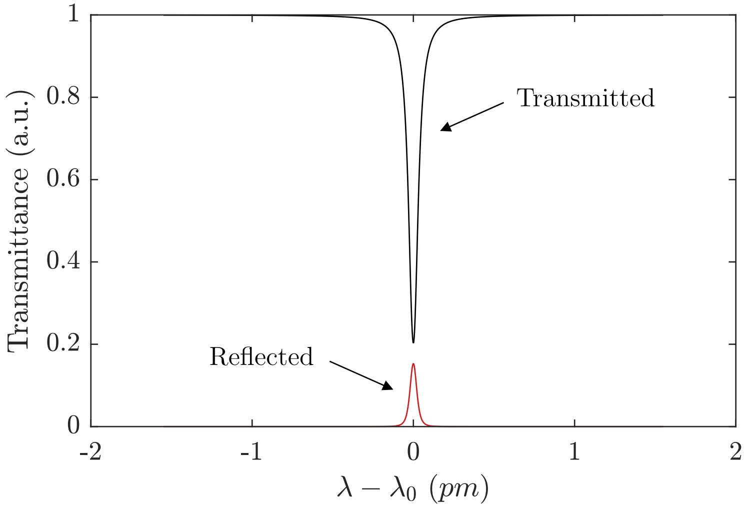

Figure 2.14: Calculated transmittance and reflectivity for a MR with $a = 62.5$ µm, $\lambda = 1.55$ µm, $Q_0 = 10^8$, $Q_c = 2.8 \cdot 10^7$ and $g\tau = 1.4 \cdot 10^{-5}$.

Figure 2.14 shows the transmittance and the reflectivity of a WGM resonance in a MR ($a = 62.5$ µm) where a microfiber has been used to excite the mode. The working wavelength is $\lambda = 1.55$ µm. The coupling is in the overcoupling regime ($\kappa_c = 3.5\kappa_0$). Thus, the transmitted light is not minimal, for the parameters considered, $T(\lambda_0) = 0.2$. Adjusting $g\tau$, the reflected light is $R(\lambda_0) = 0.15$.

From the values of Q_c and Q_0, and taking into account Eq. (2.33), it is possible to calculate the Q-factor of the resonance shown in Fig. 2.14, $Q \sim 2.2 \cdot 10^7$. Frequently, in the experiments, the coupling system is in overcoupling or undercoupling regime. This implies that the Q-factor of the WGM resonance is limited by the external losses (coupling losses for this particular case).

Although the coupling strength is a very small coefficient, in a coupling system as the one discussed in this section, the energy transfer from the microfiber to the MR can be virtually 100%. The reason for this relies on the interference between the optical fields of the WGMs and the modes guided by the microfiber. Each round trip there is a constructive, self-interference of the WGM, that leads to an amplification of the WGM field in a stationary regime. Contrarily, the non-constructive interference between the WGM and the microfiber modes, E_{ccw} and E_i, leads to to the fact that the transmitted field, E_t, can be zero.

Besides, since the quality factor of this type of MRs is high, even small surface imperfections (a small coefficient $g\tau$) can induce a strong coupling of a counter propagating wave, which leads to a significant reflectivity in experimental conditions, with practical applications, as we will see in further chapters.

2.5 Guided modes in dielectric rods

The structure represented in Fig. 2.1 supports several types of guided modes. WGMs is just one of them. In this section, we will present a detailed description of all the families of modes that such structure can guide. For the description, a more general expression for the electromagnetic field than the considered for the WGMs, Eq. (2.1), must be treated [20]:

$$\begin{aligned}\mathbf{E}(\mathbf{r},t) &= \mathbf{e}(\rho)e^{-\jmath\beta_\phi\phi}e^{-\jmath\beta_z z}e^{\jmath\omega t}\\ \mathbf{H}(\mathbf{r},t) &= \mathbf{h}(\rho)e^{-\jmath\beta_\phi\phi}e^{-\jmath\beta_z z}e^{\jmath\omega t}\end{aligned} \tag{2.40}$$

where β_i are the azimuthal and axial components of the guided mode wave vector. By solving Maxwell's equations considering the electromagnetic field given by Eqs. (2.40), and applying the proper boundary conditions to this problem, the following transcendental equation is obtained [4, 6, 8]:

$$\left[n_1^2\frac{J'_m(\gamma_1 a)}{(\gamma_1 a)J_m(\gamma_1 a)}+n_2^2\frac{K'_m(\bar{\gamma}_2 a)}{(\bar{\gamma}_2 a)K_m(\bar{\gamma}_2 a)}\right]\left[\frac{J'_m(\gamma_1 a)}{(\gamma_1 a)J_m(\gamma_1 a)}+\frac{K'_m(\bar{\gamma}_2 a)}{(\bar{\gamma}_2 a)K_m(\bar{\gamma}_2 a)}\right] - \frac{m^2\beta_z^2}{\mu_0\varepsilon_0\omega^2}\left[\frac{1}{(\gamma_1 a)^2}+\frac{1}{(\bar{\gamma}_2 a)^2}\right]^2 = 0 \quad (2.41)$$

where γ_1 and $\bar{\gamma}_2$ are given by:

$$\begin{aligned}\gamma_1 &\equiv \sqrt{k_0^2 n_1^2 - \beta_z^2}\\ \bar{\gamma}_2 &\equiv \sqrt{\beta_z^2 - k_0^2 n_1^2}\end{aligned} \quad (2.42)$$

By solving numerically this equation, we can find the solution for the different guided modes existent in a dielectric rod. They can be classified into three types:

(i) Modes with propagation purely in the azimuthal direction ($\beta_z = 0$).

This is the case of the WGMs. The axial component is null and, like in the previous case, the solutions split into the TE and TM polarization states. By taking into account the relations between the Bessel and Hankel functions [7], the characteristic equation can be rewritten as it follows:

$$\left[n_1\frac{J'_m(k_1 a)}{J_m(k_1 a)} - n_2\frac{H_m^{(2)'}(k_2 a)}{H_m^{(2)}(k_2 a)}\right]\left[\frac{1}{n_1}\frac{J'_m(k_1 a)}{J_m(k_1 a)} - \frac{1}{n_2}\frac{H_m^{(2)'}(k_2 a)}{H_m^{(2)}(k_2 a)}\right] = 0 \quad (2.43)$$

It is clear now that, as it was pointed out before, the existence of hybrid modes is not a solution to the characteristic equation of the WGMs in cylindrical MRs. In order to obtain the β_ϕ values correspondent to WGM resonances, the proper constraints, Eqs. (2.7) and (2.10), must be considered.

(ii) Modes with propagation purely in the axial direction ($\beta_\phi = m = 0$).

By considering the azimuthal component zero, we obtain the following transcendental equation, Eq. (2.44). The solutions to this equation split into two families, which corresponds to the TE and TM polarization.

$$\left[\frac{n_1^2 J_m'(\gamma_1 a)}{(\gamma_1 a) J_m(\gamma_1 a)} + \frac{n_2^2 K_m'(\bar{\gamma}_2 a)}{(\bar{\gamma}_2 a) K_m(\bar{\gamma}_2 a)}\right]\left[\frac{J_m'(\gamma_1 a)}{(\gamma_1 a) J_m(\gamma_1 a)} + \frac{K_m'(\bar{\gamma}_2 a)}{(\bar{\gamma}_2 a) K_m(\bar{\gamma}_2 a)}\right] = 0 \quad (2.44)$$

This includes some of the conventional modes used for guiding light in optical fibers.

(iii) Modes with $\beta_z \neq 0$ and $\beta_\phi \neq 0$.

Depending on which component of the wavevector is the dominant (β_z or β_ϕ), the solutions of the characteristic equation are considered as guided modes in the axial direction or spiral modes. When $\beta_z \gg \beta_\phi$, the solutions obtained, along with the $\beta_\phi = 0$ solutions, describe the conventional guided modes of an optical fiber. Moreover, these solutions describe the propagating modes of the microfibers employed to excite the WGMs. Contrarily, when $\beta_\phi \gg \beta_z$, the modes propagate as surface modes in the waveguide in a spiral trajectory. If the spiral WGMs fulfill the resonance conditions, secondary resonances located at the blue-side of the $\beta_z = 0$ resonances will appear [21].

References

[1] J. Krupka, D. Cros, M. Aubourg, and P. Guillon. *"Study of whispering gallery modes in anisotropic single-crystal dielectric resonators"*, IEEE Transactions on Microwave Theory and Techniques, **42**, pp. 56–61 (1994).

[2] A. Yariv and P. Yeh. *"Photonics: optical electronics in modern communications"*, Oxford University Press, New York Oxford (2007).

[3] M. Sumetsky. *"Mode localization and the Q-factor of a cylindrical microresonator"*, Optics Letters, **35**, pp. 2385–2387 (2010).

[4] K. Zhang and D. Li. *"Electromagnetic theory for microwaves and optoelectronics"*, Springer, Berlin (2008).

[5] N. H. Asmar. *"Partial differential equations and boundary value problems"*, Prentice Hall, Upper Saddle River, NJ (2000).

[6] A. Snyder and J. Love. *"Optical Waveguide Theory"*, Springer, US (1983).

[7] M. Abramowitz and I. A. Stegun. *"Handbook of mathematical functions, with formulas, graphs, and mathematical tables"*, Dover Publications, New York (1965).

[8] J. R. Wait. *"Electromagnetic whispering gallery modes in a dielectric rod"*, Radio Science, **2**, pp. 1005–1017 (1967).

[9] T. A. Birks, J. C. Knight, and T. E. Dimmick. *"High-resolution measurement of the fiber diameter variations using whispering gallery modes and no optical alignment"*, IEEE Photonics Technology Letters, **12**, pp. 182–183 (2000).

[10] M. Adams. *"An introduction to optical waveguides"*, Wiley, Chichester New York (1981).

[11] J. Cabrera. *"Óptica electromagnética"*, Addison-Wesley Iberoamericana España Universidad Autónoma de Madrid, Madrid (1998).

[12] W. Kuch. *"Magnetic microscopy of layered structures"*, Springer, Heidelberg (2014).

[13] J. L. Cruz, M. V. Andres, and M. A. Hernandez. *"Faraday effect in standard optical fibers: dispersion of the effective Verdet constant"*, Applied Optics, **35**, pp. 922–927 (1996).

[14] Z. Chen, L. Yang, Y. Hang, and X. Wang. *"Faraday effect improvement by Dy3+-doping of terbium gallium garnet single crystal"*, Journal of Solid State Chemistry, **233**, pp. 277–281 (2016).

[15] M. L. Gorodetsky, A. A. Savchenkov, and V. S. Ilchenko. *"Ultimate Q of optical microsphere resonators"*, Optics Letters, **21**, pp. 453–455 (1996).

[16] T. J. Kippenberg, S. M. Spillane, and K. J. Vahala. *"Modal coupling in traveling-wave resonators"*, Optics Letters, **27**, pp. 1669–1671 (2002).

[17] C.-L. Zou, Y. Yang, C.-H. Dong, Y.-F. Xiao, X.-W. Wu, Z.-F. Han, and G.-C. Guo. *"Taper-microsphere coupling with numerical calculation of coupled-mode theory"*, Journal of the Optical Society of America B, **25**, pp. 1895–1898 (2008).

[18] M. L. Gorodetsky and V. S. Ilchenko. *"Optical microsphere resonators: optimal coupling to high-Q whispering-gallery modes"*, Journal of the Optical Society of America B, **16**, pp. 147–154 (1999).

[19] Y. Dumeige, S. Trebaol, L. Ghişa, T. K. N. Nguyên, H. Tavernier, and P. Féron. *"Determination of coupling regime of high-Q resonators and optical gain of highly selective amplifiers"*, Journal of the Optical Society of America B, **25**, pp. 2073–2080 (2008).

[20] C. Balanis. *"Advanced engineering electromagnetics"*, 2nd edition, John Wiley & Sons, Hoboken, N.J (2012).

[21] A. W. Poon, R. K. Chang, and J. A. Lock. *"Spiral morphology-dependent resonances in an optical fiber: effects of fiber tilt and focused Gaussian beam illumination"*, Optics Letters, **23**, pp. 1105–1107 (1998).

3 | Experimental Procedures

In this chapter we will describe the experimental procedures carried out to fabricate and characterize our MRs for WGMs. The fabrication process and characteristics of the microfibers employed for the coupling will be detailed. To illustrate the process, we will characterize the resonances of a cylindrical MR fabricated from a conventional silica fiber, and from a polymer fiber. Thus, we will show that our experimental procedure is valid for a variety of MR materials.

3.1 Experimental setup

Figure 3.1 shows the general experimental setup used in the experiments throughout this work to excite and measure the WGMs. The general setup includes different sections for different purposes: (i) the light source, (ii) the coupling of the light to the MR, and (iii) the characterization of the WGM resonances.

(i) The light source used to monitor the WGMs will depend on the Q-factor of the resonances. When the linewidth is broad (Q lower than 10^5), a broadband source such as a LED can be employed to excite the WGMs. In this case, to characterize the WGM MRs we would employ a common OSA (resolution: 20 pm). In most cases of this work, the WGM resonators exhibit high Q-factors (higher than 10^6), and the resonances can not be measured with a typical OSA.

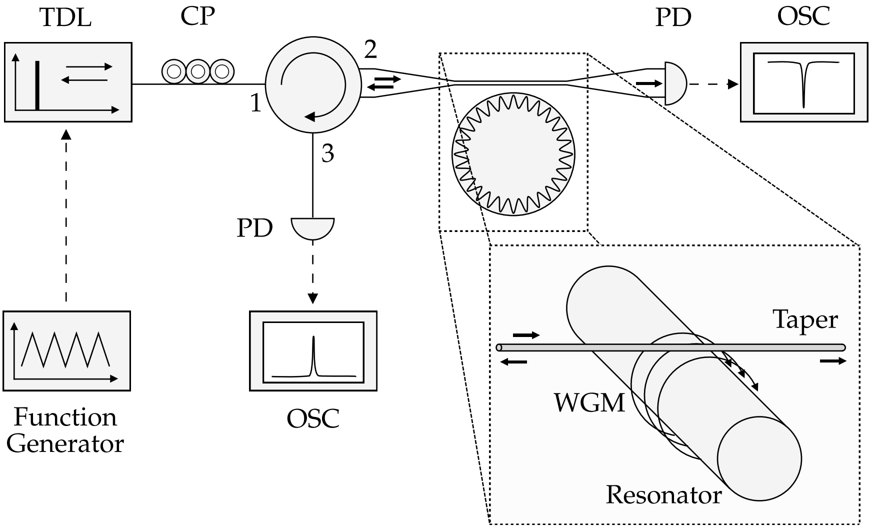

Figure 3.1: Scheme of the general experimental setup for exciting and measuring WGM resonances.

In the cases with Q-factor higher than 10^6, we will use a tunable continuous wave diode laser (TDL), linearly polarized with a narrow linewidth (< 300 kHz) as the light source. The tuning range covers typically from 1515 to $1545\,\mathrm{nm}$. The laser integrates a piezoelectric-based fine frequency tuning facility that allows continuous scanning of the emitted signal around a given wavelength. The sweeping of the laser is controlled by a triangle wave signal from a function generator. The sweeping velocity can be controlled by means of the parameters of the electric signal that drives the laser. A polarization controller (PC) is placed after the laser to rotate the polarization light, which allows the excitation of TM- and TE-WGMs separately. An optical circulator enables measuring the WGM resonances in reflection.

(ii) In order to couple the light to the resonator, the optical signal is launched through a $2\,\mu\mathrm{m}$ diameter auxiliary tapered fiber which is placed perpendicularly on a 3-axis flexure stage allowing to control the distance between them to optimize the coupling. The resonator consists on a section of a bare optical fiber.

(iii) The transmitted and reflected light from the taper is measured by means of two photodetectors (PDs), whose output signal is registered by the digital oscilloscopes (OSCs) synchronized with the electrical signal driving the laser. The transmission and reflection trace obtained as a function of time are converted into spectra (this is, intensity vs wavelength) using a previous calibration of the sweeping velocity of the TDL.

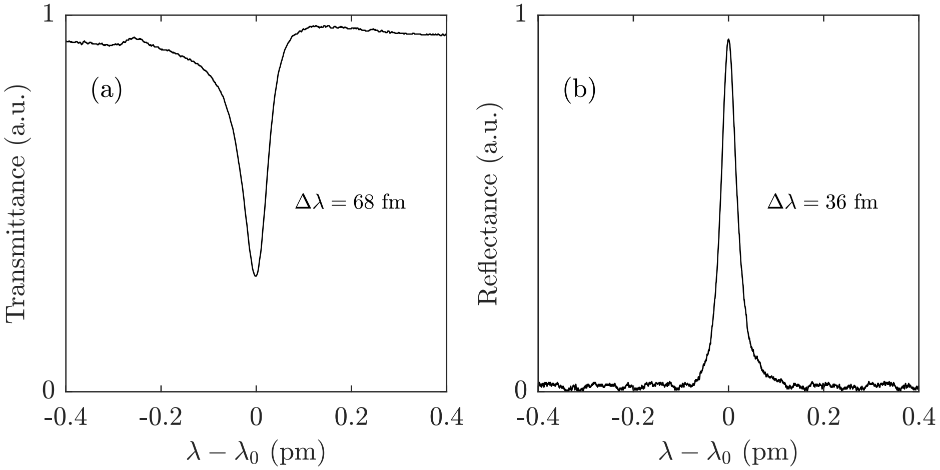

Figure 3.2: WGM spectra in a cylindrical, silica MR ($a = 62\,\mu\text{m}$): (a) Transmitted signal; (b) Reflected signal.

Figure 3.2 shows the transmission and reflection spectra of a WGM resonance in a slightly stretched conventional optical fiber ($a = 62\,\mu\text{m}$). The Q-factor of the WGM resonance is $\sim 4 \cdot 10^7$. The linewidth of the transmittance spectrum is 68 fm, while for the reflectance spectrum is 36 fm. The linewidth difference is due to different reasons. When the transmitted spectrum presents an asymmetry at shorter wavelengths, and the reflected spectrum is symmetric, as the situation presented in Fig. 3.2, this asymmetry is due to the existence of spiral modes (see Chapter 2). These modes can be excited because the cylindrical MR does not confine the light in the axial direction, and the illumination source provided by the taper is not a plane wave but a beam of finite extension. Thus, modes with $\beta_z \neq 0$ and $\beta_z \ll \beta_\phi$ can be excited. In addition, the existence of inhomogeneities on the surface of the resonator leads to an internal modal coupling between the two counter-propagating WGMs, and the splitting of the resonant wavelength in a doublet. All these reasons lead to a broadening of the resonances [1]. Moreover, for resonators with small half-angles (this is, conical shape), it can be observed the existence of an asymmetry towards longer wavelengths [2]. Nevertheless, the evanescent field of a tapered fiber, which is a finite beam with a gaussian spatial distribution, can be modeled as a weighted sum of monochromatic plane waves traveling in different directions (angular spectrum) [1]. Then, it is important to point out that the WGMs theoretical approach presented in Chapter 2 is also valid when we consider the coupling by means of a taper. Besides, it has been demonstrated that such a beam can excite WGM resonances with high Q-factors in cylindrical MRs [3].

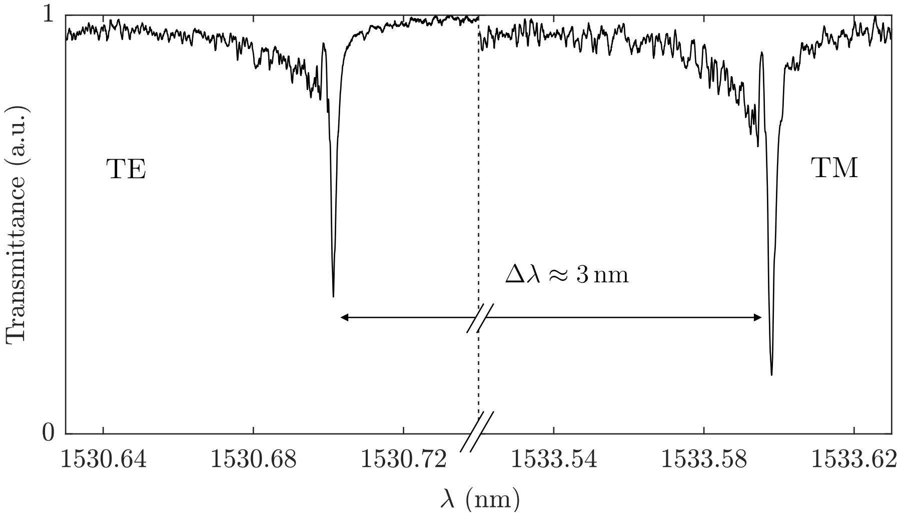

Figure 3.3: WGM resonances with the same m order for TE and TM polarization.

Figure 3.3 shows an example of a resonance for the TE and the TM polarization in a slightly stretched optical fiber ($a = 62$ µm) and the same azimuthal order. As it can be observed, the resonant wavelengths are not usually degenerated, and they are separated $\Delta\lambda \approx 3\,\mathrm{nm}$ with our setup. To identify which resonance corresponds to each polarization, it is necessary to solve the characteristic equations of the WGMs, Eqs. (2.17), for our MR experimentally characterized. By comparing the theoretical results with the experimental measurements, we can determine the azimuthal order and the polarization state of each resonance.

To conclude, let us point out the case of resonators with ultra-high Q-factors. In this case the measurement setup typically employed is slightly different from the one described in Fig. 3.1. Although the characterization can be done with a narrowband tunable laser with high level of frequency stability, the ring-down technique is preferred [4]. The use of this technique allows to avoid some limitations such as thermal drifts of the spectral position and the undesired contribution of nonlinear effects. This technique is employed with MRs with spherical and toroidal shapes, since they generally provide higher Q-factors than cylindrical shaped MRs.

3.2 Tapers fabrication technique

Although there exists different techniques for coupling energy to a resonator (by using a prism, an integrated waveguide, a fiber tip, etc) in this work we will excite the WGMs by employing a tapered fiber (a microfiber). We will use this method because the efficiency of the coupling can be as high as 99.97% for a fused silica resonator [5].

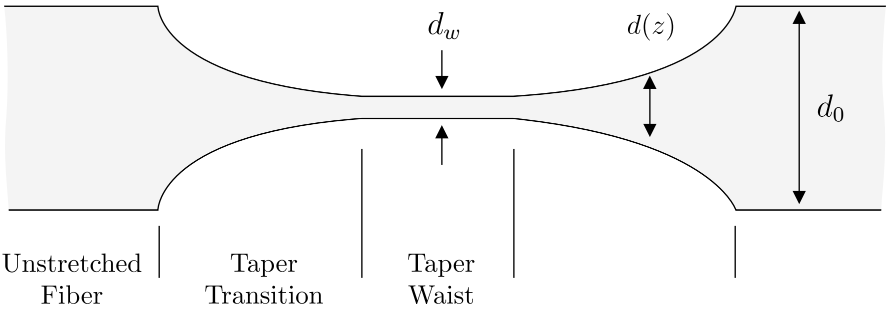

Figure 3.4: Scheme of the structure of a tapered optical fiber. The three distinguished sections are shown.

The operating principle of the coupling consists on decreasing the diameter of an optical fiber until the evanescent field of its propagating modes is large enough to couple energy to the MR. To fabricate the microfibers, we employ a fuse-and-pull technique from conventional telecom fibers [6]. From a theoretical point of view, the technique is based on the mass conservation of a silica rod (this is, the fiber), as it is fused and stretched. The result is a fiber with a section of reduced diameter with two transitions. By means of an accurate control of the fabrication process, it is possible to control the final diameter of the waist, and the length and shape of the transitions [7]. Figure 3.4 shows the schematic structure of a fiber taper. The different sections can be identified: the unstretched fiber with diameter d_0 (for a bare conventional fiber $d_0 = 125\,\mu\text{m}$), the taper waist with diameter d_w, and the taper transition with a shape dependent on the fabrication conditions. In our case, they will show an exponential shape.

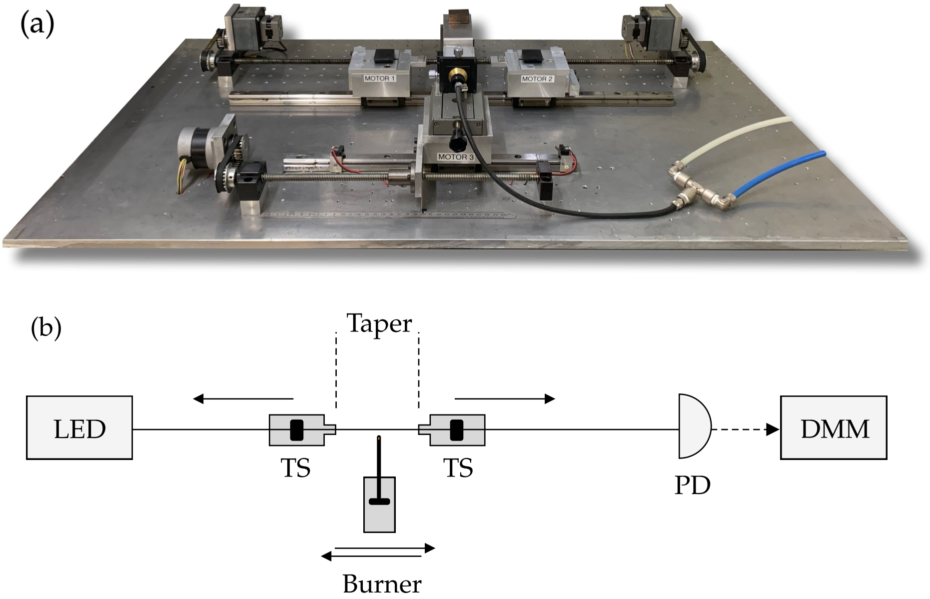

Figure 3.5: (a) Setup of the fuse-and-pull microfiber machine. (b) Scheme of the tapers fabrication and the losses monitoring.

For the fabrication, we employ a fuse-and-pull machine developed in the Laboratory of Fiber Optics of the University of Valencia. Figure 3.5a shows an image of the system and the different elements of the mechanism. Figure 3.5b shows a schematic representation of the experimental setup and the equipment employed to monitor the transmittance of the taper. The translation stages (TSs) stretch the fiber as the burner sweeps the tapered section in a back-and-forth motion. During all the process, the transmittance of a light source is monitored to ensure that fabrication losses are kept, typically, under 0.5 dB, as a maximum, for our tapers. The use of this system ensures both high repeatability and high manufacturing precision.

The typical parameters of the tapers employed to excite the WGM resonances are: diameter of the waist $d_w = 2$ µm, length of the waist ~ 6 mm.

Besides, in order to improve the Q-factor of the WGM MRs, we also process the fibers that will be used as the MRs, by tapering them slightly down to ~ 124 µm in diameter. When the coating of a conventional fiber is removed, imperfections in the surface of the fiber can appear. As it was previously mentioned, see Chapter 2, the roughness introduces scattering losses. The tapering process smoothes the surface of the optical fiber, leading to an increment of the Q-factor.

3.3 WGM resonances in a polymeric resonator

Although the most employed material for the fabrication of WGM resonators is SiO_2, depending on the geometry and the application of the resonator, the implementation of different materials and fabrication techniques could be needed. One type of these materials that are currently under study are polymers. We will show some experimental results with such resonators in the following chapters. To excite and measure the WGM resonances of a cylindrical-shaped polymeric resonator, the technique showed in the previous section can be employed. The inset of Fig. 3.6 shows a micrograph of a polymeric hollow resonator. The description of the polymer material and the fabrication method (based on the two-photon polymerization) can be found in [8]. The resonator exhibits a diameter of $55\,\mu\mathrm{m}$, a wall thickness of $3.9\,\mu\mathrm{m}$, and a height of $60\,\mu\mathrm{m}$. Figure 3.6 shows the transmittance spectrum of one of its resonances. The linewidth is $\Delta\lambda \approx 15\,\mathrm{pm}$, which corresponds to a quality factor of $Q = 2.5 \cdot 10^6$. As it can be observed, the resonator presents a high Q-factor. This is possible due to the low absorption of the polymer at $1550\,\mathrm{nm}$, the small roughness of the surface wall ($1.5\,\mathrm{nm}$), and the polymer refractive index (1.510 ± 0.001), similar to the silica, which enables an efficient coupling by employing a silica tapered fiber. It can also be seen that the resonance exhibit an asymmetry at longer wavelengths. This is a clear example of the asymmetry induced by a conical shape that we commented in the previous section.

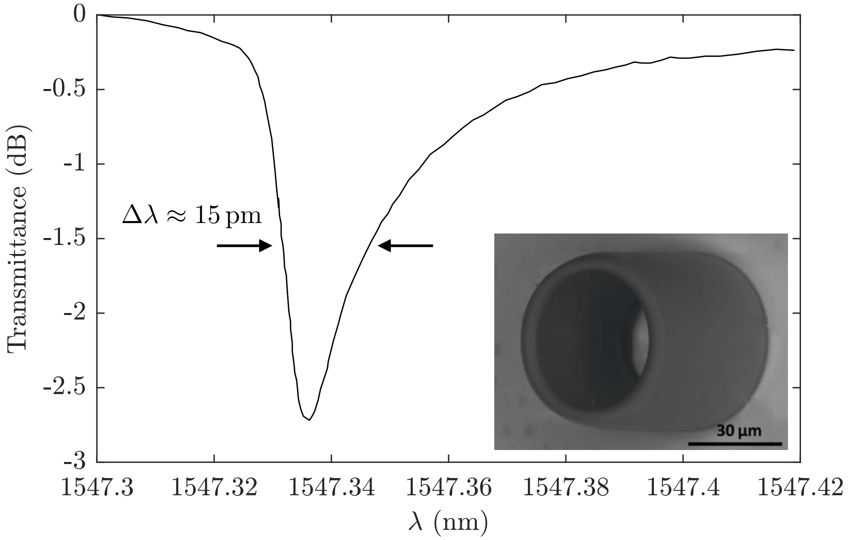

Figure 3.6: Cylindrical hollow polymer MRs. Transmittance spectrum of a WGM resonance excited in the polymer MR. Inset: Micrograph of a typical MR produced by two-photon polimerization.

References

[1] V. Zamora, A. Díez, M. V. Andrés, and B. Gimeno. *"Interrogation of whispering-gallery modes resonances in cylindrical microcavities by backreflection detection"*, Optics Letters, **34**, pp. 1039–1041 (2009).

[2] M. Sumetsky. *"Localization of light on a cone: theoretical evidence and experimental demonstration for an optical fiber"*, Optics Letters, **36**, pp. 145–147 (2011).

[3] M. Sumetsky. *"Mode localization and the Q-factor of a cylindrical microresonator"*, Optics Letters, **35**, pp. 2385–2387 (2010).

[4] A. A. Savchenkov, A. B. Matsko, V. S. Ilchenko, and L. Maleki. *"Optical resonators with ten million finesse"*, Optics Express, **15**, pp. 6768–6773 (2007).

[5] S. Spillane, T. Kippenberg, O. Painter, and K. Vahala. *"Ideality in a Fiber-Taper-Coupled Microresonator System for Application to Cavity Quantum Electrodynamics"*, Physical Review Letters, **91**, p. 043902 (2003).

[6] R. P. Kenny, T. A. Birks, and K. P. Oakley. *"Control of optical fibre taper shape"*, Electronics Letters, **27**, pp. 1654–1656 (1991).

[7] T. A. Birks and Y. W. Li. *"The shape of fiber tapers"*, Journal of Lightwave Technology, **10**, pp. 432–438 (1992).

[8] N. B. Tomazio, A. J. G. Otuka, G. F. B. Almeida, X. Roselló-Mechó, M. V. Andrés, and C. R. Mendonça. *"Femtosecond laser fabrication of high-Q whispering gallery mode microresonators via two-photon polymerization"*, Journal of Polymer Science Part B: Polymer Physics, **55**, pp. 569–574 (2017).

4 Strain-Optic Effect

In this chapter we will characterize the strain-optic effect in cylindrical, isotropic resonators by using WGMs. We will present a theoretical description of the modification of the material optical properties due to an axial stretching of the MR. The variation of the permittivity tensor, together with the variation of the mechanical parameters of the resonator, are derived. While in silica MRs, the axial strain will induce an anisotropic permittivity, PMMA MRs will be isotropic even under axial stretching, due to the particular values of the strain-optic coefficients in this material. We will perform an experimental characterization of the spectral properties of WGM resonances in both materials, to illustrate this different behavior. In addition, this technique, will allow us to measure the strain-optic coefficients.

4.1 Theoretical description

The strain-optic effect describes the changes in the optical properties of a material due to mechanical strain. Traditionally, this effect is expressed in terms of variations of the relative dielectric impermeability tensor (which is the inverse of the permittivity tensor), $\bar{\boldsymbol{\eta}}$, induced by strain, $\bar{\boldsymbol{S}}$ [1]. The effect can also be expressed in terms of the stress, $\bar{\boldsymbol{T}}$, since it is linearly related with the strain by means of Hooke's law (in this work, we will only consider linear elastic materials).

$$\eta_{ij}\left(\bar{\boldsymbol{S}}\right) = \eta_{ij}^{(0)} + \Delta\eta_{ij}\left(\bar{\boldsymbol{S}}\right) = \eta_{ij}^{(0)} + \sum_{k,l} p_{ijkl} S_{kl} \tag{4.1}$$

where $\eta_{ij}^{(0)}$ is the impermeability tensor of the unperturbed material, and p_{ijkl} is the strain-optic coefficients tensor. In general, a fourth-rank tensor, has 81 independent elements. However, due to the strain tensor symmetry ($S_{kl} = S_{lk}$) [2], and the impermeability tensor symmetry ($\eta_{ij} = \eta_{ji}$) [3], the number of elements is reduced to 36, and this allows using a contracted index notation to avoid the double indices, this is, $p_{ijkl} = p_{mn}$ where $m, n = 1, 2, ...6$. With this notation, Eq. (4.1) can be reduced to:

$$\eta_{m}\left(\bar{\boldsymbol{S}}\right) = \eta_{m}^{(0)} + \Delta\eta_{m}\left(\bar{\boldsymbol{S}}\right) = \eta_{m}^{(0)} + \sum_{n} p_{mn} S_{n} \tag{4.2}$$

The strain-optic coefficients are dimensionless, and the number of independent components depends on the structure of the material medium. For isotropic materials, which is the case of interest for this work, the number of independent components are reduced to two, and we can write the strain-optic tensor in contracted notation as [1]:

$$p_{ij} = \begin{pmatrix} p_{11} & p_{12} & p_{12} & & & \\ p_{12} & p_{11} & p_{12} & & & \\ p_{12} & p_{12} & p_{11} & & & \\ & & & p_{44} & & \\ & & & & p_{44} & \\ & & & & & p_{44} \end{pmatrix} \tag{4.3}$$

where $p_{44} = \frac{1}{2}\left(p_{11} - p_{12}\right)$. Once we have described the expression of the strain-optic tensor, it is necessary to establish the form of the strain tensor (the way the mechanical strain is applied to the material) in order to obtain the variation of the dielectric permittivity. For the purposes of this work, we will study the deformation that suffers a cylindrical MR (a rod) under axial stretch.

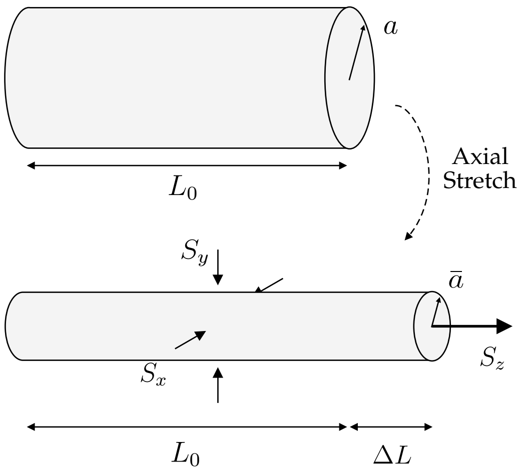

Figure 4.1: Scheme of the deformations suffered by a cylindrical shaped resonator under axial stretch.

Figure 4.1 shows a schematic representation of the effects of an axial stretch applied to a rod. When there is not an applied strain, the unperturbed cylinder has a length L_0 and radius a. When an axial deformation is considered, the length of the rod experiences an elongation ΔL, together with a shrinking of the radius Δa. The axial deformation, S_z, is given by the ratio of the unperturbed length to the elongation: $S_z = \Delta L/L_0$. When a material suffers a stretching, the elongation in one direction is accompanied by contractions in the two transversal directions. The ratio between these deformations is given by the Poisson's ratio, $\nu = -S_x/S_z = -S_y/S_z$.

By taking into account the different deformations and the strain-optic tensor, we calculate the variation of the impermeability of a rod under axial stretch:

$$\begin{pmatrix} \Delta\eta_x \\ \Delta\eta_y \\ \Delta\eta_z \\ \Delta\eta_{xy} \\ \Delta\eta_{yz} \\ \Delta\eta_{zy} \end{pmatrix} = \begin{pmatrix} p_{11} & p_{12} & p_{12} & & & \\ p_{12} & p_{11} & p_{12} & & & \\ p_{12} & p_{12} & p_{11} & & & \\ & & & p_{44} & & \\ & & & & p_{44} & \\ & & & & & p_{44} \end{pmatrix} \cdot \begin{pmatrix} -\nu S_z \\ -\nu S_z \\ S_z \\ 0 \\ 0 \\ 0 \end{pmatrix} \tag{4.4}$$

where S_x and S_y are expressed in terms of S_z. By solving the Eq. (4.4), we obtain the variation introduced in the different components of the permittivity tensor, as a function of the axial strain. As it can be noticed, the variation in the transversal components x and y are the same. Therefore, from this moment, we consider that $\Delta\eta_t \equiv \Delta\eta_x = \Delta\eta_y$.

$$\begin{aligned}
\Delta\eta_t &= \left[-\nu p_{11} + (1-\nu)p_{12}\right] S_z \\
\Delta\eta_z &= \left[p_{11} - 2\nu p_{12}\right] S_z \\
\Delta\eta_{xy} &= \Delta\eta_{yz} = \Delta\eta_{zy} = 0
\end{aligned} \tag{4.5}$$

If we consider the variation of the impermeability tensor, Eqs. (4.5), in the general expression of the dielectric impermeability, Eq. (4.1), and assume that the strain-optic coefficients are very small, we can derive the variation in the refractive index:

$$\begin{aligned}
\frac{\Delta n_t}{n_1} &\approx -\frac{n_1^2}{2}\left[-\nu p_{11} + (1-\nu)p_{12}\right] S_z \equiv -p_{et} S_z \\
\frac{\Delta n_z}{n_1} &\approx -\frac{n_1^2}{2}\left[p_{11} - 2\nu p_{12}\right] S_z \equiv -p_{ez} S_z \\
\Delta n_{xy} &= \Delta n_{yz} = \Delta n_{zy} = 0
\end{aligned} \tag{4.6}$$

where p_{et} and p_{ez} are effective strain-optic coefficients defined for simplicity. It can be noticed that the variation in the refractive index is different for the transversal and axial components. Thus, when the strain-optic coefficients p_{11} and p_{12} are different, an axial stretch in an isotropic cylinder induces an uniaxial anisotropy in the medium. For example, for fused silica, if we estimate the anisotropy with the reported values of $p_{11} = 0.121$, $p_{12} = 0.270$ [4], and $\nu = 0.17$ [5], the ratio is $\Delta n_t/\Delta n_z \approx 6.97$, so a significant anisotropy is expected. It should be noticed out that, until this moment, we have described the strain-optic effect in cartesian coordinates, while the problem of the WGMs is described in a cylindrical coordinate system. If we perform a coordinate system transformation of the permittivity tensor into cylindrical coordinates, the same expression is obtained. Thus, Eqs. (4.6) for Δn_t and Δn_z are valid for both coordinate systems, cartesian and cylindrical.

To study how an axial stretch affects the spectral position of the WGM resonances in a cylindrical dielectric resonator, the characteristic equations for an uniaxial medium described in Chapter 2, Eqs. (2.17), must be solved. The changes in the optical properties are given by the anisotropic variation of the permittivity tensor, Eqs. (4.6). On the other hand, the changes in the mechanical properties of the resonator are determined by the axial strain, $S_z = \Delta L / L_0$, and the variation of the radius and Poisson's ratio, ν:

$$\Delta a = -a\nu S_z = -a\nu \frac{\Delta L}{L_0} \tag{4.7}$$

By taking into account the resonant condition for a WGM, $m\lambda_R = 2\pi n_{\text{eff}}$, and carrying out a perturbative approach as a function of the axial strain, we obtain the relative shift of the WGM resonances:

$$\frac{\Delta\lambda_R}{\lambda_R} = \left(\frac{1}{a}\frac{da}{dS_z} + \frac{1}{n_{\text{eff}}}\frac{dn_{\text{eff}}}{dS_z}\right)\Delta S_z \tag{4.8}$$

As a first approximation, the effective refractive index of the modes can be assumed to be that of the material refractive index. It must be taken into account that the TM polarization depends on the axial component of the refractive index, Δn_z, while the TE polarization depends on the transversal component, Δn_t. Thus, since $\Delta n_t / \Delta n_z \approx 6.97$, we obtain that, for a fused silica MR, the relative shift between the TE-WGM and the TM-WGM resonances is $\Delta\lambda^{\text{TE}} / \Delta\lambda^{\text{TM}} \sim 1.66$. In practice, this will imply that TE modes shift faster than the TM as the strain is increased.

We introduce the strain as a perturbation in the characteristic equations of the WGMs, Eqs. (2.17); as a result, we can write the first-order approximation for the relative shift of the resonances:

$$\left[\frac{\Delta\lambda_R}{\lambda_R}\right]_{\text{TE,TM}} = \frac{\Delta a}{a} + (1 - C_{\text{TE,TM}})\frac{\Delta n_{t,z}}{n_0} \tag{4.9}$$

where $C_{\text{TE,TM}}$ is a small coefficient that depends on wavelength, radius and material refractive index. The coefficient is different for each polarization state and it can be determined for the particular experimental parameters. Then, by measuring the shift of both polarizations as a function of the strain, we can obtain the strain-optic coefficients just by solving a linear system of equations.

$$s_{\text{TE,TM}} = -\nu - (1 - C_{\text{TE,TM}})p_{et,ez} \tag{4.10}$$

where s_{TE} and s_{TM} are the slopes of the WGM resonances relative shift with the axial strain, for each polarization.

Eq. (4.9) introduces a correction of the order of 4% to the rough estimation that is obtained when the effective index of the modes is approximated to the material refractive index (this is, $C_{\text{TE,TM}} = 0$) in Eq. (4.8). Therefore, in order to obtain the most accurate values to evaluate the strain-optic effect, we will use Eq. (4.10) to calculate p_{11} and p_{12}.

4.2 Experimental characterization

To study the effects of an axial stretching in a resonator, we carried out a characterization of the spectral position of the WGM resonances as a function of the strain applied to the MR. To do the measurements, we performed a small modification to the general experimental arrangement depicted in Fig. 3.1. For these experiments, a controllable axial strain is applied to the MR by means of a calibrated translation stage with a step of 0.5 µm, see Fig. 4.2.

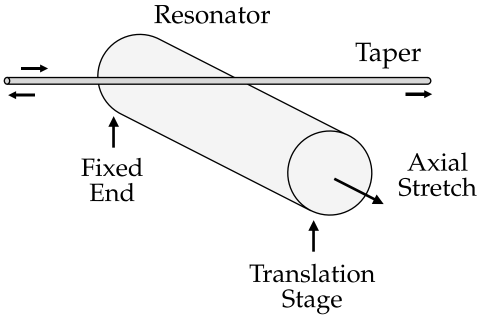

Figure 4.2: Scheme of the experimental arrangement with translation stage to axially stretch the resonator.

The technique relies on measuring the shift of the WGM resonances as a function of the axial strain. One crucial characteristic, which was predicted by the simulations, is that the relative shift of the resonances as a function of the strain is virtually independent of the azimuthal and radial orders, within a deviation smaller than 0.01%. This feature enables the use of WGM resonances to characterize the strain-optic effect, since it does not matter which specific resonance is employed for measuring.

Furthermore, as it has been shown in Chapter 3, the technique employed to excite and measure the WGMs allows the characterization of silica MRs, but also of resonators fabricated with other materials with refractive indices similar to that of the taper material. This property allows to study the strain-optic effect in different materials. In this work, we will carry out the characterization of silica and PMMA MRs under axial strain.

(I). Silica microresonators

We measured the shift of the WGM resonances of a silica MR as a function of the axial strain. Our resonator was a conventional bare SMF-28 fiber without coating, with a diameter reduced to $124\,\mu\text{m}$. The tapered fiber used to couple the light has the typical parameters of the microfibers employed in this work: $2\,\mu\text{m}$ waist and

6 mm length. The linewidth of the studied resonances was $\sim 0.22\,\mathrm{pm}$ typically, which corresponds to a Q-factor of $\sim 7 \cdot 10^6$.

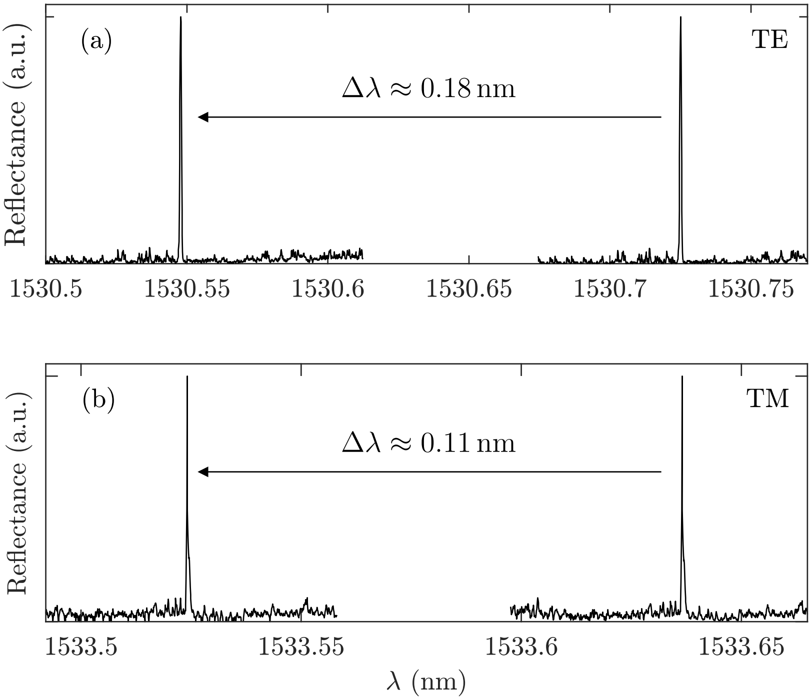

Figure 4.3: Example of the wavelength shift measured for a strain of $S_z = 330\,\mu\epsilon$. (a) TE polarization: (b) TM polarization.

Figure 4.3 gives an illustrative example of the wavelength shift measured for a resonance of each polarization, for a given strain of $330\,\mu\epsilon$. The TE and TM polarizations can be identified because of their different response with the strain, in accordance with the theory. The TE-WGM resonance shifts $180\,\mathrm{pm}$ towards shorter wavelengths, while the TM-WGM resonance shifts $110\,\mathrm{pm}$. As it can be observed, the TE polarization shifts around ~ 1.6 times more than the TM polarization, as it is predicted from the simulations. Although this effect has been extensively exploited in different applications, such as strain sensors [6] or strain-induced long-period gratings [7], the anisotropic behavior of the material is rarely mentioned [8]. The tuning of WGM resonances by means of an axial stretch in silica resonators has been reported in the past [9], but the different response of the TE and TM polarizations had not been mentioned before this work, up to our knowledge.

The strain-optic coefficients of an optical fiber are usually determined by measuring the optical activity induced by a mechanical twist and the phase change caused by longitudinal strain [10, 11]. This technique relies on the study of the conventional axial modes propagating through the fiber. Since the electromagnetic field of the modes is mainly transverse to the axis of the fiber [12], the anisotropy does not show up. On the contrary, WGMs have a significant longitudinal components, and their electromagnetic field experiences the anisotropy of the strain-optic effect intrinsically, since longitudinal and transversal components are dependent on different values of the refractive index. In the past few years, an increasing number of fiber devices in which the longitudinal component of the electromagnetic field is not negligible have appeared, such as microfibers [13], and microstructured optical fibers with a high air filling fraction [14]. For these cases, the measurement and characterization of the anisotropy of the strain-optic effect is of high interest.

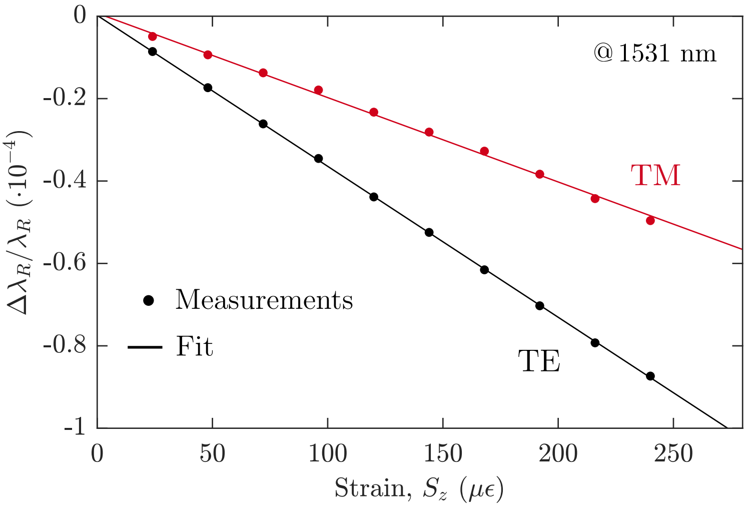

Figure 4.4: Relative wavelength shift of WGM resonances as a function of the strain for the TE and TM polarization, at 1531 nm.

Figure 4.4 shows the relative wavelength shift as a function of the strain for a resonance centered at $1531\,\mathrm{nm}$. The slopes of the linear regressions that fit the experimental values are: $s_{\mathrm{TE}} = -0.369 \pm 0.006\,\mathrm{p}\epsilon^{-1}$ and $s_{\mathrm{TM}} = -0.201 \pm 0.004\,\mathrm{p}\epsilon^{-1}$. We calculated the uncertainties in the slopes considering non-correlated errors in both variables [15]. The error in the strain measurements is $\pm 4\,\mu\epsilon$, and the errors in the relative wavelength shift are within the range $(0.6 - 6) \cdot 10^{-6}$, from the smallest to the highest strain values. The anisotropy can be clearly observed from the measurements: $s_{\mathrm{TE}}/s_{\mathrm{TM}} = 1.84$. From the values of the slopes and considering the Eq. (4.10), it is possible to calculate the strain-optic coefficients. For the particular parameters of the experiment, $a = 62\,\mu\mathrm{m}$, $m = 354$ and n_1 calculated using Sellmeier [16], $C_{\mathrm{TE}} = 5.766 \cdot 10^{-3}$ and $C_{\mathrm{TM}} = 3.756 \cdot 10^{-3}$. Thus, by taking into account the Poisson's ratio $\nu = 0.17 \pm 0.01$, the values of the strain-optic coefficients are: $p_{11} = 0.116 \pm 0.017$ and $p_{12} = 0.255 \pm 0.021$.

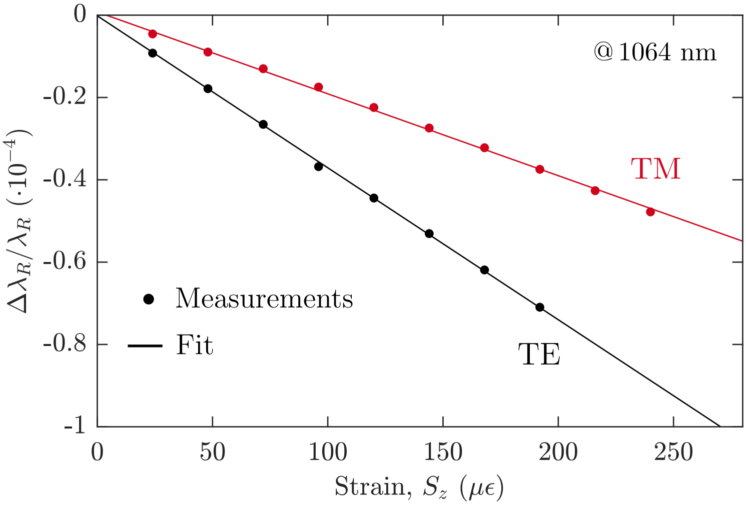

Figure 4.5: Relative wavelength shift of WGM resonances as a function of the strain for the TE and TM polarization, at $1064\,\mathrm{nm}$.

An additional advantage of this technique is that it does not require single-mode propagation in order to characterize the MRs. The method based on the optical activity requires it, since it uses the conventional modes of the fiber. This feature enables the measurement of the strain-optic coefficients at different wavelengths using the same MR for all of them, as long as the material is transparent, to determine their dispersion.

Figure 4.5 shows the relative shift as a function of the strain for a resonance centered at 1064 nm. The characterization is analogous to the previous one. The slopes of the linear regressions are: $s_{\mathrm{TE}} = -0.378 \pm 0.008\,\mathrm{p}\epsilon^{-1}$ and $s_{\mathrm{TM}} = -0.213 \pm 0.004\,\mathrm{p}\epsilon^{-1}$. In this wavelength range, $m = 516$, $C_{\mathrm{TE}} = 3.848 \cdot 10^{-3}$ and $C_{\mathrm{TM}} = 2.505 \cdot 10^{-3}$. From these values and Poisson's ratio, we calculate the values of the strain-optic coefficients at 1064 nm: $p_{11} = 0.132 \pm 0.018$ and $p_{12} = 0.267 \pm 0.024$.

The values of the strain-optic coefficients obtained are comparable to those reported in the literature, which were obtained by other techniques. Table 4.1 summarizes the results for both wavelengths, compared to other measurements reported in the literature. Both sets of values are in good agreement, and the small differences might be due to the fact that the technique based on the WGMs measures the properties of the cladding material (for the fibers characterized, the p_{ij} of fused silica). While, in the other techniques, the value of the coefficients are determined, mainly, by the material of the fiber core, which is usually silica doped with different elements. In the study presented in [10], the core of the fiber is also made of silica. Here the difference may be due to the different cladding material (silica doped with B_2O_3), which affects the conventional optical modes of a fiber because of their evanescent field.

	Present Work		**Literature**
	1531 nm	1064 nm	
p_{11}	0.116	0.131	0.113 @633 nm [10] 0.121 @633 nm [4]
p_{12}	0.255	0.267	0.252 @633 nm [10] 0.270 @633 nm [4]

Table 4.1: Comparison of measured p_{ij} coefficients with the values reported in the literature.

The most critical factor for an accurate determination of the individual strain-optic coefficients is the uncertainty associated to the Poisson's ratio (6% in this case, the highest of all the parameters considered here). Thus, it is useful to evaluate the slope difference, $s_{\mathrm{TM}} - s_{\mathrm{TE}} = 0.168 \pm 0.007\,\mathrm{p}\epsilon^{-1}$, which is defined in the literature as the bending-induced birefringence, p_{eb}, and does not depend on the Poisson's ratio. In addition, the WGMs technique enables the experimental measurement of the effective strain-optic coefficients, p_{et} and p_{ez}. The coefficient p_{et} can be compared with the values reported in the study of fiber Bragg gratings strain sensors. The p_{ez} coefficient can be calculated by considering the coefficients p_{11}, p_{12} and ν. Our measurements of the effective strain-optic coefficients, and those reported in the literature are compiled in Tab. 4.2. From these comparisons, we can conclude that the results obtained by our technique are in good agreement with the previously reported values.

	Present Work		Literature
	1531 nm	1064 nm	
p_{et}	0.200	0.209	0.205 @ 633 nm [10] 0.205 @ 1530 nm [17] 0.202 @ 1534 nm [18]
p_{ez}	0.031	0.043	0.030$^{(a)}$ [4, 5] 0.034 @ 633 nm [10]
p_{eb}	0.168	0.165	0.186 @ 633 nm [19] 0.171$^{(b)}$ @ 1550 nm [20]

(a) Calculated using the p_{ij} and ν values of bulk silica.

(b) Calculated using the strain-optic rotation coefficient g: $p_{eb} = (1 + \nu)g$.

Table 4.2: Comparison of measured effective strain-optic coeffients with those reported in the literature.

When comparing the values of the strain-optic coefficients at different wavelengths, it is difficult to extract conclusive information on wavelength dispersion due to its relatively high errors. As it was explained, the major contribution to the error is the uncertainty of the Poisson's ratio. Therefore, by evaluating the relative dispersion of the strain-optic coefficient $p_{44} = (p_{11} - p_{12})/2$, i.e., $(dp_{44}/d\lambda)/p_{44}$, we can calculate a value with relative precision. This is possible since Poisson's ratio is not necessary for this calculation, and the refractive index is known with high precision. We obtain a relative wavelength dispersion for p_{44} of 5% µm^{-1}, which is comparable to the 8% µm^{-1} reported in [10] (it is worth to point out that this result was obtained from two measurements at 633 and 880 nm which are wavelengths different to ours). In both cases, the estimated wavelength dispersion is within the experimental error. From our results, and those reported in the literature, we can conclude that the strain-optic coefficients of the fused silica show a flat dispersion response.

(II). PMMA microresonators

We also used PMMA fibers as MRs for WGMs. We used the same procedure to measure the shift of its WGM resonances as a function of the axial strain. The resonator is a PMMA rod with a diameter of 130 µm. It is worth to point out that, for the case of PMMA fibers, the smoothness of the surface is not as high as in the case of the silica, and the absorption coefficient is also higher than that of the silica. Thus, the linewidth of the resonances is broader: in particular the linewidth of our PMMA WGM resonances are typically $\sim 60\,\mathrm{pm}$, which corresponds to a Q-factor of $\sim 2.6 \cdot 10^4$. The linewidth of the resonances requires to employ a broadband source and an OSA to excite and measure the WGMs. The tapered silica fiber used to couple the light has 2 µm waist and $6\,\mathrm{mm}$ length, as usual.

Figure 4.6 shows the relative shift as a function of the strain for a resonance centered at $1550\,\mathrm{nm}$. The slopes of the linear regressions are: $s_1 = -0.439 \pm$

$0.005\,\mathrm{p\epsilon}^{-1}$ and $s_2 = -0.440 \pm 0.004\,\mathrm{p\epsilon}^{-1}$. As it can be observed, the shift of both polarizations is the same, since the difference is within the experimental error. For the particular parameters of the resonator, $a = 65\,\mu\mathrm{m}$, $m = 378$ and n_1 of the PMMA calculated from [21], $C_{\mathrm{TE}} = 3.115 \cdot 10^{-3}$ and $C_{\mathrm{TM}} = 4.853 \cdot 10^{-3}$. Thus, by taking into account the Poisson's ratio $\nu = 0.340 \pm 0.005$ [22], the values of the strain-optic coefficients are: $p_{11} = 0.283 \pm 0.021$ and $p_{12} = 0.282 \pm 0.024$. The values obtained for the strain-optic coefficients of PMMA are practically identical. Therefore, a resonator under axial strain maintains its isotropic optical response, contrary to the behavior observed in silica.

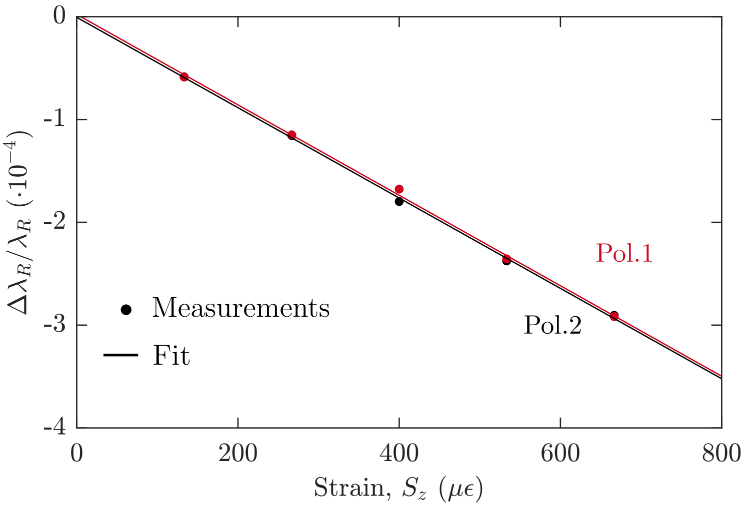

Figure 4.6: Relative wavelength shift of WGM resonances as a function of the strain for a PMMA resonator, at 1550 nm.

Since the experimental technique allows the characterization at different wavelengths, we repeated the measurements of the WGMs shift within a range of $1.2\,\mu\mathrm{m}$, from 800 to 2000 nm (this is the range at which we had available LED sources).

Figure 4.7 shows the values of the p_{ij} coefficients calculated for different wavelengths. As it can be seen, in the whole wavelength range the values are similar within the error, and a flat dispersion curve is observed. Moreover, the coefficients obtained are in good agreement to those reported in the literature [23]. This result is of interest since in many applications of strain sensors in the infrared range based on PMMA fibers, the strain-optic coefficients employed to characterize the optical device are the ones reported for 633 nm ($p_{11} = 0.300$ and $p_{12} = 0.297$). As the results depicted in Fig. 4.7 show, this assumption is valid within the range studied.

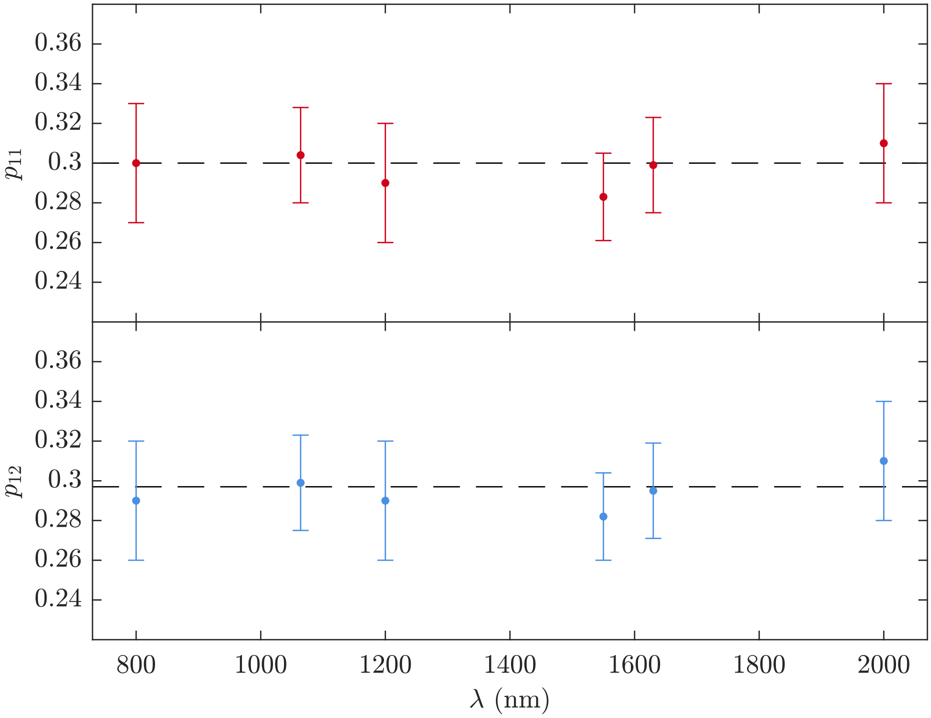

Figure 4.7: Strain-optic coefficients of PMMA at different wavelengths. The dashed lines refer to tabulated values at 633 nm.

References

[1] J.-m. Liu. *"Photonic Devices"*, Cambridge University Press (2005).

[2] M. Sadd. *"Elasticity: theory, applications, and numerics"*, Elsevier/Academic Press, Amsterdam Boston (2014).

[3] S. Visnovsky. *"Optics in magnetic multilayers and nanostructures"*, CRC Taylor & Francis, Boca Raton (2006).

[4] D. R. Lide. *"CRC Handbook of Chemistry and Physics"*, 84 edition, CRC Press (2003).

[5] J. F. Shackelford and W. Alexander. *"CRC Materials Science and Engineering Handbook"*, 3 edition, CRC Press (2001).

[6] A. D. Kersey, M. A. Davis, H. J. Patrick, M. LeBlanc, K. P. Koo, C. G. Askins, M. A. Putnam, and E. J. Friebele. *"Fiber grating sensors"*, Journal of Lightwave Technology, **15**, pp. 1442–1463 (1997).

[7] S. Savin, M. J. F. Digonnet, G. S. Kino, and H. J. Shaw. *"Tunable mechanically induced long-period fiber gratings"*, Optics Letters, **25**, pp. 710–712 (2000).

[8] A. L. Huston and J. D. Eversole. *"Strain-sensitive elastic scattering from cylinders"*, Optics Letters, **18**, pp. 1104–1106 (1993).

[9] M. Pöllinger, D. O'Shea, F. Warken, and A. Rauschenbeutel. *"Ultrahigh-Q Tunable Whispering-Gallery-Mode Microresonator"*, Physical Review Letters, **103**, p. 053901 (2009).

[10] A. Bertholds and R. Dandliker. *"Determination of the individual strain-optic coefficients in single-mode optical fibres"*, Journal of Lightwave Technology, **6**, pp. 17–20 (1988).

[11] P. D. Dragic, J. Ballato, S. Morris, and T. Hawkins. *"Pockels’ coefficients of alumina in aluminosilicate optical fiber"*, Journal of the Optical Society of America B, **30**, pp. 244–250 (2013).

[12] A. Bertholds and R. Dandliker. *"Deformation of single-mode optical fibers under static longitudinal stress"*, Journal of Lightwave Technology, **5**, pp. 895–900 (1987).

[13] S. Skelton, M. Sergides, R. Patel, E. Karczewska, O. Maragó, and P. Jones. *"Evanescent wave optical trapping and transport of micro- and nanoparticles on tapered optical fibers"*, Journal of Quantitative Spectroscopy & Radiative Transfer, **113**, pp. 2512–2520 (2012).

[14] J. Lægsgaard. *"Theory of surface second-harmonic generation in silica nanowires"*, Journal of the Optical Society of America B, **27**, pp. 1317–1324 (2010).

[15] D. York, N. M. Evensen, M. L. Martínez, and J. De Basabe Delgado. *"Unified equations for the slope, intercept, and standard errors of the best straight line"*, American Journal of Physics, **72**, pp. 367–375 (2004).

[16] M. Adams. *"An introduction to optical waveguides"*, Wiley, Chichester New York (1981).

[17] F. Jülich, L. Aulbach, A. Wilfert, P. Kratzer, R. Kuttler, and J. Roths. *"Gauge factors of fibre Bragg grating strain sensors in different types of optical fibres"*, Measurement Science and Technology, **24**, p. 094007 (2013).

[18] P.-C. Law, A. Croteau, and P. D. Dragic. *"Acoustic coefficients of P_2O_5-doped silica fiber: the strain-optic and strain-acoustic coefficients"*, Optical Materials Express, **2**, pp. 391–404 (2012).

[19] R. Ulrich, S. C. Rashleigh, and W. Eickhoff. *"Bending-induced birefringence in single-mode fibers"*, Optics Letters, **5**, pp. 273–275 (1980).

[20] A. Galtarossa, D. Grosso, and L. Palmieri. *"Accurate Characterization of Twist-Induced Optical Activity in Single-Mode Fibers by Means of Polarization-Sensitive Reflectometry"*, IEEE Photonics Technology Letters, **21**, pp. 1713–1715 (2009).

[21] G. Beadie, M. Brindza, R. A. Flynn, A. Rosenberg, and J. S. Shirk. *"Refractive index measurements of poly(methyl methacrylate) (PMMA) from 0.4-1.6 μm"*, Applied Optics, **54**, F139–F143 (2015).

[22] M. Silva-López et al. *"Strain and temperature sensitivity of a single-mode polymer optical fiber"*, Optics Letters, **30**, pp. 3129–3131 (2005).

[23] R. M. Waxler, D. Horowitz, and A. Feldman. *"Optical and physical parameters of Plexiglas 55 and Lexan"*, Applied Optics, **18**, pp. 101–104 (1979).

5 | Thermo-Optic Effect

In this chapter we will characterize the thermo-optic effect in cylindrical MRs. We will present a theoretical description of how a temperature increment modifies the optical and mechanical properties of a material. These changes will affect the spectral position of the WGM resonances. Exploiting this effect, we will thermally characterize different optical fiber components such as UV-irradiated fibers, long period gratings (LPGs), and active fibers (Ytterbium and Holmium doped fibers). The WGM-based technique will allow us to measure the temperature increment in these components when they are illuminated by optical signals of moderate to high power ($\sim 1\,\mathrm{W}$ maximum powers). This technique provides useful information about how the atenuation coefficient of UV-irradiated photosensitive (PS) fibers increase due to the UV-illumination, and about the thermal profiles induced by the heating in doped fibers and gratings.

5.1 Theoretical description

The thermo-optic effect describes the change of the material refractive index due to a temperature variation. This effect is expressed as a function of $\Delta T = T - T_0$:

$$n\left(T\right) = n^{(0)}(T_0) + \Delta n\left(\Delta T\right) = n^{(0)}(T_0) + K_T \Delta T \tag{5.1}$$

where T_0 and $n^{(0)}$ are the temperature and the refractive index of the unperturbed MR, respectively. The thermo-optic coefficient is denoted as K_T, and it can be estimated from a derivation of the Lorentz-Lorenz relation [1]:

$$K_T = \frac{(n^2-1)(n^2+2)}{6n}\,(\psi - \gamma) \tag{5.2}$$

where γ is defined as the volume expansion coefficient, and ψ is the electronic polarizability. Since the thermo-optic effect is intrinsically isotropic, it is not necessary a tensorial description of the refractive index variation, contrarily to the strain-optic effect. The value of K_T is of the order of 10^{-3} to $10^{-6}\,\mathrm{K}^{-1}$, depending on the material. Although the thermo-optic coefficient itself also depends on the temperature, for the purposes of this work we will consider a constant value that depends only on the material medium. For example, for fused silica at room temperature, a typical value is $K_T = 8.57 \cdot 10^{-6}\,\mathrm{K}^{-1}$ [2].

To study how a temperature variation affects the spectral position of the WGM resonances in a cylindrical dielectric MR, we will take into account the changes in the optical properties of the medium, induced by the thermo-optic effect, together with the changes in the geometrical dimensions of the MR. When a material is subjected to a temperature increment, it suffers a volumetric thermal expansion. Thus, it induces a variation of the MR diameter, given by the thermal expansion coefficient of the material:

$$\frac{\Delta a}{a} = \alpha_T \Delta T \tag{5.3}$$

where Δa is the variation of the radius, and α_T is the thermal expansion coefficient. For fused silica, $\alpha_T = 0.5 \cdot 10^{-6}\,\mathrm{K}^{-1}$ [3].

Once we know the variation of the refractive index, Eq. (5.1), and the variation of the MR radius, Eq. (5.3), we can determine the shift of the WGM resonances by solving the characteristic equations of the WGMs. Besides, by taking into account the resonant condition, $m\lambda_R = 2\pi n_{\text{eff}}$, and carrying out a perturbative approach introducing the variation of the n_{eff} and a as a function of the temperature variation, we can obtain an expression for the relative shift of the resonances:

$$\frac{\Delta\lambda_R}{\lambda_R} = \left(\frac{1}{a}\frac{da}{dT} + \frac{1}{n_{\text{eff}}}\frac{dn_{\text{eff}}}{dT}\right)\Delta T \tag{5.4}$$

We will assume that the effective index of the modes are equal to the material refractive index to calculate the relative shift of the WGM resonances without solving the characteristic equations. For a fused silica MR, by considering the values of the thermo-optic and thermal expansion coefficients previously introduced, the relative shift per degree of temperature increment is $\left(\frac{\Delta\lambda_R}{\lambda_R}\right)/\Delta T \sim 6.4 \cdot 10^{-6}$.

In the experimental characterization that we will discuss in the following section, the temperature increment will be induced by the propagation of an optical signal of moderate power ($\sim 1\,\text{W}$) in the core of the optical fiber, which acts as the MR. Following the analysis developed in [4], we can relate the temperature increment to the pump signal that propagates in the core of the fiber and it is absorbed. The radial distribution of temperature is given by:

$$\Delta T(\rho) = \frac{\eta P_v b^2}{2ah} - \frac{\eta P_v b^2}{2k}\ln\left(\frac{\rho}{a}\right) \tag{5.5}$$

where η is the fraction of absorbed power turned into heat, a and b are the cladding and core radius respectevely, h is the heat transfer coefficient in air, k is the thermal conductivity of the silica, and $P_v = P_{\text{abs}}/V$ is the average pump power absorbed per unit volume. The value of η depends on the dopant. In conventional or photosensitive fibers doped with germanium, boron or aluminum, the non-radiative processes are the only ones allowed, and all the pump power absorbed is transformed into heat ($\eta = 1$). However, in active fibers, the processes for the relaxation of excited electrons of the dopants can be via two types of mechanisms: radiative and non-radiative. The second type is the one that contributes to the heating of the fibers. Thus, only a fraction of the absorbed optical power will result in an increase of temperature, this is, $\eta < 1$.

5.2 Experimental characterization

In order to measure the temperature variations induced by an optical signal on different optical fiber components, we employed a technique based on the analysis of the WGM resonances thermal shift.

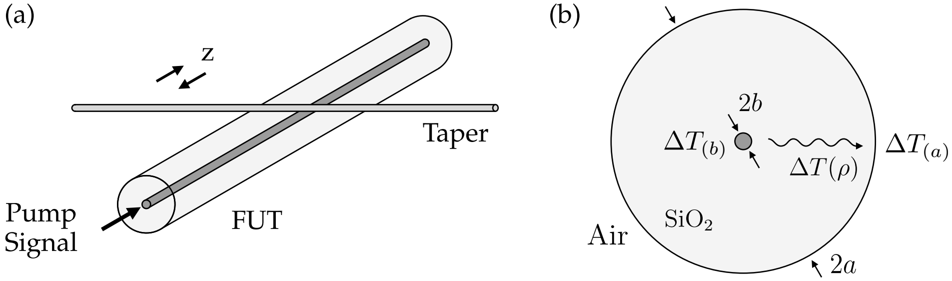

Figure 5.1: (a) Scheme of the experimental arrangement with pump signal and taper axial sweeping; (b) Scheme of temperature distribution in the cross section of the fiber.

To do the measurements, we performed a small modification to the general experimental arrangement shown in Fig. 3.1. The optical fiber device, which plays the role of the MR, was illuminated with an optical signal that propagates in its core. Simultaneously, the WGM resonances were excited with an auxiliary taper that was swept along the fiber under test (FUT), this allowed a characterization of the thermal profile point to point, see Fig. 5.1a. The spatial resolution of the technique is limited by the axial extension of the WGMs, which is $\sim 200\,\mu\text{m}$ in cylinders [5]. Moreover, the typical high Q-factor of the resonances, between 10^6 and 10^7, allows achieving very low detection limits (DL) for the temperature variations [6]. In our experiments, the detection limit is $0.03\,^{\circ}\mathrm{C}$, mostly due to the spurious vibrations and small temperature changes in the setup.

Just as in the strain-optic effect, the relative shift of the WGM resonances with the temperature is virtually independent of the azimuthal and radial orders. The thermal sensitivity of WGM resonances of different orders was theoretically calculated and the results showed that the difference is smaller than $1/10000$ per each °C of temperature increment, for a broad range of m and l values. This feature simplifies the utility of the described technique, since it does not matter which specific resonance is employed for measuring.

It should be noticed that the field of the illumination signal is mainly located in the core of the optical fiber components (we will assume single-mode propagation for the illumination signal). Thus, the source of the heating is located in the core, $\Delta T_{(b)}$. While, the WGM resonances are tightly confined in the outer region of the cladding and they will thermally shift according to the temperature increment at the surface of the fiber, $\Delta T_{(a)}$. Figure 5.1b shows a scheme of the heat distribution in the optical fiber cross section. Following the analysis developed in [4], it is possible to calculate the temperature increment at the interface of a silica fiber surrounded by air, in the steady-state:

$$\frac{\Delta T_{(b)} - \Delta T_{(a)}}{\Delta T_{(a)}} = -\frac{a \cdot h}{k} \ln\left(\frac{b}{a}\right) \tag{5.6}$$

By taking into account the conventional values of a silica optical fiber surrounded by air, the heating in the cladding is just 1.5% smaller than in the core [7].

The shift of the WGM resonances could be calibrated theoretically by taking into account the tabulated values of the thermo-optic and thermal expansion coefficients. However, the reported values vary depending on the reference and the shift rate can differ up to 20%. In this work, in order to obtain the most accurate value for our fibers, an experimental calibration is preferred. The details of the experimental procedure can be found in [7]. The shift of the WGM resonances is compared with that of a fiber Bragg grating (FBG) inscribed in the core of a doped fiber. The thermal shift of the Bragg wavelength of the FBG was previously calibrated in a temperature chamber. Then, the FBG was illuminated with an optical signal, and the WGMs were excited at a given point of it. The thermal shift of the WGM resonances were monitored and compared with the shift of the FBG, allowing to correlate the temperature increment with the WGM resonances shift. Using this calibration, the shift rate of the WGM resonances was measured to be $8.2\,\mathrm{pm}/^{\mathrm{o}}\mathrm{C}$. For comparison, the calculated thermal shift using the tabulated values presented in this chapter has a value of $9.97\,\mathrm{pm}/^{\mathrm{o}}\mathrm{C}$.

One of the main advantages of this technique is that it allows a thermal characterization point to point, which enables the measurement of the thermal profile along fiber components. Figure 5.2 shows the temperature increment induced by an illumination signal of two different optical fiber components: a homogeneously irradiated PS fibers (length: $3\,\mathrm{mm}$), and a PS fiber irradiated where some misalignment was introduced during the UV-irradiation process (length: $5\,\mathrm{mm}$). In both cases, the increment of the refractive index is produced by irradiating the core of a PS fiber and, as a consequence, the absorption coefficient also increases. Figure 5.2a shows a homogeneously irradiated fiber. The data shows a clear difference between the irradiated section ($z < 3$) and the pristine fiber ($z > 6$). It can be observed a smooth decay in an intermediate region due to the heat conduction of the silica and the transfer of heat to the surrounding air. In order to show the utility of the technique, we measured a section of an irradiated PS fiber with a non-homogeneous absorption profile, see Fig. 5.2b. This measurement shows how the WGM-based technique can be used to detect and quantify smooth undesired non-homogeneities that may occur during the fabrication of the fiber components, for example in fiber gratings. Also, the technique can be employed to measure the temperature increment induced for illumination signals at different wavelengths, as long as the fiber is single-mode.

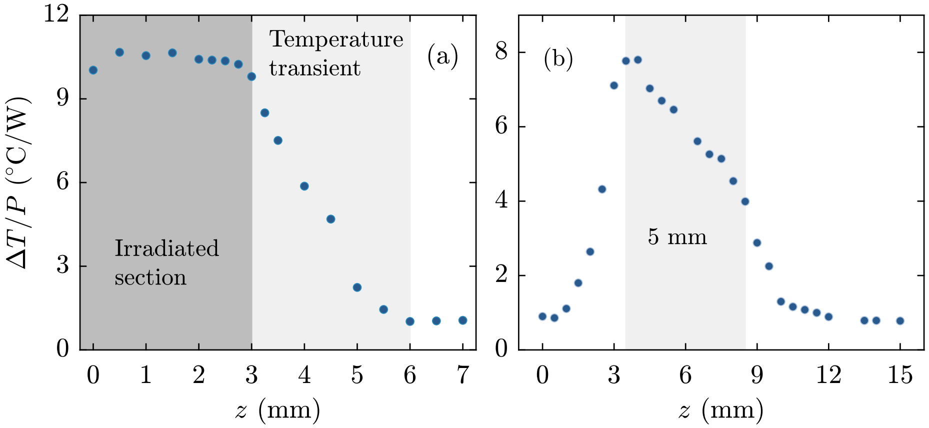

Figure 5.2: Temperature profile of irradiated PS fibers: (a) uniformly irradiated; (b) with some misalignment during the inscription.

In this work we used this technique to characterize different optical fiber components. We measured (i) the absorption coefficient of UV-irradiated PS fibers, (ii) the thermal profile induced by an illumination signal in a LPG, and (iii) the thermal effects in pumped rare-earth doped active fibers.

(I). Absorption in irradiated photosensitive fibers

When a PS fiber is exposed to a UV-irradiation, a permanent refractive index change is induced in the core. As a result, according to Kramers-Kronig relations, the absorption coefficient, α^{abs}, is also changed. In addition, the exposure of the fiber to the UV light levels usually required for gratings inscription may induce mechanical deformations in the fiber, such as corrugations due to the densification of the material [8]. This leads to an increment of the scattering losses, α^{scat}. Therefore, when a PS fiber is irradiated with UV light, its atenuation coefficient, α, increases due to both absorption and scattering mechanisms. Actually, $\sim 30\%$ of the refractive index variation induced by the UV illumination is due to densifications [9].

The measurement of the total losses introduced by the UV-irradiation of a PS fiber has been reported before in the literature using a technique based on the monitoring of the transmittance of the device during the UV-inscription [10]. The increment of α is a parameter of interest to optimize the fabrication of gratings, as in the case of long [11], or superimposed gratings [12]. The direct measurement of the transmission during the UV-irradiation provides information about the average value of the attenuation coefficient along the whole irradiated section. This measurement includes the contribution of the absorption and scattering losses. Meanwhile, the technique based on the measurement of the thermal shift of WGM resonances only accounts for the contribution of the absorption coefficient. Thus, by combining both measurement techniques, it is possible to evaluate both contributions separately.

We characterized different types of PS fibers:
(i) Fibercore PS980, NA ~ 0.13, cutoff wavelength 940 nm, attenuation 11.4 dB/km at 980 nm.
(ii) Fibercore PS1250/1500, NA ~ 0.13, cutoff wavelength 1214 nm, attenuation 131.1 dB/km at 1550 nm.
(iii) Fibercore SM1500, NA ~ 0.29, cutoff wavelength 1387 nm, attenuation 1.95 dB/km at 1550 nm.
(iv) Corning SMF28, NA ~ 0.14, cutoff wavelength 1260 nm, attenuation 0.188 dB/km at 1550 nm; this fiber was hydrogenated for 15 days (pressure: 30 bar) to increase its photosensitivity.

Figure 5.3 shows the setup employed to carry out the measurement of the total losses increment during the UV inscription. The UV fluence was provided by a doubled-argon laser at 244 nm. The lens employed to focus the light in the core of the PS fiber had spherical shape with a diameter of 75 µm. The total UV fluence delivered was $\sim 150\,\mathrm{J/mm^2}$ in all cases. For the inscription, the UV laser was swept back and forth along a 5 cm length of each fiber, repeatedly ($2.5\,\mathrm{J/mm^2}$ delivered per swept). During the inscription, the transmittance of a LED source (spectral range: $1520 - 1550$ nm) was measured after each swept of the UV laser.

The possible power fluctuations of the LED were monitored by employing a secondary OSA.

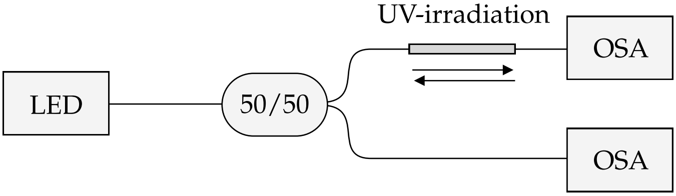

Figure 5.3: Scheme of the experimental setup employed to measure the attenuation coefficient increment during the UV-inscription.

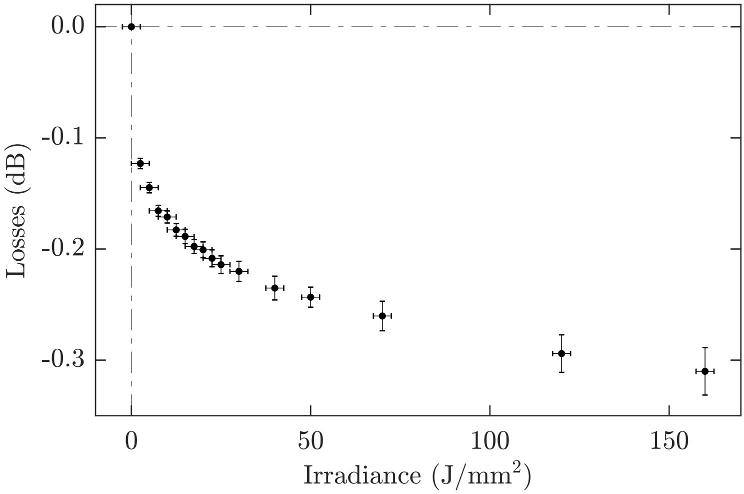

Figure 5.4: Direct measurement of the losses as the fiber is irradiated (length: 5 cm)

Figure 5.4 shows the results obtained from the measurements of the attenuation increment per each irradiation swept, for the PS980 fiber. The losses of the pristine PS980 fiber, α_1, were measured at $1550\,\mathrm{nm}$ by means of the cutback method. The value obtained was $120 \pm 0.5\,\mathrm{dB/km}$. The final losses after the UV inscription, α_2, were $6.2 \pm 0.4\,\mathrm{dB/m}$. This means that the total losses were increased in 52 ± 3 times. It should be remarked that the attenuation coefficient includes the contribution of absorption and scattering: $\alpha = \alpha^{\mathrm{abs}} + \alpha^{\mathrm{scat}}$.

Once this UV-irradiation process was finished, the same section of the fiber was characterized by means of the thermal shift of the WGM resonances, when an illumination signal (at $\sim 1550\,\text{nm}$) was launched to it. This optical signal launched through the irradiated fiber was provided by a CW laser source: it consisted on an amplified tunable laser with maximum CW power $1\,\text{W}$, tuning range $1530 - 1565\,\text{nm}$, and linewidth $< 20\,\text{pm}$. The laser signal propagating through the fiber induced a temperature increment, then, we measured the wavelength shift of the WGM resonances as the illumination power was increased. The measurement was performed at two different points, one within the irradiated section of the fiber and one outside of it (this is, the pristine fiber). Figure 5.5 shows the measurements of the temperature variation as the illumination power was increased. Note that it was not observed any sign of saturation, for this range of power. The temperature of the irradiated section increased at a rate of $26.48 \pm 0.15\,^{\circ}\text{C/W}$, and at $0.718 \pm 0.014\,^{\circ}\text{C/W}$ in the pristine fiber. The ratio between the slopes shows that the temperature increment in the irradiated section is 36.9 ± 0.7 times larger than in the pristine section.

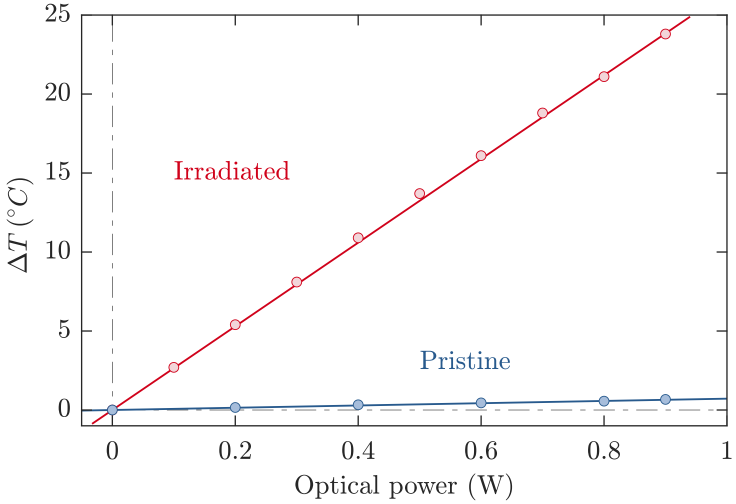

Figure 5.5: Thermal heating of the PS980 fiber as a function of the optical power of the illumination signal at $1550\,\text{nm}$.

The temperature increment was measured at different wavelengths within the amplification range ($1530 - 1565$ nm). We observed the same linear trend of the heating, showing that the variation of the illumination signal absorption was smooth for this wavelength range.

The same set of measurements was repeated for all the different fibers mentioned before: PS1250/1500, SM1500 and hydrogenated SMF28. The illumination signal was centered at 1550 nm in all the cases. Table 5.1 compiles the measurements.

	WGM resonances		**Direct measurement**	
	$\Delta T/P$ (°C/W)		**α (dB/km)**	
	Irradiated	Pristine	Irradiated	Pristine
PS980	26.48 ± 0.15	0.718 ± 0.014	6200 ± 400	$120 \pm 2^{(1)}$
PS1250	30.80 ± 0.17	0.768 ± 0.014	6600 ± 400	$131.1^{(2)}$
H_2-SMF28	23.48 ± 0.13	0.815 ± 0.012	5600 ± 400	n/a$^{(3)}$
SM1500	1.20 ± 0.03	$< 0.03^{(4)}$	370 ± 90	$1.95^{(2)}$

$^{(1)}$ Cutback measurement, $^{(2)}$ Nominal value, $^{(3)}$ Non-available, $^{(4)}$ Below detection limit

Table 5.1: Measurement of thermal heating and attenuation coefficient of different irradiated fibers (illumination wavelength: 1550 nm).

Since in this case we are not dealing with active fibers, we will assume that the heating over the transversal section of the fiber, at a given axial position, is set by the absorption coefficient, which implies that $\eta = 1$. For these fibers, the absorption is still low enough to consider that the exponential decay of the illumination signal is very small along the axial direction (length of the FUT $\sim$ 5 cm). Therefore, the illumination power absorbed can be approximated as: $P_{\text{abs}} = P_0 \left(1 - e^{-\alpha^{\text{abs}} \cdot z}\right) \approx P_0 \cdot \alpha^{\text{abs}} \cdot z$. Thus, we can derive an expression from Eq. (5.5) to directly relate the temperature increment with the absorption coefficient:

$$\frac{\Delta T}{P_0} = \frac{1}{2\pi a h}\alpha^{\text{abs}} \tag{5.7}$$

where a is the fiber radius and h is the heat transfer coefficient (for standard fiber: $a = 62.5\,\mu\text{m}$ and $h = 81.4\,\text{W}\cdot\text{m}^{-2}\cdot\text{K}^{-1}$ [4]). Then, the ratio of the temperature increment between two different points that experience a different heating along the FUT, see Fig. 5.6, is given by:

$$\frac{\Delta T_2}{\Delta T_1} = \frac{\alpha_2^{\text{abs}}}{\alpha_1^{\text{abs}}} \tag{5.8}$$

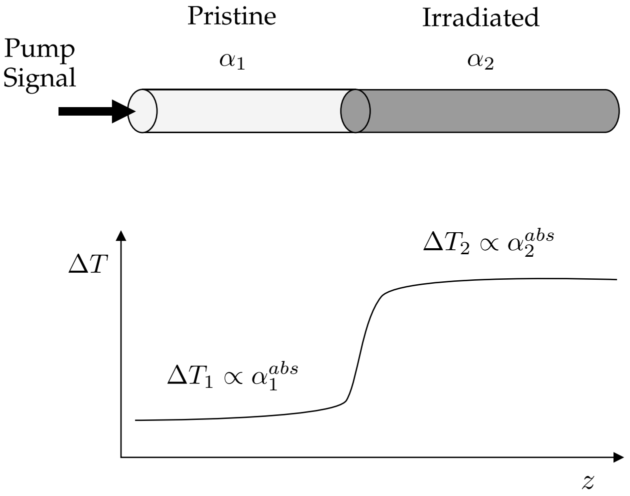

Figure 5.6: Scheme of a fiber with a pristine and an irradiated section, and the corresponding heating.

As we mentioned before, while the WGM technique allows to quantify the variation in the absorption coefficient due to UV-irradiation, the transmission technique also accounts for the contribution of the scattering. The comparison of both techniques is compiled in Tab. 5.2.

From these results, together with the ones showed in the Tab. 5.1, we can establish several interesting conclusions. First, the absorption coefficient is substantially increased by a factor between 28 (H_2-SMF28) and 40 (PS1250). This is consistent with the increment in the refractive index exploited for the inscription of gratings. Since the increment of α^{abs} is considerable, the temperature increment induced by a signal of moderate or high power will not be negligible. FBGs and LPGs might experience shifts and chirps [13] that should be taken into account in, for example, tuning of gratings in lasers or compensation of the dispersion in distributed feedback cavities.

	WGM resonances	**Direct measurement**
	$\boldsymbol{\alpha_2^{\text{abs}}/\alpha_1^{\text{abs}}}$	$\boldsymbol{\alpha_2/\alpha_1}$
PS980	36.9 ± 0.7	52 ± 3
PS1250	40.1 ± 0.8	50 ± 3
H_2-SMF28	28.8 ± 0.5	n/a$^{(1)}$
SM1500	$> 40^{(2)}$	190 ± 50

$^{(1)}$ Non-available, α_1 unknown, $^{(2)}$ ΔT_1 below detection limit

Table 5.2: Comparison of results obtained by the two techniques.

Second, the results show that α_2/α_1 is systematically higher than $\alpha_2^{\text{abs}}/\alpha_1^{\text{abs}}$. This implies two facts:

(i) the relative contribution of the absorption coefficient decreases after the UV-irradiation, i.e., $(\alpha_2^{\text{abs}}/\alpha_2) < (\alpha_1^{\text{abs}}/\alpha_1)$.

(ii) the relative contribution of scattering to the overall losses increases, therefore, $(\alpha_2^{\text{scat}}/\alpha_2^{\text{abs}}) > (\alpha_1^{\text{scat}}/\alpha_1^{\text{abs}})$.

We can conclude, then, that α^{scat} increases faster than α^{abs} with UV-irradiation. The above conclusions are virtually free of any heat dissipation model, since they have been carried out using experimental values. However, they are limited to the relative values between two points.

Finally, we will take into account Eq. (5.7) and the values of a and h reported in [4] for a silica fiber, to obtain absolute values for the absorption coefficient. By combining the calculated values of α^{abs} with the measurement of the attenuation coefficient, we can also obtain the absolute values for the scattering contribution to the overall losses ($\alpha^{\text{scat}} = \alpha - \alpha^{\text{abs}}$). Table 5.3 summarizes the numerical values obtained.

	α^{abs} (dB/km)		**α^{scat} (dB/km)**	
	Irradiated	Pristine	Irradiated	Pristine
PS980	3680 ± 20	99.7 ± 1.9	2500 ± 400	20 ± 3
PS1250	4280 ± 20	106.6 ± 1.9	2300 ± 400	24.5 ± 1.9
H_2-SMF28	3260 ± 18	113.1 ± 1.7	2300 ± 400	n/a$^{(1)}$
SM1500	167 ± 4	$< 1.95^{(2)}$	200 ± 90	$< 1.95^{(2)}$

$^{(1)}$Non-available, hydrogenated fiber, $^{(2)}$Nominal value

Table 5.3: Absorption and scattering contributions to the overall attenuation coefficient, $\alpha = \alpha^{\text{scat}} + \alpha^{\text{abs}}$

It can be seen that, after the UV-irradiation, in most cases both contributions are of the same order of magnitude, even though α^{scat} is smaller, between 0.53 and 0.70 times α^{abs}. The only exception is for the SM1500 in which α^{scat} is 1.19 times α^{abs}. For the pristine fibers PS980 and PS1250/1500, the α^{scat} is 0.20 and 0.23 times α^{abs}, respectively. This confirms that the UV-irradiation produces a faster increment of the scattering coefficient than that of the absorption.

Thus, by combining the technique based on the thermal shift of the WGM resonances with the conventional measurement of the fiber attenuation, we can quantify separately the absorption and scattering contributions to the overall losses. This information can be employed, for example, to optimize the design of novel active doped fibers or PS fibers, in order to decrease the scattering losses contributions. Moreover, the WGM-based technique allows to characterize the attenuation coefficient point to point along a short section of the FUT, while the conventional technique obtains average values of the whole length of the fiber.

(II). Thermal profile of LPGs

By taking advantage of the spatial resolution of the WGM-based technique, we measured the thermal profile of a LPG illuminated with a signal of moderate power. This technique has been used before to thermally characterize FBGs, showing significant temperature variations on gratings with short length [14].

The LPG used in the experiments was inscribed in a germanium-silicate boron co-doped, PS fiber (Fibercore PS1250/1500), using the same UV laser described before, and a point to point technique. The attenuation peak of the LPG was centered at $\lambda_R = 1535.3\,\text{nm}$ (spectrum shown in Fig. 5.7a), and corresponds to the coupling from the fundamental mode LP_{01} to the LP_{07} cladding mode. The LPG parameters were: $11.7\,\text{mm}$ length, $16\,\text{dB}$ maximum attenuation, 3-dB bandwidth of $34.8\,\text{nm}$, and the pitch was set to $418.4\,\mu\text{m}$. It was illuminated by optical signals of moderate power ($\sim 1\,\text{W}$) at different wavelengths, corresponding to different transmittances of the LPG. The pump power is provided by the same tunable laser centered in $1550\,\text{nm}$ mentioned in the previous section.

We measured the temperature profile along the LPG with the optical pump signal tuned at: (i) the resonant wavelength of the LPG, $1535.3\,\text{nm}$; (ii) the $-4\,\text{dB}$ point on the right edge of the LPG, $1553\,\text{nm}$; (iii) the $-1\,\text{dB}$ point on the right edge of the LPG, $1565\,\text{nm}$. These points are indicated in Fig. 5.7a for clarification and the results are shown in Fig. 5.7b. In all cases the temperature profile is not uniform, and it depends on the pump laser wavelength tuning respect the LPG. We can explain this difference as follows: as the illumination signal propagates along the LPG, the grating couples the light to the cladding modes, in our case, LP_{07}. We performed a numerical simulation to identify which mode corresponds to the LPG resonance studied. The spectrum of the LPG showing four resonances is compared with the dispersion curves of the fiber modes. To match the experimental position of the resonances with the calculated ones, we considered the phase-matching condition of the LPG, for the different modes. From this simulation, we deduced that the cladding mode coupled with the fundamental mode for the resonance centered at $1535.3\,\text{nm}$ is the LP_{07}, see Fig. 5.8. The variation of the absorption coefficient is introduced in the core of the fiber during the UV-inscription, thus the average will be constant along the entire length of the grating. However, because of the action of the LPG, the amount of light guided by the fundamental mode (LP_{01} mode) will vary with z, and this effect is the main responsible for the non-uniform heating.

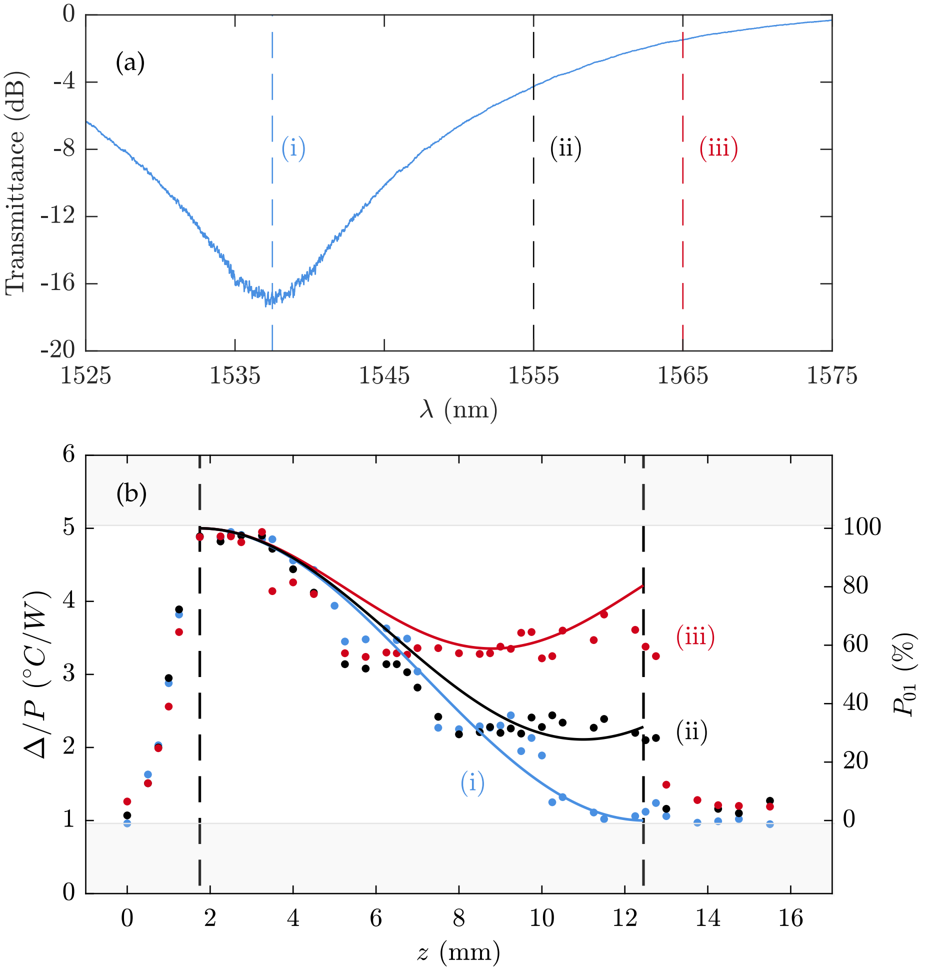

Figure 5.7: (a) Optical spectrum of the LPG; (b) Temperature profile of the LPG for different wavelengths of the illuminating signal.

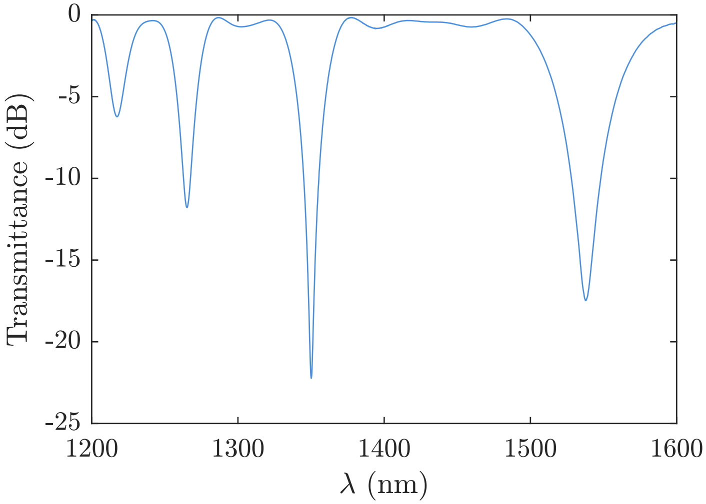

Figure 5.8: Spectrum of the LPG with four resonances that we employed to calculate the corresponding excited cladding modes.

As it can be observed in Fig. 5.7b, the temperature variations correlate well with the evolution of the fraction of light guided by the LP_{01} mode along the LPG. At the entrance, where the maximum heating is achieved, all the power is guided by the fundamental mode, $P_{01} = 100\%$. The 73% of the power flow of this mode is located in the core, and the remaining 27% is located in the cladding. As the light propagates along the LPG, the power of the illumination signal is coupled to the LP_{07}. The 98% of the power flow of this cladding mode is distributed over the cladding, while only the 2% is located in the core. Figure 5.9 illustrates the intensity and power distribution of the LP_{01} and LP_{07} modes over the transversal section of the fiber. Therefore, since the amount of power of the LP_{07} located in the core is negligible, the fraction of the fundamental mode along the LPG is the main responsible of the heating.

At the output of the LPG, where the optimal coupling is achieved for the resonant wavelength, curve (i), the light is mostly guided by the LP_{07} ($P_{01} = 0\%$ and $P_{07} = 100\%$), and the temperature change is $\sim 1\,^{\circ}\text{C}$. Thus, 2% of the optical power contributes to the heating. It is worth to note that the value for the heating in this condition is similar to the one measured for a pristine fiber when the light is guided by the LP_{01} mode. For the cases corresponding to $-4\,\mathrm{dB}$ and $-1\,\mathrm{dB}$ values, curves (ii) and (iii), at the output of the grating there is still a significant part of the signal guided by the fundamental mode, 32% and 80% respectively. As a consequence, the heating is larger than at the resonant wavelength.

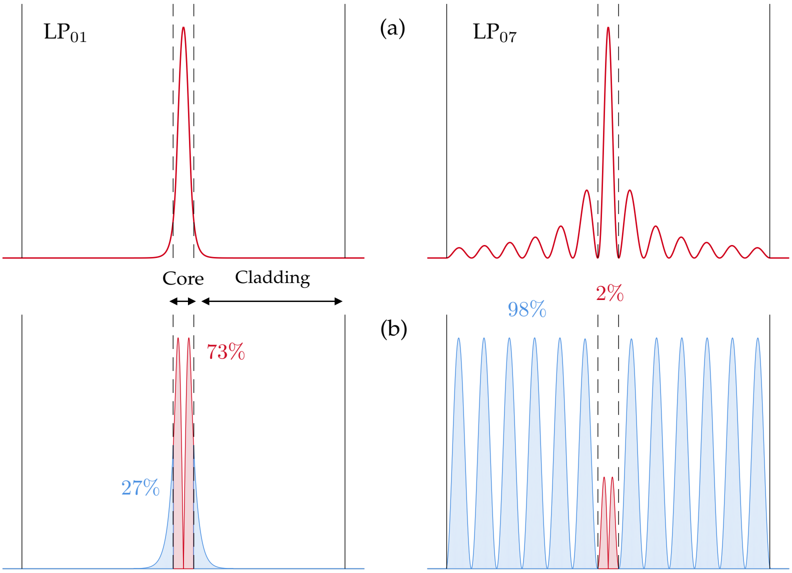

Figure 5.9: (a) Intensity distribution of the LP_{01} and LP_{07} modes; (b) The red area represents the fraction of power located in the core, while the blue one represents the fraction of power located in the cladding.

It is important to remark that these thermal profiles are not a consequence of an inhomogeneous absorption profile, as in the case presented in Fig. 5.2b. The different heating along this optical fiber device is due to the coupling between the fundamental mode and the cladding mode coupled by the grating. As it is reported in [14], if the illumination signal wavelength is not at the vicinities of the resonant wavelength, the thermal profile corresponds to a homogenous irradiated fiber. The heating observed in this case would be half of the value of the uniformly irradiated fibers, since only the high index periods of the LPG are the ones where the α^{abs} is increased, see Fig. 5.10.

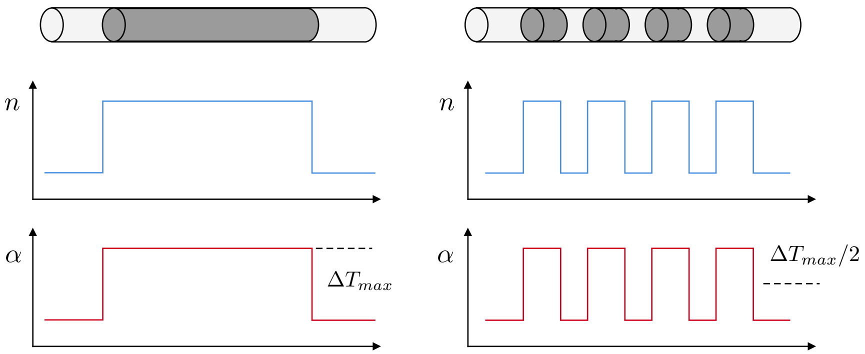

Figure 5.10: Index profile of a homogeneous irradiated fiber and a fiber grating.

These measurements show that a signal of moderate or high power can produce a non-homogeneous thermal profile in the LPG even in the case of a grating without defects. Also, that these profiles are more pronounced as the pump signal wavelength gets closer to the resonant wavelength (which in practice is the wavelength that will be used for operation). These variations may induce chirps that could affect the spectral and phase properties of the optical fiber device. The measurement of these effects will be studied in future works.

(III). Thermal effects in rare-earth doped fibers

The WGM-based measurement technique can be employed to thermally characterize active fibers. Active fibers are usually pumped with optical signals of significant power, specially if they are used for laser applications. Thus, the study of the heating that these fibers suffer when they are in operation is a topic of interest. Rivera-Pérez *et al.* studied these effects in Er/Er-Yb doped fibers, pumped at 980 nm. Temperature increments as high as 80 °C were demonstrated. We should point out that the specific dopant will influence on the thermal heating; for example, Er/Yb co-doped fibers suffer a heating almost 70 times larger than the Yb doped fibers [7].

In this work, we studied the thermal effects in optical fibers doped with different concentrations of Holmium. In the last years, Ho became of great interest due to the developing of lasers beyond 2 µm. Several applications arose, such as laser surgery, LIDARs, *etc*. In optical fibers doped with this element, the lasing is usually achieved by two methods [15, 16]:

(i) with a pump wavelength close to the absorption bands of the Ho^{3+}, one centered at ~ 1.15 µm (near-IR), and the other centered at ~ 1.95 µm (mid-IR).

(ii) adding other dopants, such as Ytterbium or Thulium, that allows to employ pump wavelengths different from those of the absorption bands, for example 975 nm.

Figure 5.11 shows a schematic diagram of the energy levels and processes involved at the different types of pumping. The non-radiative transitions are the ones that contribute to the heating of the fiber (for example, $^5I_6 \rightarrow {}^5I_7$).

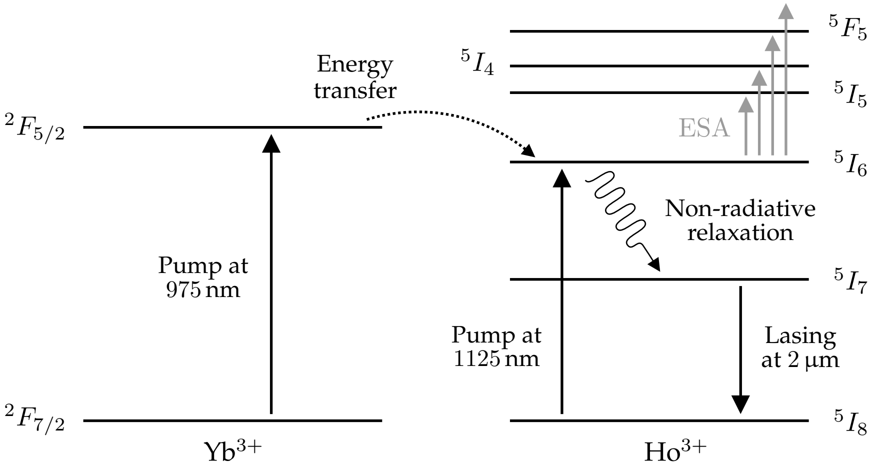

Figure 5.11: Simplified energy level diagram of the Yb^{3+} and Ho^{3+} co-doped system showing the absorption and laser transitions, and the energy transfer processes.

We characterized three different types of Ho-doped optical fibers: two fibers (HDF1 and HDF2) doped only with different concentrations of Ho^{3+}, with a ratio of doping levels of (HDF2/HDF1) ~ 1.5; and a fiber co-doped with Yb^{3+}, YHDF. Two CW single-mode lasers of 400 mW were employed for the pump signal: one centered at $\sim 1.125\,\mu\text{m}$ for the fibers HDF1 and HDF2, and other one at $975\,\text{nm}$, for the YHDF. In all the cases, the pump signal is launched to the core of the active fiber.

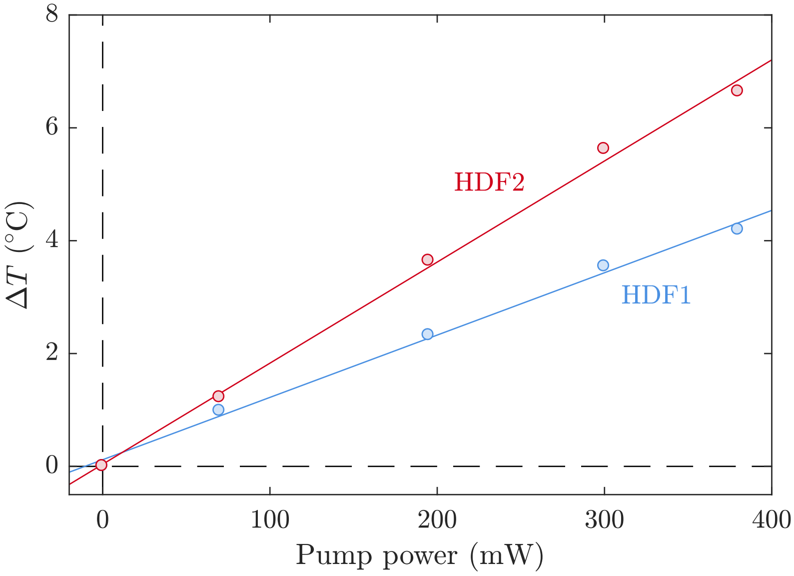

Figure 5.12: Temperature increment of the HDF1 and HDF2 with the pump signal power. Pump wavelength at $\sim 1.125\,\mu\text{m}$.

The measurement technique was analogous to the one described before. We measured the thermal shift of the WGMs at a point of the active fiber, when the pump signal was launched through it. Figure 5.12 shows the increase of the heating of the fibers HDF1 and HDF2 with the pump power. The heating rate of the HDF1 fiber was $11.1 \pm 0.2\,°\text{C/W}$, while for the HDF2 fiber was $18.0 \pm 0.3\,°\text{C/W}$. Therefore, the temperature increment suffered for the fiber doped with more concentration of Ho^{3+} is ~ 1.6 times larger, which is in concordance with the concentration ratio (HDF2/HDF1) ~ 1.5. In the power range studied, the temperature increment showed a linear trend with the pump and we did not observe any sign of saturation. Moreover, the temperature increment was measured at different positions along the active fibers (total section length: $15\,\text{mm}$), and heating showed the same linear trend. Therefore, we can assume that, for these lengths, the exponential decay of the pump is very small along the active fiber.

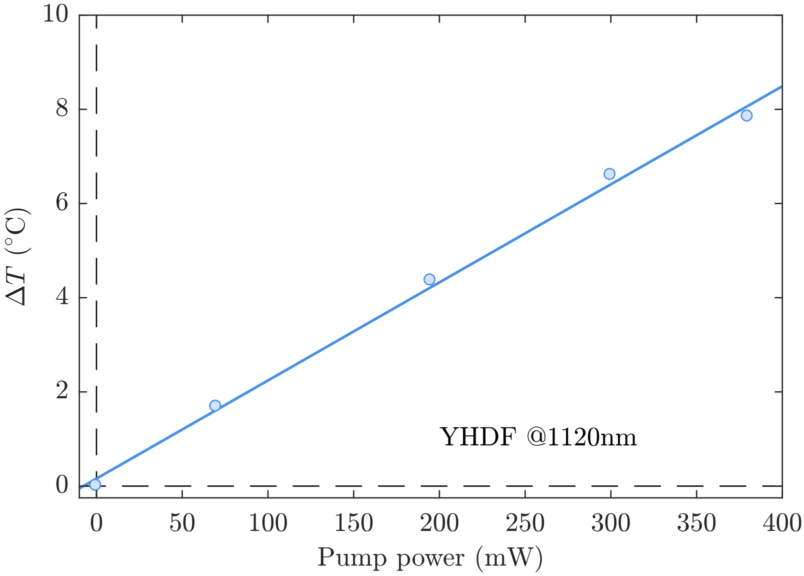

Figure 5.13: Temperature increment of the YHDF with the pump signal power. Pump wavelength at ~ 1.125 µm.

Figure 5.13 shows the temperature increment of the YHDF with the 1125 nm pump. As it can be observed, the heating is comparable with the fiber only doped with Ho^{3+}, HDF2. The heating rate was 20.9 ± 0.4 °C/W and, again, it shows a linear trend with the pump power with no evidence of saturation. The same fiber was illuminated with a signal at 975 nm (transition $^2F_{7/2} \rightarrow {}^2F_{5/2}$). In this case, the temperature increment was much larger than for the previous pump wavelength, 1125 nm. For the range of powers studied, the heating does not show a linear trend at the highest values of power. As it can be observed in Fig. 5.14, for 400 mW of pump power, the temperature reached in the fiber exceeds 200 °C. Thus, the heating of the fiber changes dramatically depending on the pump wavelength. In the case of YHDF, the absorption is very large and the pump power propagating through the fiber droped to zero in few centimeters. The measurements showed in Fig. 5.14 were carried out exciting the WGMs 1 mm after the splice with the SM980 fiber of the pump laser.

We should conclude then, that when the fiber is co-doped with Yb^{3+}, the thermal effects induced by the pump signal must be taken into account, since the heating can be critical. On the other hand, when the fiber was pumped at 1125 nm, the temperature increment induced depends linearly on the Ho^{3+} concentrations of our samples, and it is kept below 21 °C/W.

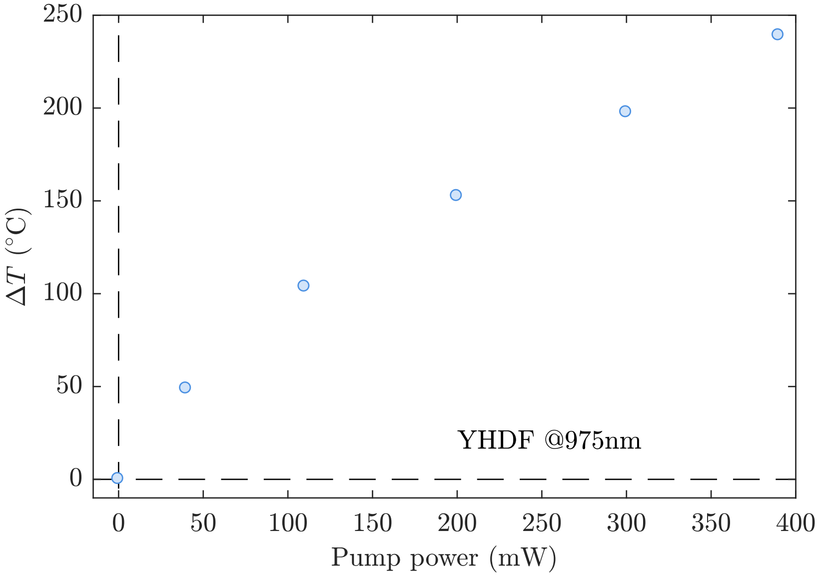

Figure 5.14: Temperature increment of the YHDF with the pump signal power. Pump wavelength at $\sim$ 975 nm.

To conclude, we showed that the WGM-based technique can be used to study the thermal effects induced by pump signals at the different wavelengths of absorption of the dopants Ho^{3+} and Yb^{3+}. This technique can be useful to characterize the effect of different concentrations and types of dopants. This information can be employed to design new active fibers with different rare-earth elements that enhance the radiative processes and minimize the thermal effects.

Other studies can be carried out in active fibers by means of the WGM-based technique, but they are beyond the scope of this work. For example, with a model of the fraction of power turned into heat, we can use the temperature measurements to quantify the contributions of the non-radiative absorption and the scattering losses in active fibers. Moreover, if gratings are inscribed in this fibers for the developing of lasers, the heating induced may produces undesired chirps and variations of the dispersion in the laser cavity.

References

[1] E. Palik. *"Handbook of optical constants of solids"*, Academic Press, San Diego (1998).

[2] D. B. Leviton and B. J. Frey. *"Temperature-dependent absolute refractive index measurements of synthetic fused silica"*. 2006 (cit. on p. 76).

[3] M. Weber. *"Handbook of optical materials"*, CRC Press, Boca Raton (2003).

[4] M. K. Davis, M. J. F. Digonnet, and R. H. Pantell. *"Thermal Effects in Doped Fibers"*, Journal of Lightwave Technology, **16**, p. 1013 (1998).

[5] M. Sumetsky. *"Mode localization and the Q-factor of a cylindrical microresonator"*, Optics Letters, **35**, pp. 2385–2387 (2010).

[6] I. M. White and X. Fan. *"On the performance quantification of resonant refractive index sensors"*, Optics Express, **16**, pp. 1020–1028 (2008).

[7] E. Rivera-Pérez, I. L. Villegas, A. Díez, M. V. Andrés, J. L. Cruz, and A. Rodríguez-Cobos. *"Measurement of Pump-Induced Temperature Increase in Doped Fibers Using Whispering-Gallery Modes"*, IEEE Photonics Technology Letters, **25**, pp. 2498–2500 (2013).

[8] B. Poumellec, P. Guénot, I. Riant, P. Sansonetti, P. Niay, P. Bernage, and J. Bayon. *"UV induced densification during Bragg grating inscription in Ge:SiO$_2$ preforms"*, Optical Materials, **4**, pp. 441–449 (1995).

[9] R. Kashyap. *"Fiber Bragg gratings"*, Academic Press, Burlington, MA (2010).

[10] J. Canning, M. Åslund, and P.-F. Hu. *"Ultraviolet-induced absorption losses in hydrogen-loaded optical fibers and in presensitized optical fibers"*, Optics Letters, **25**, pp. 1621–1623 (2000).

[11] M. Gagné, S. Loranger, J. Lapointe, and R. Kashyap. *"Fabrication of high quality, ultra-long fiber Bragg gratings: up to 2 million periods in phase"*, Optics Express, **22**, pp. 387–398 (2014).

[12] A. Arigiris, M. Konstantaki, A. Ikiades, D. Chronis, P. Florias, K. Kallimani, and G. Pagiatakis. *"Fabrication of high-reflectivity superimposed multiple-fiber Bragg gratings with unequal wavelength spacing"*, Optics Letters, **27**, pp. 1306–1308 (2002).

[13] J. Lauzon, S. Thibault, J. Martin, and F. Ouellette. *"Implementation and characterization of fiber Bragg gratings linearly chirped by a temperature gradient"*, Optics Letters, **19**, pp. 2027–2029 (1994).

[14] M. Delgado-Pinar, I. L. Villegas, A. Díez, J. L. Cruz, and M. V. Andrés. *"Measurement of temperature profile induced by the optical signal in fiber Bragg gratings using whispering-gallery modes"*, Optics Letters, **39**, pp. 6277–6280 (2014).

[15] A. V. Kir'yanov, Y. O. Barmenkov, and I. V. Garcia. *"2.05 μm holmium-doped all-fiber laser diode-pumped at 1.125 μm"*, Laser Physics, **27**, p. 085101 (2017).

[16] S. D. Jackson and S. Mossman. *"Diode-cladding-pumped Yb^{3+}, Ho^{3+}-doped silica fiber laser operating at 2.1-μm"*, Applied Optics, **42**, pp. 3546–3549 (2003).

6 Locking techniques and applications

For nonlinear applications of WGMs, the detuning between the laser and the WGM resonant wavelength needs to be constant (ideally null, for a maximum coupling of the energy in the MR). In this chapter we will describe the fundamentals of the locking techniques used to stabilize this parameter. We will detail the problems to match the laser wavelength with the WGM resonance, and propose different techniques to overcome these difficulties. We will propose the design of a feedback system that allows an active locking based on the strain-optic and the thermo-optic effect in MRs. We will describe the experimental implementation of different alternatives: laser-locking, strain-locking, and an auxiliary all-optical pump-locking technique, being the two last ones novel techniques that have not been reported before for cylindrical MRs, up to our knowledge. Due to the advantages of the two lasts processes compared to the first one, we will characterize their performance against external perturbations. Exploiting the passive and active locking techniques, we will excite and measure optical nonlinear effects in spherical, silica MRs, and we will show the improvements that our proposals present. Finally, we will carry out a study of optomechanical phenomena on bubble MRs, by characterizing the vibrational mechanisms and their main features as a function of the energy density.

6.1 Locking fundamentals

WGM-based silica MRs with different geometries (such as cylindrical, spherical or toroidal shaped), show low optical losses, high- or ultra-high Q factors, and small mode volumes. These features make such MRs suitable to be used for the study of a broad range of nonlinear phenomena in materials with low nonlinear coefficients, while using low launched optical powers. For example: optical parametric oscillation (OPO) [1], stimulated Raman scattering (SRS) [2], stimulated Brillouin scattering [3], or third-harmonic generation (THG) [4], have been demonstrated in MRs using WGMs. Besides, it is possible to find the implementation of WGM-based MR in applications that involve nonlinear effects, such as optical frequency combs [5], ultralow-threshold laser [6], or cavity opto-mechanics [7]. One of the most important features of these microcavities is the excitation of nonlinear effects at low dc power. The high-Q factors and the small mode volumes produce large modal field intensities within the cavity and, consequently, enormous circulating optical powers for low power launched signals. For a given coupled, input power, P_{in}, the circulating intensity within the MR can be approximated by the expression: $I \approx P_{in}\,(\lambda/2\pi n_1)\,(Q/V)$. For a spherically shaped MR with a Q-factor of $\sim 10^8$, a mode volume of $500\,\mu\mathrm{m}^3$, and an input power of $1\,\mathrm{mW}$, the circulating power exceeds $1\,\mathrm{GW/cm}^2$ [8]. Nevertheless, these huge circulating powers, that are crucial to observe nonlinear optical phenomena, can result in thermal nonlinearities [9]. The circulating WGM power is partially absorbed by the MR material (even when it is low-loss, the amount of absorbed power is significant due to the huge circulating power), and it can lead to the heating of the MR. This heating induces variations of the refractive index, and changes of the MR geometrical sizes, resulting in a thermal shift of the WGM resonances that can not be neglected (it can exceed several times the cavity linewidth). In contrast to the linear thermo-optic effect described in Chapter 5, the value of the temperature variation for the thermal nonlinearity, that is, the heating, depends on the WGM optical field intensity, that is, a self-heating [10]. Due to this nonlinear thermal effect, a broadening

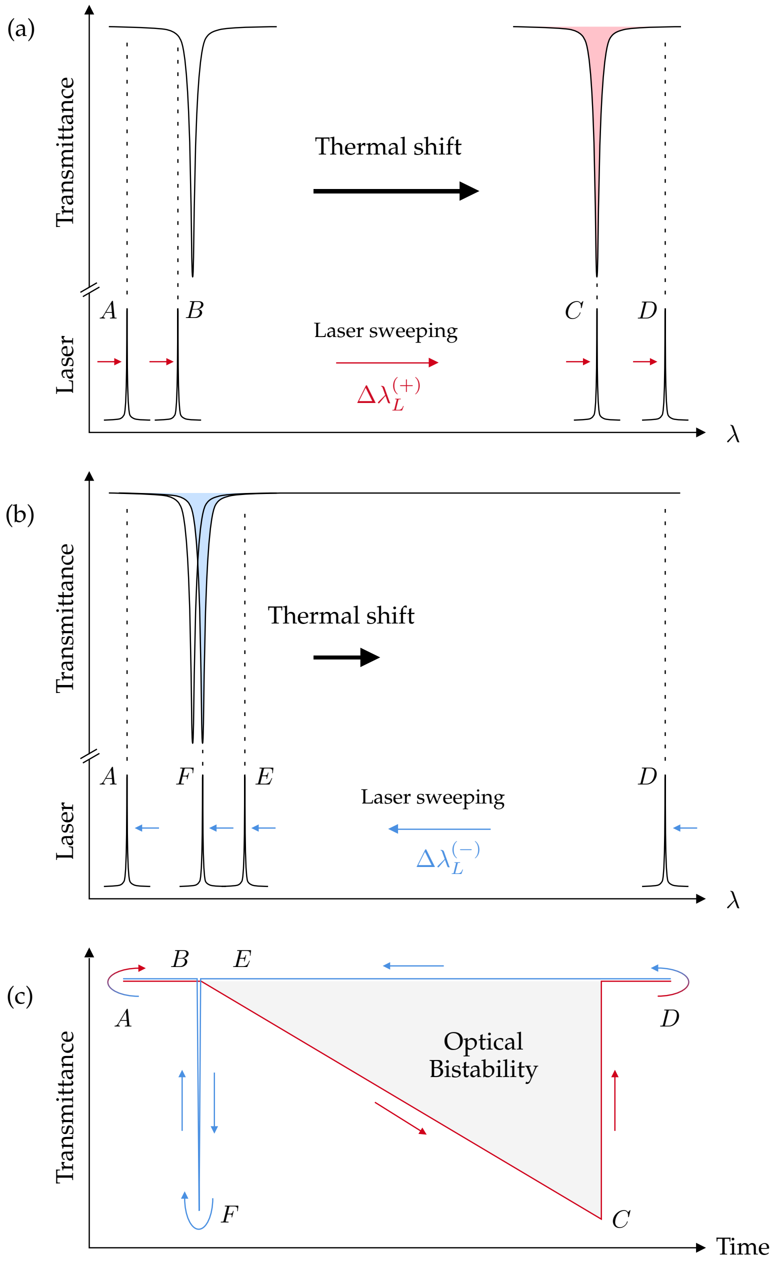

Figure 6.1: Relative spectral position of a laser and a WGM resonance for different scanning directions of the laser: (a) toward longer wavelengths, and (b) toward shorter wavelengths. (c) Illustration of the dynamical thermal behavior of a WGM resonance scanned by a laser.

and compression of the resonance line shape can be observed during the matching of the laser wavelength with the WGM resonances.

Figure 6.1 illustrates the typical dynamical, nonlinear thermal behavior of a WGM resonance scanned with a laser. Depending on the direction (toward longer or shorter wavelengths) and the scanning speed of the laser, the resonance shape suffers different distortions from its original, Lorentzian profile, cold-shape. We show two scenarios depending on the laser direction: (i) it is scanned toward longer wavelengths, or (ii) it is scanned toward shorter wavelengths (red and blue arrows in Fig. 6.1 respectively). Figures 6.1a and 6.1b depict the key spectral position differences between the WGM resonance and the laser wavelength. Figure 6.1c shows the differences in the transmittance behavior depending on the sweeping direction of the laser.

(i) First, we will consider the situation when the laser is detuned from the resonance at its left, point-A. As the laser scans toward longer wavelengths, it approaches the WGM resonance, point-B, and the MR starts to increment its temperature. Consequently, the resonance thermally shifts toward longer wavelengths in the same direction of the laser scanning. The temperature rises as long as the thermal shift compensates the laser sweeping (we are considering that the scan of the laser is faster than the shift of the resonance) and the hot-shape of the resonance broadens. When the laser exceeds the minimum point of transmittance, point-C (this is, the laser and the WGM resonance are in the same spectral position), the heating terminates resulting in a fast drop of the coupling. The laser continues its sweeping and the resonance returns to the cold-spectral position, point-D. The transmittance of the forward sweeping laser follows the curve $-ABCD-$ in Fig. 6.1c.

(ii) In the reverse scenario, we will consider that, at the beginning, the laser is completely detuned from the resonance at its right, and there is no energy coupling, point-D. As the laser, which scans towards shorter wavelengths, approaches the resonance, point-E, the MR starts to heat-up. In this case, the WGM resonance thermally shifts in the opposite direction to the laser sweeping, resulting in a narrowing of the shape of the resonance, point-F. The laser, which continues its sweeping, crosses the central position of the WGM resonance, and returns to its cold-spectral position, point-A. The transmittance of the backward sweeping laser follows the curve $-DEFA-$ in Fig. 6.1c.

Therefore, the evolution of the output signal depends on the sweeping direction of the laser and the initial detuning between the laser and the WGM resonance, resulting in a bistable behavior. Due to the high-Q factors and the microscales of the WGM resonators, the threshold of this bistability is very low, in the order of the μW [11]. Thus, this effect is present in all the experiments that involve optical nonlinear phenomena.

In the different experiments described throughout this work up to this point, the influence of the thermal nonlinearities in the results for our experiments are negligible since we employed a fast laser sweeping velocity ($\sim$ $10\,\mathrm{nm/s}$) compared to the thermal shift. Moreover, the input power, and therefore the circulating WGM field, was also set to be a small value. For those experiments, the objective was to interrogate the spectral position of the WGM resonances, thus, nonlinear thermal effects were avoided.

It is worth noting that, even for the low laser powers employed in the linear experiments of Chapters 3-5, we observed thermal nonlinearities if we reduced the scan velocity, thus this was the key parameter to control. The setup used to characterize this effects was the same one described in Fig. 3.1. The laser power was set to $10\,\mathrm{mW}$. Figure 6.2 shows the broadening (narrowing) of a resonance for a forward (backward) scan. Figure 6.2a shows a WGM resonance scanned with a fast sweep velocity ($9.8\,\mathrm{nm/s}$). When we reduced the scan velocity to $98\,\mathrm{pm/s}$, the measurement of the same resonance shows a narrowing of its shape for a backward sweeping, see Fig. 6.2b, and a broadening for a forward sweeping, depicted in Fig. 6.2c.

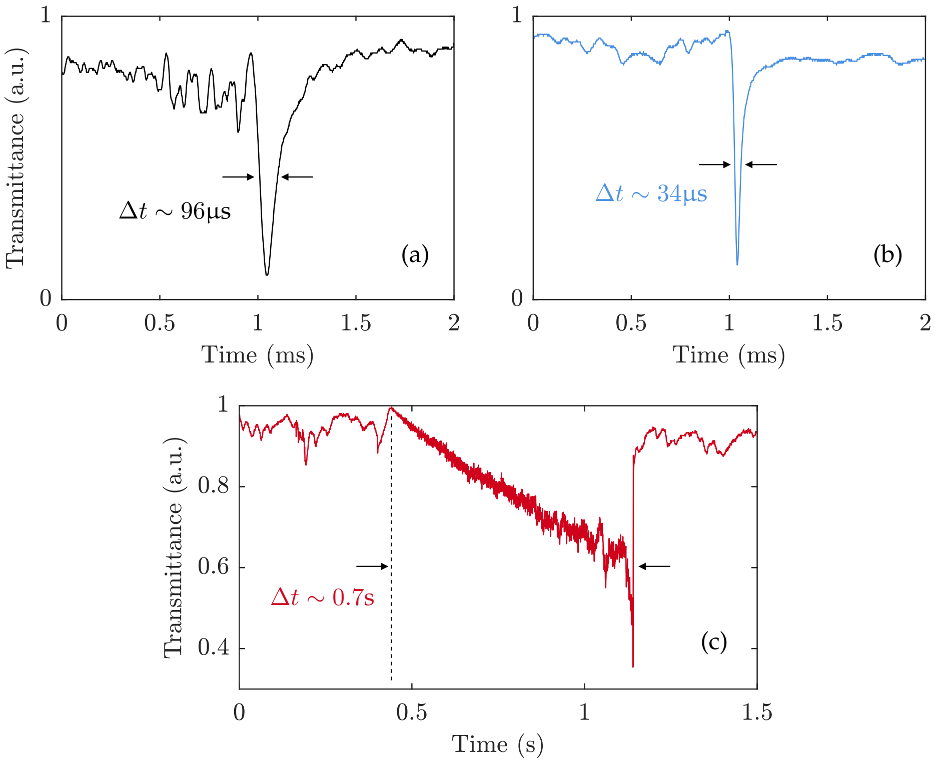

Figure 6.2: (a) WGM spectrum for a fast laser scan. Nonlinear thermal effects: (b) narrowing of the resonance for a backward scan, and (c) broadening for a forward scan.

As a consequence of the nonlinear thermal effects, then, it is not obvious that the laser wavelength is permanently tuned at the center of the WGM resonance. This results in a variable quantity of power coupled to the MR, depending on the parameters at which the laser performance is set (sweep velocity and optical power), and the characteristics of the MR (thermo-optic coefficients, Q-factor, *etc*). However, for most applications that involve optical nonlinear effects in MR, it is necessary an operational regime in which the coupled input power is stable. In some other applications, it is also needed a stable pump wavelength. To achieve a proper matching of the laser wavelength to the WGM resonance, different techniques can be implemented with the objective of stabilizing the input power coupled to the MR. These stabilization techniques are usually called locking techniques, and can be distinguished in two major categories: passive-locking, and active-locking techniques.

In passive locking techniques, the nonlinear thermal effect described above is exploited to quasi-stabilize the energy coupled to the MR. The idea of the locking process consists on tuning the laser pump to a shorter wavelength than the WGM resonance, and scan toward longer wavelengths with a sweeping velocity comparable to the self-induced thermal shift of the resonance (the scenario illustrated in Fig. 6.1a). If the laser sweeping is stopped during the scan, a meta-stable warm-equilibrium is achieved (the small detuning between the laser wavelength and the WGM wavelength remains constant). This equilibrium can overcome small perturbations of the WGM resonance wavelength that may be induced by external instabilities such as vibrations. Figure 6.3a illustrates this situation, when a small perturbation shifts the resonance toward longer wavelengths and the laser is centered at a wavelength on the blue side of the resonance (this is, within the width of the resonance, slightly shifted to its left). When that happens, the temperature of the MR decreases, since the coupled power is reduced (this is, $\mathrm{Tr}_{\mathrm{per}} > \mathrm{Tr}_{\mathrm{eq}}$). Thus, the resonant wavelength drifts again to the meta-stable equilibrium. In the opposite scenario in which the perturbation shifts the resonance toward shorter wavelengths, the inverse process occurs, which is depicted in Fig. 6.3b: the MR increases its temperature (since $\mathrm{Tr}_{\mathrm{per}} < \mathrm{Tr}_{\mathrm{eq}}$), and the WGM resonance shifts thermally back to the meta-stable equilibrium [10]. The maximum amplitude of the self compensated perturbations are given by the distance in wavelength between the laser and the minimum transmission point of the WGM resonance, see Fig. 6.3c. However, despite this ability to compensate noise sources, the passive locking can not overcome slow and continuous drifts of the resonances, thus, other techniques must be implemented.

On the other hand, in some applications, instead of stopping the laser during the sweeping, the WGM resonance is continuously and repetitively scanned [12]. Since the response times of the optical nonlinear effects are much faster than the typical time response of thermal effects, the coupling power during the sweeping is averaged, and it is possible to observe the nonlinear phenomena. By employing this configuration the coupled power and the wavelength are not constant. However, since the operational wavelength varies in a given range, it may be easier to achieve the phase matching condition required for the nonlinear effects. The laser sweep velocity for this kind of experiments depends on the input coupled power: for higher powers, faster laser sweep velocities are needed.

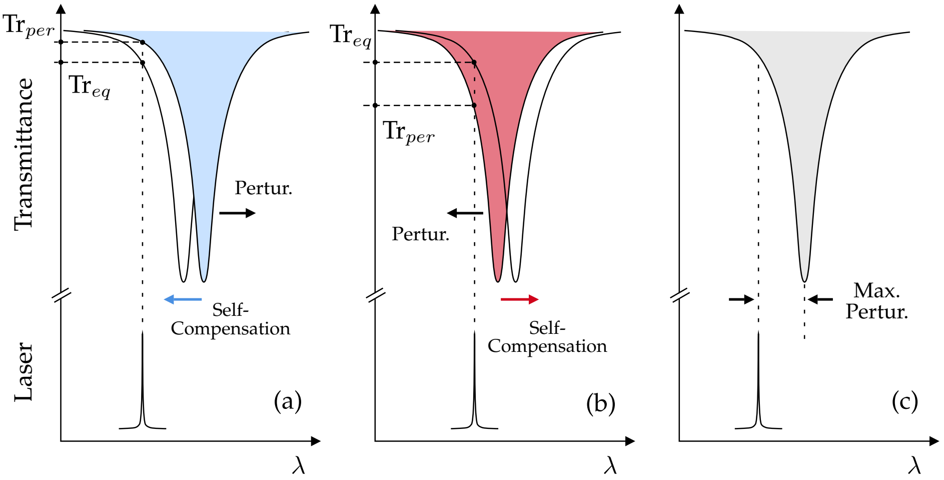

Figure 6.3: Self-compensation in the meta-stable equilibrium for: (a) cooling perturbation, and (b) heating perturbation. (c) Self-compensated maximum perturbation amplitude.

In active locking techniques, a feedback control system is used to stabilize the energy coupled to the MR for an unlimited time. The techniques can be classified depending on the feedback parameter. For locking WGM resonances, in most of the applications the feedback parameter is the resonant wavelength, or the power coupled to the MR (the transmittance of the resonance) [13]. When the wavelength is the locking parameter, the Pound-Drever-Hall method [14] is used to correct the deviation between the laser wavelength and the WGM resonance. In this method, the phase of the WGM resonance is modulated and used to control the feedback loop. As an alternative, in the active locking techniques that we will present in the following sections, we will employ the average transmission level as the feedback parameter of the active locking technique.

Then, the transmittance of the system (which is complementary to the fraction of input power coupled to the MR), is the parameter used to control the feedback loop. Experimentally, the transmittance of the system is measured by a photodiode, and the corresponding voltage is the input signal for the electronic feedback device. Figure 6.4 shows a scheme of the system employed for the locking. The input voltage, V_{in}, proportional to the transmittance, is filtered by a low-pass filter which, in our case, attenuates all the frequencies above 1.5 kHz. The locking system is designed to compensate low frequency variations such as room temperature variations, which are the main source of perturbations, and produce slow thermal drifts below this cutoff frequency. These slow variations of the transmittance are compensated perfectly even when the higher frequency perturbations (which may be caused by a sudden blow in the setup, for example) are not corrected. In addition, the locking system must allow fast frequency phenomena to occur: for example, as we will show later in this chapter, the optomechanic effects show typical frequencies in the range from hundred of kHz to MHz, and it is crucial that the locking device does not compensate this range of frequencies.

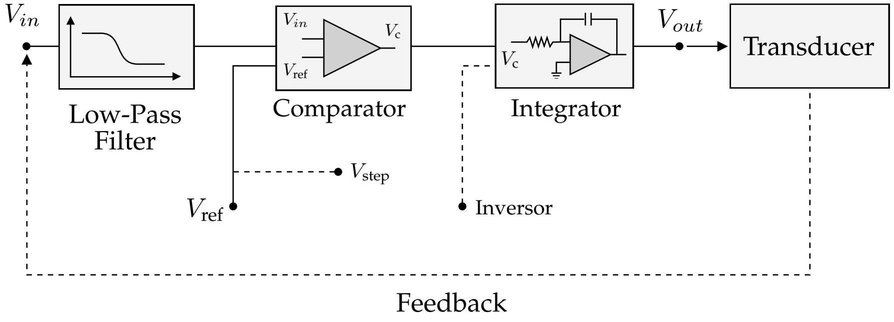

Figure 6.4: Scheme of the electronic feedback operational device. Feedback parameter: transmittance of the system, V_{in}.

In a second stage, the filtered signal is compared with a reference one, V_{ref}. This value is adjusted to one of our choice, to match the laser wavelength to a point of the resonance of a chosen transmittance. In this way, we set the operational transmittance of the system (or coupled energy to the MR). In our device, this reference signal can be modified manually with a step function, V_{step}, that will allow us studying the time response of our locking technique. The value of the comparator output signal, V_c, indicates how different is the input signal compared to the reference one. Finally, the integrator generates an output signal (proportional to the integral of V_c), V_{out}, which is applied to a transducer. This transducer modifies the conditions of the optical system (λ of the laser, for example) in order to reduce the value of V_c, this is, to set the operational transmittance back to the reference value that we chose initially by means of V_{ref}: now, the system is locked. Thus, when a low frequency variation perturbs our MR, leading to an undesired detuning between the laser wavelength and the spectral position of the resonance, the electronic system reacts introducing a variation in the optical conditions that corrects that detuning, for example by slightly shifting the laser wavelength to a new spectral position.

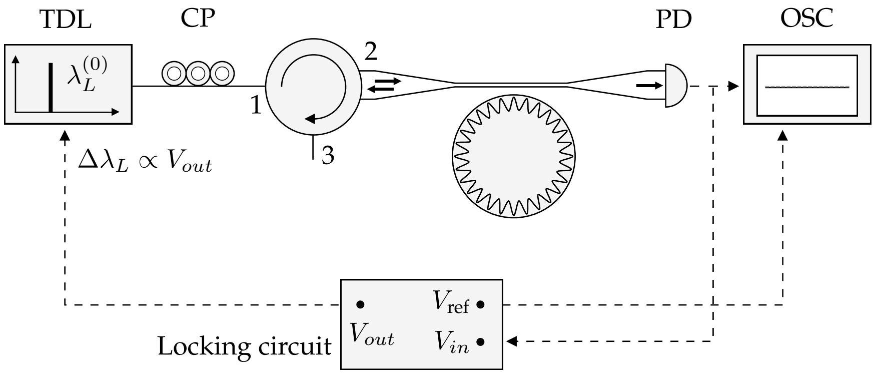

Figure 6.5: Scheme of the setup employed to lock WGM resonances by adjusting the operational wavelength of the TDL.

We employed our feedback device to lock WGM resonances actively. To achieve the stabilization in this first experiment, we adjusted the wavelength of a TDL. Fig. 6.5 shows a scheme of the setup. The transmittance of the system is monitored on an oscilloscope. The same signal of the photodiode is used as the input for the feedback device, V_{in}. We can manually modify the reference signal, V_{ref}, and adjust its level, to one within the maximum and minimum values of the transmittance of the resonance. However, in practical conditions, this value must not be chosen too close to the upper or lower limits of the transmittance. The locking system will produce an output voltage, V_{out}, which will change the laser wavelength when is needed. This process results in the correction of thermal nonlinearities, which, as we mentioned before, is the main effect we want to overcome, and some other external perturbations. When the system is locked, the energy coupled to the MR is fixed to a constant value, which is set by the reference level.

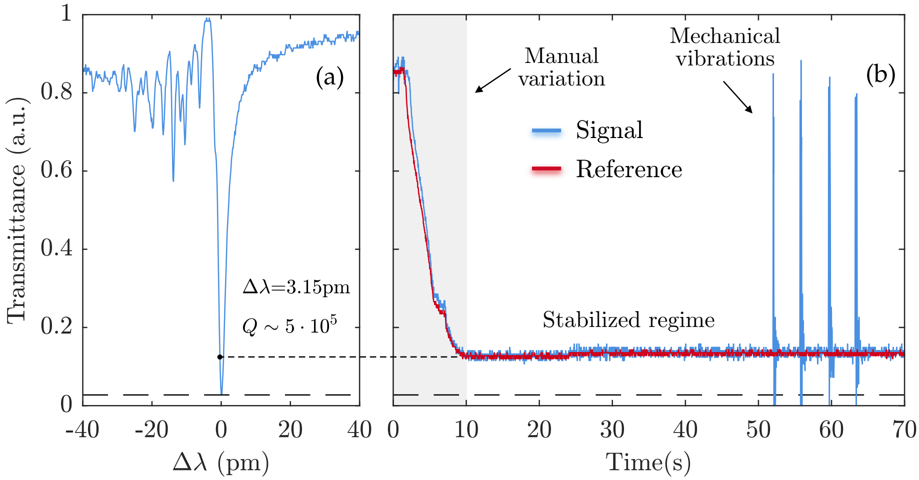

Figure 6.6: (a) WGM resonance of a cylindrical, silica MR of 124 μm diameter. (b) Locking at different transmittance levels, and temporal stability.

By employing this setup, we locked a WGM resonance of a cylindrical, silica MR of 124 μm of diameter, see Fig. 6.6a. The output power of the TDL was fixed to 10 mW for these measurements. Figure 6.6b shows the change of the transmittance (output signal) according to the reference level that we vary manually by means of our feedback device. In the first 10 seconds, we manually modified the reference level to show the resulting variation in the output signal. As we change the V_{ref}, the locking system shifts the wavelength of the TDL, and it takes it closer to a spectral position that shows a lower transmittance. In this way, as it can be observed, we can establish the operational transmittance of the system, and therefore, the desired energy coupled to the MR. With this technique, we can not lock the WGM resonance at its minimum transmittance, since the electrical device requires a variation of voltage with a non null slope. By contrast, we can stabilize the system at any point of its both sides. From second 10 to 70, it can be observed the stability in time of the technique. The locking device corrects and compensates the external perturbations such as thermal fluctuations of the room temperature, or small vibrations. We studied the stability of the locked system for more than 3 hours, and the same level of transmittance that the one shown in Fig. 6.6b was observed during the whole time.

The maximum perturbation that the locking system can correct depends on the transducer used to set the system back to the reference conditions. When the locking is applied to the laser, the technique is limited to its wavelength tuning range. This is the most common approach to this problem. Here we will present some alternatives that do not work based on changing the laser wavelength, but the MR properties. In this way, we can perform experiments at constant wavelength and the requirements on the laser (that are usually expensive devices) are reduced. We will show techniques based on the thermo-optic and strain-optic effects. The maximum perturbation the locking device can correct will depend, then, on the magnitude of such effects in our MR.

We also studied the laser locking using a spherical, silica MR (which usually show larger Q-factors), and we observed the same behavior reported in Fig. 6.6. Therefore, we can conclude that our feedback device allows us locking WGM resonances in different MRs, enabling the stabilization of the laser wavelength at any point of the resonance edge. This will allow us improving and controlling the generation and observation of optical nonlinear effects in such MRs, as we will show in the following sections.

6.2 Active locking at constant wavelength

The locking technique described in the above section stabilizes the transmittance of the system by adjusting the wavelength of the laser. The thermal nonlinearities and the external perturbations, which shift the resonant wavelength of the WGM resonances from its original position, are compensated and corrected by changing the operational wavelength of the laser. In applications where the control of the power coupled to the MR is a crucial parameter, this laser-locking technique can be implemented to achieve the stabilization [15, 16]. However, in some applications an operational regime with a constant wavelength is also needed. This occurs, for example, when nonlinear effects that require a phase-matching condition are involved. These two conditions, constant coupled power and constant laser wavelength, are usually fulfilled by employing a self-thermally passive locking [4]. Here, we will present two alternative active locking techniques that allow operating at constant wavelength and present some additional advantages. The idea of both proposals is to compensate and correct the thermal drift and the perturbation of the WGM resonance, by inducing a variation of the parameters of the MR that set the WGM resonant wavelength. This variation will be induced by means of a mechanical deformation, or a temperature increment of the MR.

(I). Strain locking

The first technique is based on the strain-optic effect described in Chapter 4. When a cylindrical MR is axially stretched, their WGM resonances shift toward shorter wavelengths as we already described. With this is mind, we designed a locking setup to stabilize the transmittance of the system by employing the feedback device described in the previous section. Figure 6.7 shows a schematic of the experimental setup employed to lock the WGM resonances by means of strain. The configuration is very similar to the one described in Fig. 6.5, but in this case, the MR is attached to a piezo-electric (transducer) that is driven by the electric feedback signal. Thus, the piezo-electric induces an axial stretch in the MR that is proportional to the undesired detuning of the WGM resonant wavelength with respect to its original position. This axial stretch compensates the thermal nonlinearities, and by decreasing or increasing the strain, the external perturbations can be corrected as well. By employing this configuration, the laser wavelength remains constant. This method opens the possibility of using a laser that does not present a fine-tuning wavelength system.

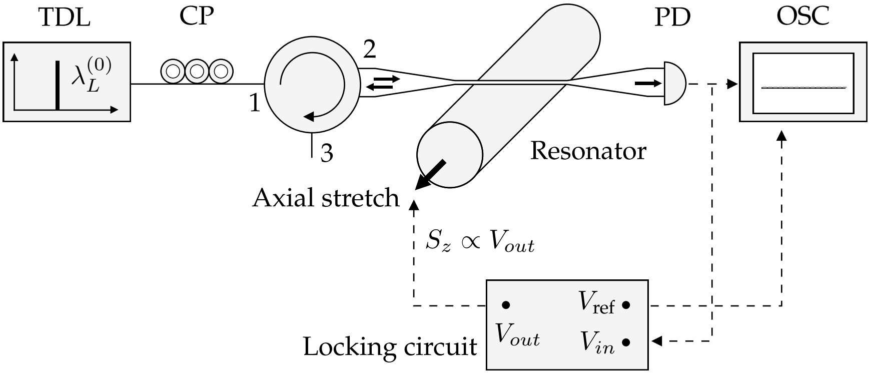

Figure 6.7: Scheme of the setup employed to lock WGM resonances, based on the strain-optic effect.

An analogous strain-based method has been reported in the past to lock spherical shaped cavities [17]. Thus, even when our setup has been designed for cylindrical MRs, it can be modified in order to adapt the stretching elements to other geometries of the MR.

To characterize the performance of the strain-locking technique, we measured the response of the system to two types of applied perturbations: (i) a step variation of the operational locked transmittance (reference level), and (ii) a harmonic variation of the laser wavelength.

(i) **Step variation:** Our feedback device was designed to allow us to modify the reference signal with a step function. In practice, when the system varies the V_{ref} value from a locked position, it induces a change in the parameters that set the resonant wavelength of the WGM (in this case, an offset strain). This produces a re-stabilization process of the WGM resonance that sets the transmittance of the system to a different level. Figure 6.8a shows a WGM resonance of a cylindrical, silica MR of 124 µm diameter. Figure 6.8b shows the time response of the locking system to a step variation of the transmittance of $\sim 26\%$. Initially the transmittance was set at a point A ($t < 0$ at Fig. 6.8). Then, a step function was applied to V_{ref}, and the operational point was set to B, at a lower transmittance ($t = 0$ at Fig. 6.8). By analogy to electronics, we will describe the response by measuring the fall time and the settling time of the locking system. The fall time is the time taken by the signal to change from the 90% to the 10% of the transmittance variation. For this example, it takes ~ 20.7 ms. The settling time is the time elapsed by the system to stabilize the signal within an error of 5%. In this case, ~ 0.65 s. A fast response of the locking device to a step change of the operational point means the possibility of varying the V_{ref}, and therefore, reconfiguring the long term steady state in a faster time. Certainly, the electronic circuit of the feedback can be designed to modify substantially these values.

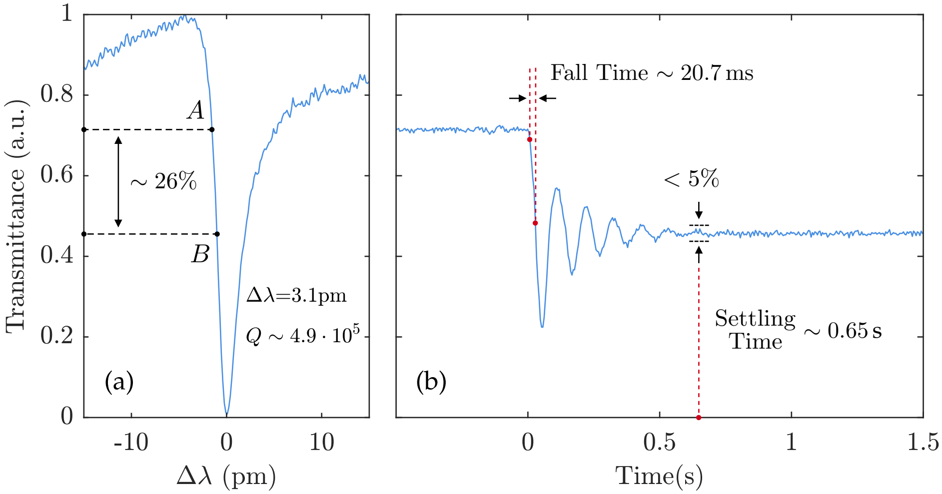

Figure 6.8: (a) WGM resonance of a cylindrical, silica MR of 124 µm of diameter. (b) Time response of the locking-strain system to a step variation of the operational transmittance.

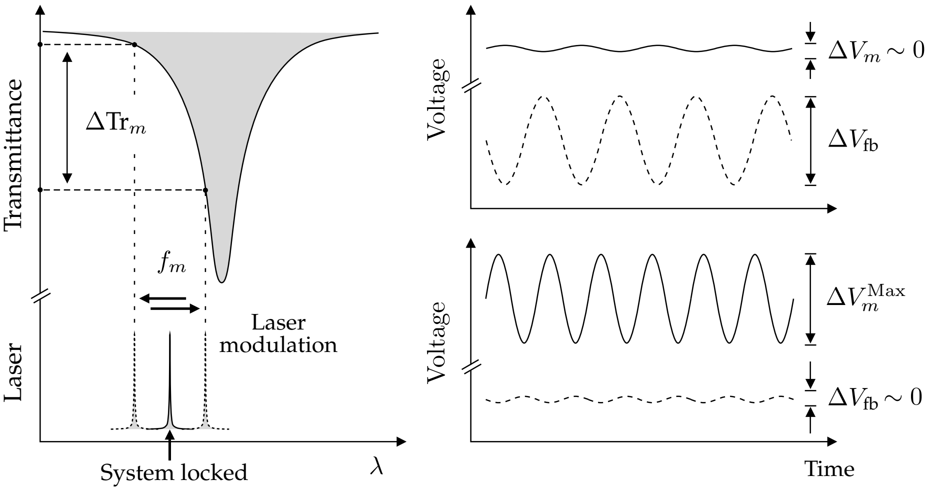

Figure 6.9: Illustration of the locking-strain system response to a harmonic modulation of the laser wavelength after the system was pre-stabilized. Two examples: $f_m < f_{\text{cutoff}}$ (upper), and $f_m > f_{\text{cutoff}}$ (lower).

(ii) **Harmonic perturbation:** The second measurement we performed was to study the response to another type of perturbation, a harmonic variation of the laser wavelength around the initially locked spectral position. After the system is locked to an operational point, we introduced a harmonic sweep in the laser wavelength. In this way, we introduced a controlled perturbation that allowed us focusing on the time response of the system, independently of other external fluctuations. The amplitude of this modulation was constant during all the experiment, and it was set to $\Delta\lambda_L = 0.5\,\text{pm}$ (which corresponds to a $\sim 24\%$ of transmittance variation). The frequency of modulation was changed to study the response of the locking system. Due to the wavelength sweeping of the laser, the system experiences a modulation of the transmittance, ΔTr_m, that can be measured by the oscilloscope as a variation of the signal voltage, ΔV_{m}. This means that the locking system is changing continuously the strain applied to the MR, within a given range set by the amplitude of the wavelength sweep. This is, the feedback device tries to stabilize continuously the system, by sending a feedback signal, ΔV_{fb}, to the piezoelectric, in order to correct the effects induced by the laser wavelength sweeping. Figure 6.9 shows an illustration of the process described above. The optimum operational regime of the locking device will be achieved when the transmittance remains constant, since this means the system is able to correct the perturbation we are applying.

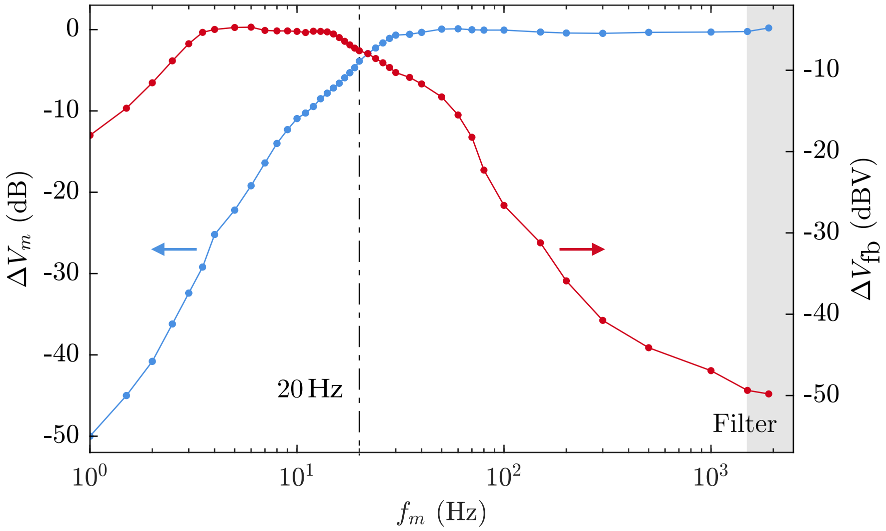

Figure 6.10: Measurement of the response of the strain-locking system to a harmonic modulation of the laser wavelength, as a function of the frequency of modulation.

Figure 6.10 shows the variation of the transmittance device (this is, the amplitude of ΔV_m) normalized to that one measured when the feedback signal was not applied to correct the laser wavelength sweep (ΔV_m^{Max}), this is, $\Delta V_m/\Delta V_m^{\text{Max}}$, as a function of the laser sweeping frequency. When there is no perturbation applied to the system (the system is locked at a working point and there is not a laser sweeping), the value for ΔV_m is zero and there is no need of feedback. As we mentioned before, once we apply a perturbation to the system in the form of a laser wavelength sweeping, the feedback device reacts trying to compensate this perturbation. In this case, it will send a signal to the transducer, depicted in Fig. 6.10 as ΔV_{fb}. At low frequencies, the locking system is fast enough to correct the perturbation induced by the laser system, thus ΔV_m is near zero (this is, we observe a constant value of the transmittance). As f_m increases, we can observe that the value of ΔV_m increases. This means that the feedback system is not able to provide enough feedback signal, ΔV_{fb}, to correct the perturbation. This decrease of ΔV_{fb} with the frequency is depicted in Fig. 6.10. There are two key factors that limit the ability of our setup to correct fast perturbations: the lowpass filter of the electronic setup, which prevents the locking at high frequencies ($f_m > 1.5\,\mathrm{kHz}$), and the time response of the piezo-electric that applies the strain to the MR. For our setup, the variation of the ΔV_m, and therefore of the transmittance variation, was kept under $3\,\mathrm{dB}$ for frequencies below $20\,\mathrm{Hz}$.

(II). Pump locking

The second proposal we present is based on the thermo-optic effect described in Chapter 5. When the temperature of a silica MR increases (decreases), their WGM resonances shift toward longer (shorter) wavelengths. By taking advantage of this phenomenon, we designed a locking setup to stabilize the transmittance of the system at a chosen value. The feedback system is the same as the one described previously, but instead of using a transducer which varies the strain of the MR, we implemented a device that controls the temperature of the MR. This variation of the temperature is achieved by pumping the core of the MR which is formed by an active, doped fiber. The maximum heating achieved depends on the power of the pump signal, and on the absorption of the core dopant at the pump wavelength. Figure 6.11 shows a scheme of the experimental setup employed to lock the resonances by a pump-induced heating. It is worth to note that, even when in the scheme we depicted a cylindrical MR, in practice, a configuration with a spherical one fabricated using a doped silica glass can be easily implemented. In our proposal, the feedback signal controls the power of an auxiliary laser pump source, whose signal is launched to the core of a fiber (for cylindrical MRs, the fiber itself plays the role of the MR, and for spherical ones, the sphere is fabricated at one of its ends). To set the operational point, the pump power is set to a given value to pre-heat the MR. Then, when a perturbation affects the locking, the system varies the pump power to correct such perturbation. In the case of thermal nonlinearities, the system will decrease the pump power, this is, it will cool the MR, to compensate the red shift of the WGM resonance. As in the other technique, the laser wavelength will remain constant during all the process.

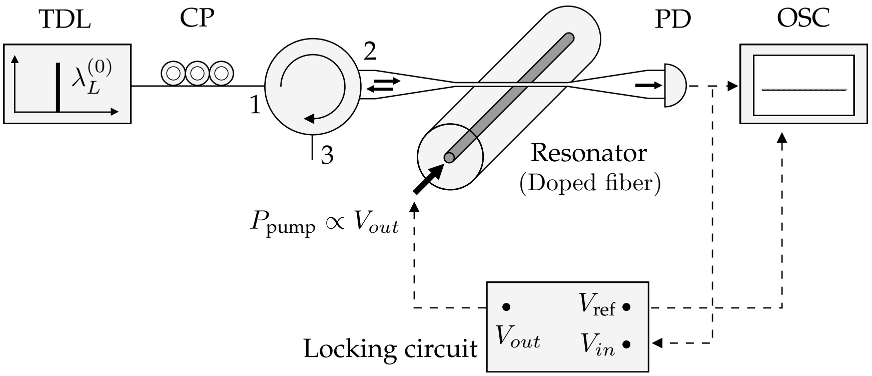

Figure 6.11: Scheme of the setup employed to lock WGM resonances by means of the thermo-optic effect.

Up to our knowledge, this is the first time that an all-optical locking technique, based on the control of the temperature of the MR using an auxiliary pump signal, is proposed to stabilize the operational transmittance of the WGMs.

To characterize the performance of the pump-locking technique as in the previous case, we measured the response of the system to a step variation, and to a harmonic modulation of the laser wavelength. For these measurements, the cylindrical MR consisted on a section of a Fibercore DF1500Y (Er/Yb co-doped fiber). The thermal behavior of this fiber was characterized in [18]. The pump source was a single-mode laser at 975 nm (maximum output power: 400 mW).

(i) **Step variation:** Figure 6.12a shows a resonance of a MR of 125 µm of diameter fabricated with the DF1500Y fiber. Figure 6.12b shows the time response of the locking system to a step variation of the transmittance of $\sim 33\%$. The description of the response is analogous to the one detailed for the strain-locking method, but for a different transducer that controls the temperature. The fall time in this case was $\sim 7.6\,\mathrm{ms}$, around 2.7 times faster than our strain-locking technique. The settling time was $\sim 0.28\,\mathrm{s}$, therefore, our pump-locking technique is ~ 2.3 times faster than the one based on the strain. This can be due to a faster response of the transducer.

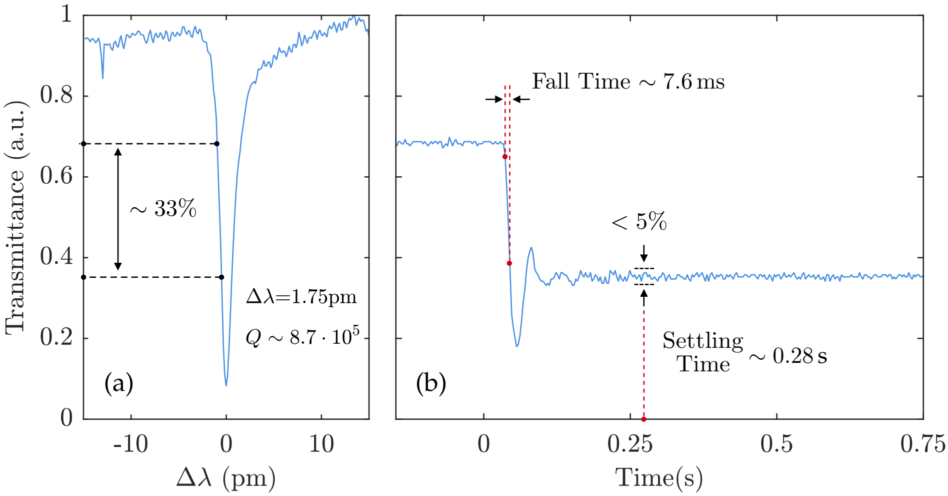

Figure 6.12: (a) WGM resonance of a cylindrical, silica MR (DF1500Y) of 125 µm of diameter. (b) Time response of the locking-pump system to a step variation of the operational transmittance.

(ii) **Harmonic perturbation:** Figure 6.13 shows the variation of the transmittance device and the amplitude of the feedback signal, analogously to Fig. 6.10. The behavior observed was very similar to the one reported for the strain-locking technique. At low frequencies, the locking system can correct the perturbation induced by the laser system, thus the transmittance remained constant. As f_m increases, the feedback system is not able to correct the perturbation. For our setup of the pump-locking, the transmittance variation was kept below 3 dB for frequencies below 200 Hz. Thus, although this alternative limits the variety of MRs to those that are doped with the proper elements, it provides a better performance than the strain-locking technique.

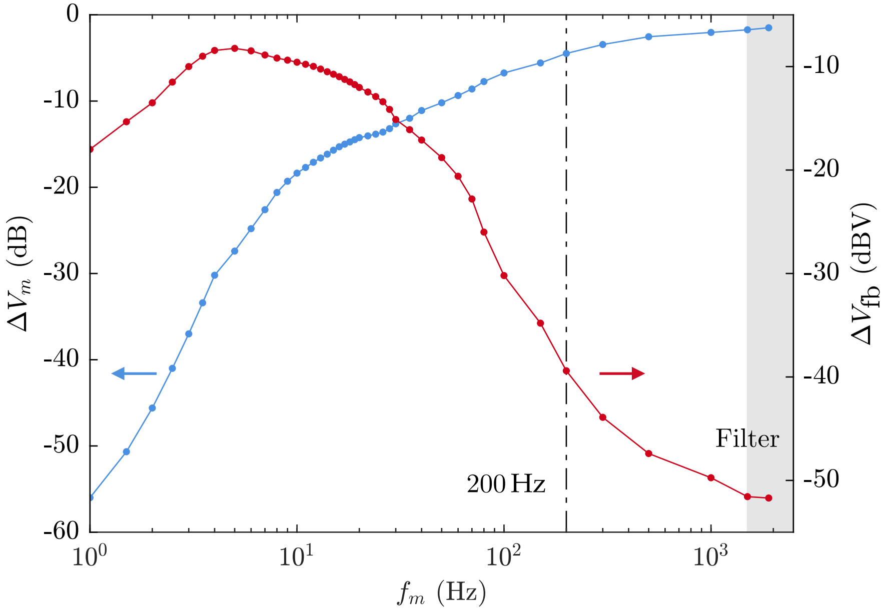

Figure 6.13: Measurement of the response of the pump-locking system to a harmonic modulation of the laser wavelength, as a function of the frequency of modulation.

6.3 Optical nonlinear phenomena

In this section, we will present different nonlinear phenomena observed in spherical, silica MRs. A detailed description of the different effects is beyond the scope of this work, and we will focus our experiments on the enhancement of the generation and stabilization of different nonlinear effects, by employing the pump-locking technique that we described in the previous section.

Among the several nonlinear effects that can be excited in silica MRs by means of WGM resonances [19], we will focus on three, which are third-order nonlinear processes: Stimulated Raman scattering (SRS), Four-wave mixing (FWM), and Stimulated Brillouin scattering (SBS) [20]. Figure 6.14 shows an illustration of the different phenomena. As an overview, we will provide a brief description of the nonlinear effects:

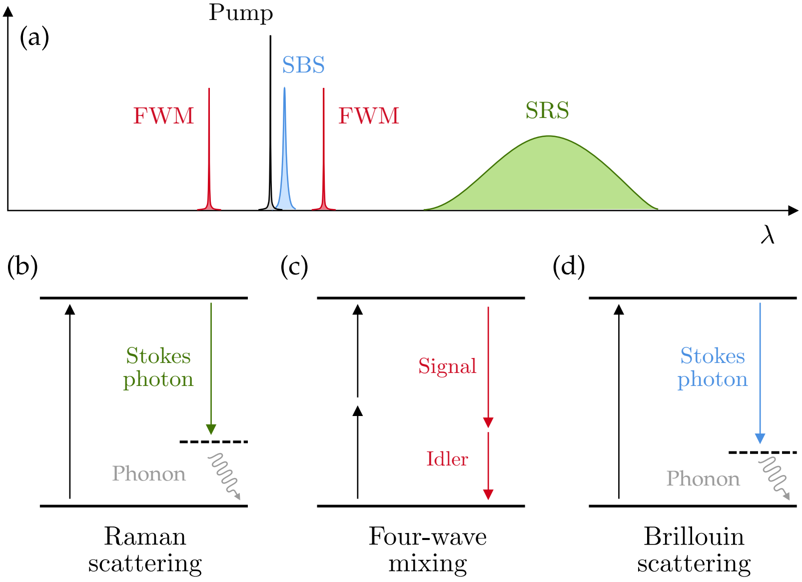

Figure 6.14: (a) Illustration of the spectra observed when nonlinear phenomena are generated. Schematics of the different physical processes: (b) Stimulated Raman scattering, (c) Four-wave mixing, and (d) Stimulated Brillouin scattering.

(i) In SRS, one pump photon is converted into one Stokes photon and an optical phonon, by means of an inelastic scattering process, see Fig. 6.14b. The interaction of the photons with the phonons is attributed to the molecular vibration of the material. Since there is an exchange of energy and momentum between the optical field and the MR material, SRS is a non-parametric process. Due to the broad Raman gain bandwidth of the silica, and the large number of modes with small FSR in spherical MRs, multi-mode Raman lasing is usually observed in these type of MRs, and we will show later an example.

(ii) In FWM, two degenerate pump photons generate one idler and one signal photon, see Fig. 6.14c. The idler (signal) photon has higher (lower) wavelength than the pump. In this case, it is a parametric process, since there is no transfer of energy to the material.

(iii) SBS is similar to SRS, one pump photon is converted into one Stokes photon and an acoustic phonon, by means of an inelastic process, see Fig. 6.14d. In this case the light is scattered by acoustic waves within the material, resulting in a non-parametric process. The Brillouin gain bandwidth is narrower than the SRS one, in silica.

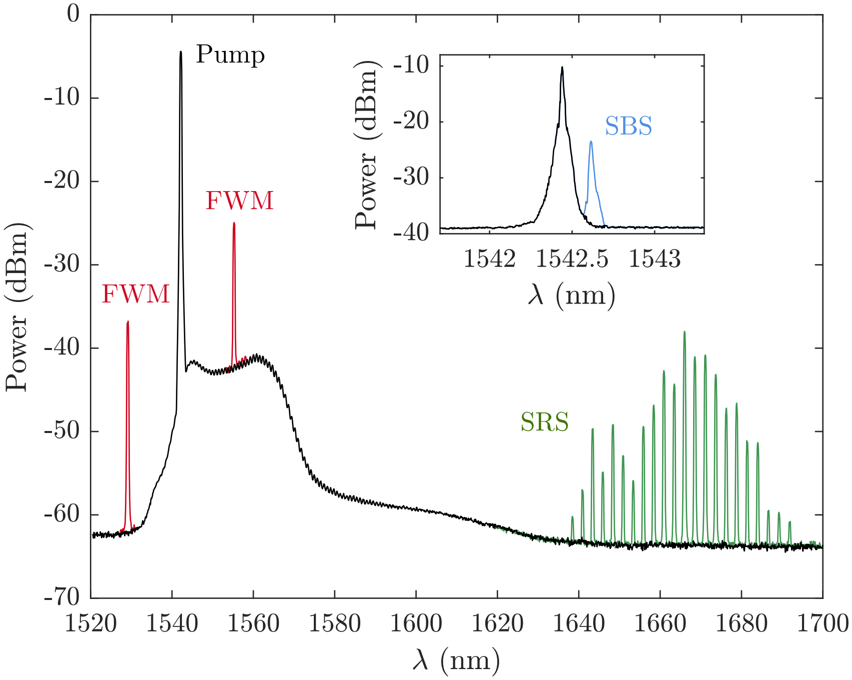

Figure 6.15: Spectra of different optical nonlinear effects in a spherical, silica MR of 239.5 µm diameter.

For our experiments, we fabricated a spherical MR from a DF1500Y fiber. We chose to use a spherical MR because of the higher Q-factor of the WGM resonances and the smaller mode volumes, when compared to cylindrical MRs. The diameter of the sphere was 239.5 µm, and the WGMs were excited by placing the taper at the equator of the MR. In the setup, the tunable laser source ($<$ 300 KHz linewidth) was amplified with an Er/Yb amplifier. For the measurements, the power of the laser signal launched to the MR was set to 100 mW. The stabilization of the WGM resonances was achieved by employing two techniques: the thermal passive method, and our active locking technique based on the thermo-optic effect. Although in both cases we observed the same nonlinear phenomena, when the resonances were stabilized by means of the active technique, the nonlinear effects were more stable, as we will show. Figure 6.15 shows a compilation of the different effects observed. They correspond to different measurements in which we locked different WGM resonances, at different operational transmittance levels. In some cases, more than one effect was observed simultaneously.

In most works, the nonlinear effects are excited and observed using a passive locking technique since it is easy to set up experimentally. Here, we propose to use an active locking techniques since it improves the performance of the nonlinear effects. Apart from the advantages that we described in the previous sections, we will show some additional improvements that presents an active locking:

(i) First, by using an active locking technique, we can choose which WGM resonance is stabilized. This means that the technique provides control on the radial, azimuthal and polar order of the different resonances that a MR exhibits (this is, we can select, within some limits, the optical field distribution of the WGMs, which can help to optimize certain nonlinear effects).

(ii) Active techniques also provide control on the value of the operational transmittance of the system. This is one of the most important features of this kind of locking. By changing the transmittance level (which was controlled by means of the reference signal, see Fig. 6.6), we modify the energy coupled into the MR. This leads to different circulating powers that can exceed or not the thresholds of the different nonlinear effects. Figure 6.16 shows an experimental measurement where by changing the transmittance of the system we could *(de)excite* SRS depending on the power coupled to the MR. As a consequence, in the case of two competitive nonlinear effects, we can suppress the one with the higher threshold and enhance the other one just by controlling the transmittance level. This accurate and stable selection of competitive effects with different thresholds is not possible with a passive locking technique.

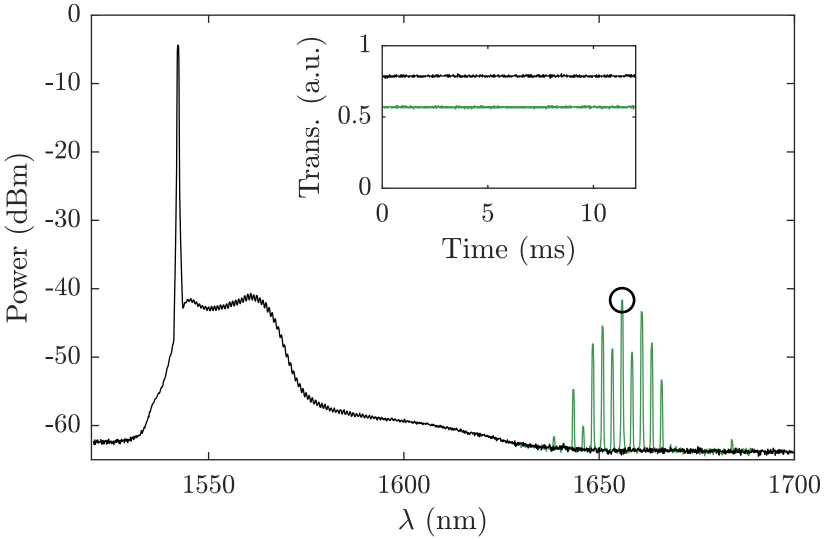

Figure 6.16: *(De)Excitation* of SRS depending on the INSET: transmittance of the resonance set at two different levels (power coupled to the MR).

(iii) Moreover, when the transmittance level is changed, the detuning between the laser and the WGM resonance is also modified. In nonlinear applications where there exists a strict phase-matching condition [21], the control of this detuning is crucial in order to excite the nonlinear phenomena. In the case of conventional active locking techniques, when the feedback consists on a variation of the laser wavelength, this is still a problem. It is worth noting, then, that our technique provides a better alternative to lock the resonance at very specific wavelengths. We should mention that in the example shown in Fig. 6.16, the *(de)excitation* of the SRS is not affected by the phase-matching condition, it is only due to the different circulating powers, since the Raman scattering does not depend on the detuning due to its broad gain in silica [1].

We studied the temporal stability of the nonlinear effects when an active pump-locking is implemented, against the passive locking technique, for one of the phenomena we could observe in our MR. Figure 6.17 shows the stability of the Raman lasing peak (circled in Fig. 6.16), for an active and a passive locking. In both cases we locked the same resonance at the same transmittance level. As it can be observed, when the system is actively locked, the power variation of the Raman peak varies less than 1 dB. Meanwhile, when it is passively locked, the power changes more than 10 dB, after a short time. It is worth to point out that, the power variations of the Raman peak are not due to the loss of the locking, since during the time of the measurement, we did not observe a significant variation of the transmittance level of the resonance (this is, the power coupled to the MR was kept as a constant).

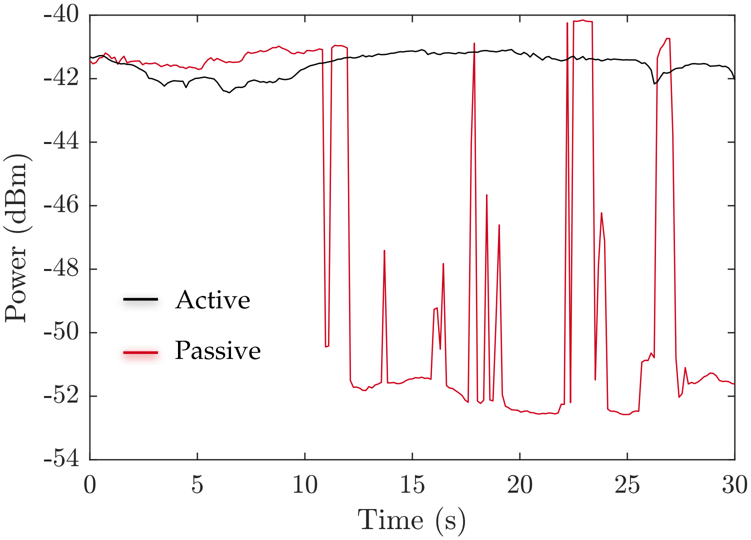

Figure 6.17: Temporal stability of a Raman lasing peak for an active and passive locking.

Therefore, we can conclude that the active pump-locking technique we propose here provides a number of advantages when it is applied to the generation of nonlinear phenomena: better stability of the nonlinear effects, capability of selection between competitive nonlinear phenomena with different thresholds, and accurate, fixed selection of the laser wavelength in order to excite efficiently the nonlinearities with a strict phase-matching condition.

6.4 Optomechanic effects

(I). Introduction

As we described throughout this chapter, when a continuous wave (dc) laser is tuned to a spectral position close to the resonant wavelength of a WGM, and in addition, it is locked to the resonance, a huge circulating power is confined in the MR. This circulating light intensity induces a mechanical flex of the cavity due to the radiation pressure (RP). As a consequence of the mechanical deformation of the MR, the optical path length that the WGM travels varies. Thus, the resonant wavelength of the WGM resonance shifts, which results in a detuning between the laser wavelength and the WGM resonance and, therefore, in a change of the system transmittance (this is, the circulating power). Consequently, the intensity of the RP will change. This feedback mechanism is the so-called optomechanical back-action [22]. The retardation between the mechanical deformations and the resulting RP variation, leads to optomechanical parametric instabilities that produce self-induced oscillations at some frequencies that correspond to those of the mechanical modes supported by the MR; this is, a periodic vibration of the cavity is induced [23].

Figure 6.18 shows an illustration of the self induced back-action RP oscillation. The optomechanical vibration will lead to a periodic modulation in the transmittance, which results in the generation of two side-band peaks that will appear at a frequency distance Ω_m from the laser frequency, ω_L. The blue-shifted peak, with frequency $\omega_{aS} = \omega_L + \Omega_m$ is usually referred as anti-Stokes peak, and the red-shifted, $\omega_S = \omega_L - \Omega_m$, as Stokes peak. Since the WGM resonances have a Lorentzian profile, both peaks are not equal in magnitude, and depending on the sign of the detuning between the laser and the resonant wavelength of the WGM, only one of them will be amplified. From this asymmetry, two effects directly arise: *cooling* or *amplification* of the mechanical mode. Figure 6.19 shows an illustration of both situations.

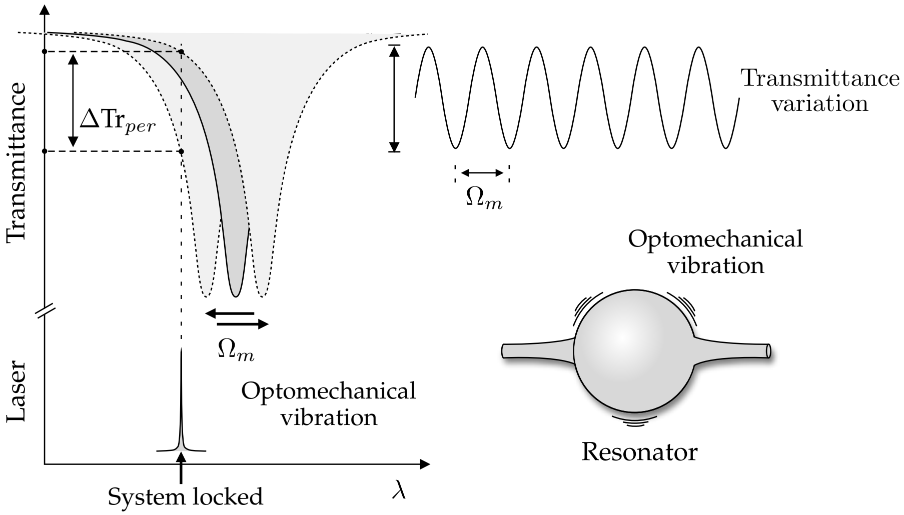

Figure 6.18: Illustration of transmittance variation (i.e., RP variation) induced due to the optomechanical vibration (Ω_m frequency of vibration).

(i) When the laser is red-detuned with respect to the resonance wavelength, $\omega_L < \omega_R$, the number of generated anti-Stokes photons is higher than the Stokes one, which implies an increment of the energy of the optical mode at expenses of the mechanical energy, see Fig. 6.19a. This transference of energy from the mechanical mode to the optical one is called *cooling*, since the result is that the mechanical mode is attenuated.

(ii) On the other hand, when the laser is blue-detuned, $\omega_L > \omega_R$, the generation of Stokes photons is dominant, and the optical mode suffers a decrease of its energy. Therefore, there is a power flow from the optical field to the mechanical mode, leading to an *amplification* of the vibration, this situation is depicted in Fig. 6.19b.

In this work, we will study the amplification of the optomechanical vibrations (laser blue-detuned case), since it is in this configuration when regenerative oscillations are observed. In these experiments, WGMs will be excited with a dc laser with pump intensities above the threshold power, this is, when the amplification of the mechanical mode exceeds its losses [23].

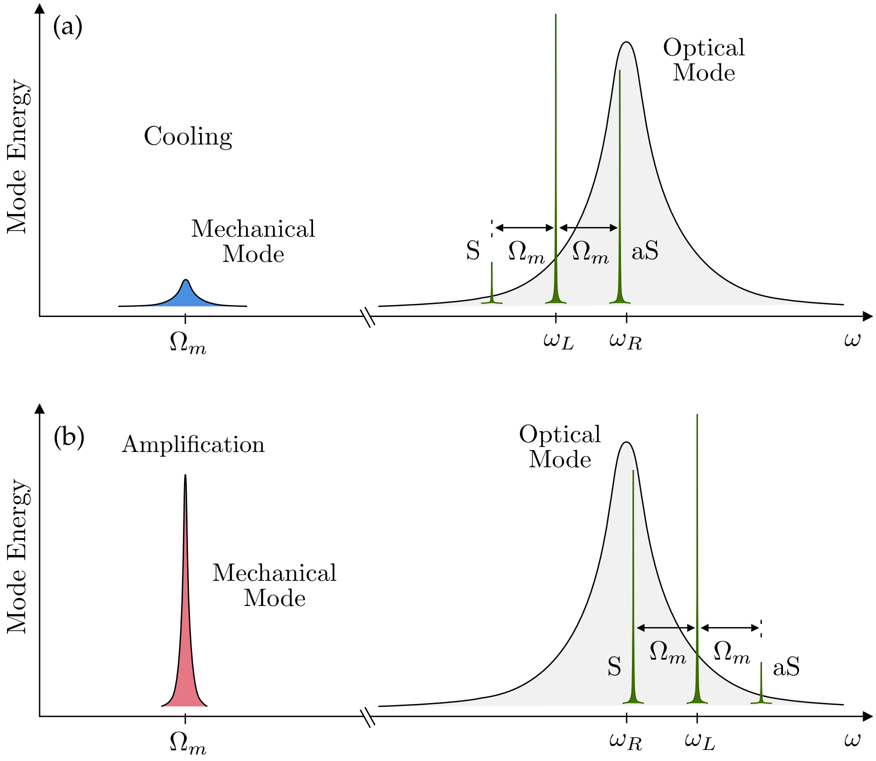

Figure 6.19: Illustration of *cooling* and *amplification* of the mechanical mode. (a) Enhancement of anti-Stokes scattering, (b) Enhancement of Stokes scattering.

It is worth noting that RP and thermal nonlinear phenomena are two mechanisms with different dynamic behaviors. While thermal nonlinearities are induced by absorption and have a dissipative nature, the RP has a reactive character. Moreover, RP is strongly dependent of the optical and mechanical Q-factor: it increases quadratically with the value of the Q-factor. Meanwhile, the thermal nonlinear effects increase more slowly with the Q-factor, thus RP dominates in MRs with high optical and mechanical Q-factors [24].

In addition, let us point out that the generation of optical or optomechanical nonlinear effects is a competitive process. Both effects can coexist, or one of them can be enhanced, leading to the suppression of the other one. It will depend on the power circulating in the MR, the phase-matching condition, the Q-factor of optical and mechanical resonances, and the electromagnetic field distribution of the locked WGM resonance.

The induced RP effects have been observed before in MRs with different geometries: in spheres [25], toroids [26], or microbottles [27]. Many applications have been developed based on the optomechanical interactions and several studies have been carried out [22, 23]: in quantum cavity optomechanics, to measure small forces, masses, or displacements, in gravitational wave detection systems, in phonon lasers, in chaotic dynamics, *etc*. In this work, we will characterize experimentally the optomechanic vibrations induced by RP in bubble MRs. Up to our knowledge, this is the first time such phenomena has been observed for this type of MRs. Besides, we will study the transition of the performance of the excited mechanical modes to a chaotic behavior, when the optical power coupled to the MR is high enough.

(II). Experimental setup

The experimental setup employed is shown in Fig. 6.20. A tunable laser source centered at 1550 nm was amplified with an erbium-doped fiber amplifier (EDFA). A small fraction of the launched signal was monitored to control the input power coupled to the MR. The light is then launched to a 2 µm taper that will excite the WGMs in our MRs. Part of the output signal of the taper was sent to an OSA (20 pm resolution), and part into a fast photodetector, connected either to an oscilloscope, or to an electrical spectrum analyzer (ESA, 9 kHz - 6 GHz).

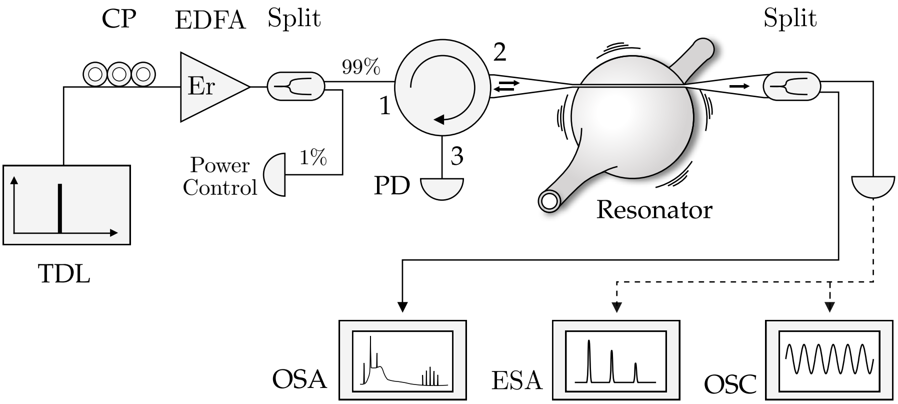

Figure 6.20: Scheme of the experimental setup emloyed to excite and measure the optomechanical vibrations induced by RP.

In this particular experiment, the MRs were silica bubbles fabricated using a technique similar to glassblowing, based on increasing the temperature up to the plastic deformation of the silica, on slightly pressurized silica capillaries [28]. The diameters of the microbubbles employed in this experiment range from 420 to 780 µm, with wall thicknesses from 2 to 6 µm (± 0.5 µm). It is worth noting that the bubble MRs have a non-uniform thickness, with the wall being thinnest at the equator (prolate spheroid). The original commercial capillaries had an external diameter of 200 µm, and a wall thickness of 80 µm. We want to point out that we did not measure the wall thickness of the bubble MRs, but we calculated it by assuming the conservation of the MR mass during the fabrication, and taking into account the capillary and bubble diameters. We measured the WGM resonances at low input powers when nonlinear phenomena were below their threshold, and thermal broadening/narrowing of the resonance was negligible. The different bubble MRs exhibited optical Q-factors around $10^6 - 10^7$. For the measurements of the optomechanics and nonlinear phenomena, the laser was locked to the WGM resonances position by employing the passive thermal locking technique detailed in the previous sections.

(III). Experimental characterization

As we have mentioned, when the laser wavelength is properly locked to a WGM resonance at its blue-edge, and the optical power coupled to the MR is high enough, the mechanical modes of the MR can be excited.

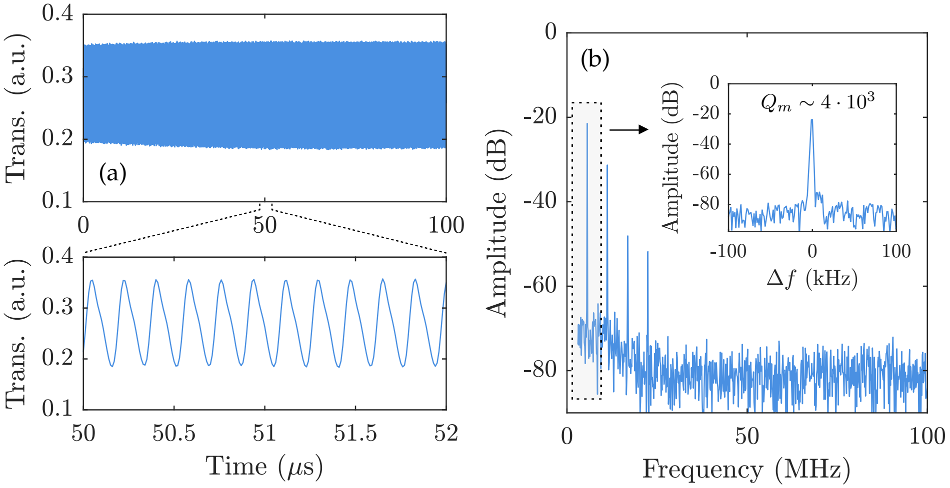

Figure 6.21: (a) Harmonic modulation of the system transmittance due to the optomechanical vibration. (b) Frequency of vibration and mechanical Q-factor.

We analyzed the optical signal as the pump power was increased. At low powers, the signal at the output of the taper remained constant, as it corresponds to a locked resonance. At a given value of the pump, the signal suddenly shows a clear quasi-harmonic oscillation: Fig. 6.21a depicts the optical trace measured by the oscilloscope, for a 200 mW of pump power. Figure 6.21b shows the radio-frequency signal measurement, using the ESA. It can be observed a narrow fundamental vibrational mode centered at 5.63 MHz, which corresponds to a vibrational mode of the bubble MR. We believe that the harmonics present in the measurement can be due to the nonlinear shape of the WGM resonance, see Fig. 6.22b. In the inset of Fig. 6.21b, we show that the excited mechanical mode had a Q-factor around $4 \cdot 10^3$. We studied the temporal stability of the mechanical vibration and obtained that the variations of the fundamental peak amplitude are lower than

1.5 dB over 3 minutes (ESA measurement), and its spectral position remains constant within deviations of 1.3 kHz.

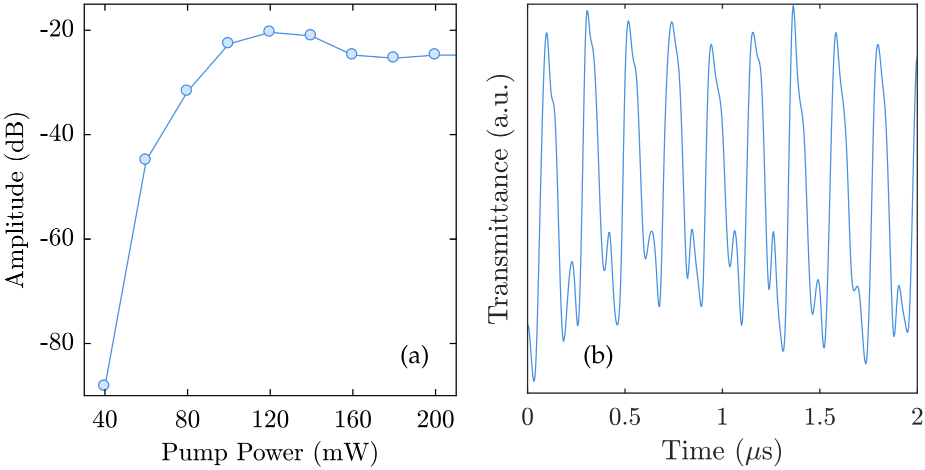

Figure 6.22: (a) Evolution of the fundamental peak amplitude as a function of the pump power. (b) Distortion of the transmittance modulation due to the resonance shape.

We studied the evolution of the amplitude of the fundamental peak observed in the ESA measurement (see Fig. 6.21b), as a function of the pump power. Figure 6.22a shows its peak amplitude evolution. As the pump power is increased beyond the threshold of the mechanical vibration, the amplification of the optomechanic effect is higher and it leads to more intense vibrations. This results in a larger modulation of the optical signal, this is, a higher amplitude of the fundamental peak in Fig. 6.21b. In addition, the number of harmonics and their amplitudes increase as the pump power does. The trend of the amplitude of the fundamental peak in the ESA signal with the optical power shows two main features: (i) there exists a threshold for the launched pump power, $\sim$ 50 mW; (ii) the amplitude of the peak reaches a saturated value around $\sim$ 140 mW of pump power. Beyond this value, the peak does not show an increment. We assume that the saturation can be due to the shape of the notch of the WGM resonance: the edge is linear for small deviations from the central point, but for larger oscillations (this is, larger mechanical amplitudes) it presents distortions from the linear behavior, which results in higher order harmonics of the fundamental frequency in the ESA measurement. Figure 6.22b shows an example of the shape-induced distortion in the optical signal. As it can be observed, the amplitude modulation of the spectral position of the WGM resonance, that is, the shift of the WGM resonant wavelength induced by the vibration of high intensity, is enough to exceed the laser wavelength.

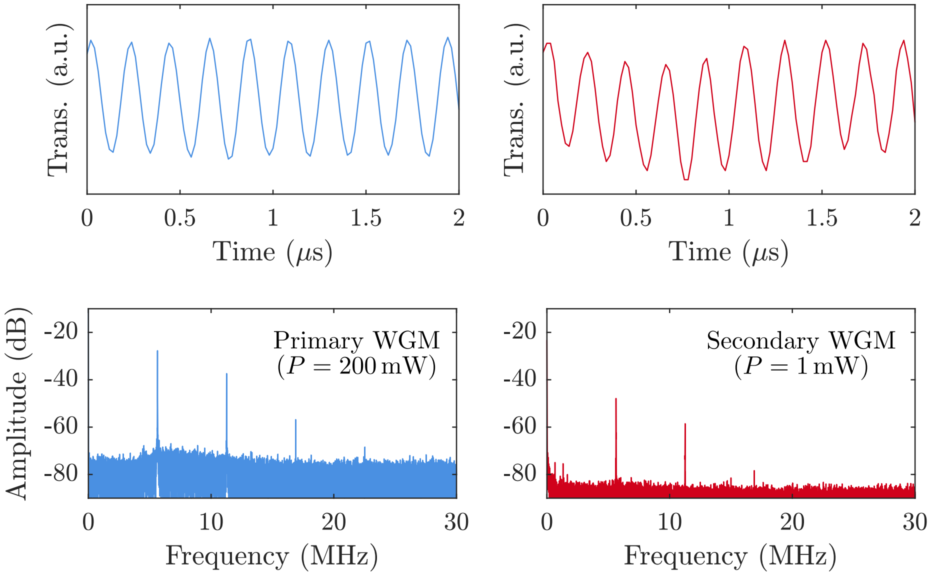

Figure 6.23: Pump and probe measurement of the transmittance modulation induced by the primary WGM ($P = 200\,\mathrm{mW}$).

In order to check that the optical modulation observed in the optical signal was truly due to a mechanical mode of the MR, we excited simultaneously a WGM at a different wavelength in a low power regime. Thus, two contra-propagating WGM were confined in the MR: the primary (high power at $1550\,\mathrm{nm}$), which induces the optomechanical vibrations, and the secondary WGM (low power at $1480\,\mathrm{nm}$), which we used to interrogate the system. This configuration corresponds to a typical pump and probe characterization. The results show that the mechanical modulation induced by the pump (primary WGM) is also suffered by the probe (secondary WGM). This implies that any signal propagating in the MR will be modulated by the mechanical oscillation, since it is caused by the change in the geometry of the MR. Figure 6.23 shows the transmittance modulation of both signals and their respective ESA measurements, the oscillations were induced by the optomechanical vibration due to the primary WGM, and they were simultaneously observed in the secondary WGM optical trace. It should be noted that, since the secondary WGM (probe) is a low power signal, $\sim 1\,\mathrm{mW}$, there are neither optomechanical vibrations induced by this wavelength, nor optical nonlinear effects. Thus, the modulation observed in the oscilloscope trace is due to the changes in the MR induced by the mechanical vibration.

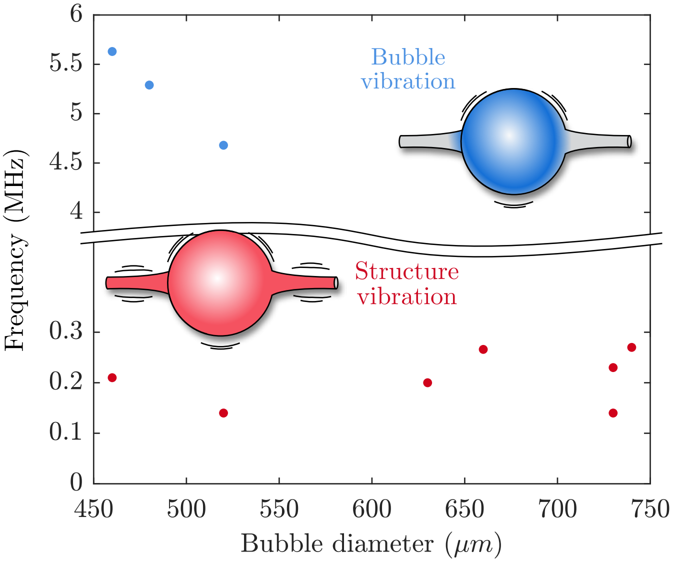

Figure 6.24: Experimental vibrational frequencies as a function of the bubble MR diameter. Illustration of the two types of vibrations that were identified in the two ranges of frequencies.

We performed the same characterization for bubble MRs of different sizes. Figure 6.24 shows the measured vibrational frequencies as a function of the bubble diameter. We identified two different ranges of vibrational frequencies: a high-frequency range (MHz) for microbubbles below 550 μm, and a low-frequency range (kHz), which predominates in larger MRs. First, it can be observed that, in the MHz range, the vibrational frequency decreases as the bubble diameter becomes larger. Meanwhile, in the kHz range, the vibrational frequencies were independent of the MR diameter. Numerical simulations were performed using a finite element method in order to obtain the theoretical vibrational eigenmodes of the microbubbles, to identify which ones were excited. From the results, we concluded that the MHz vibrations are mechanical modes of the microbubble itself, while the kHz vibrations correspond to mechanical modes of the whole structure, the microbubble and the capillary.

The excitation of a certain mechanical mode depends on the overlapping of its mechanical field distribution with the optical field of the WGM. We excited the WGMs of the bubble equator in all the experiments. In this way, we can ensure similar optical field distributions of the WGMs in all the bubbles. Nevertheless, as we mentioned before, when we use the passive thermal locking technique, we do not have control over which specific WGM resonance we are locking. This implies that, the excitation of WGMs with different radial, azimuthal and polar orders is possible. Therefore, more control of the locking process is needed in order to provide a detailed characterization of the excitation of the different mechanical frequencies in bubble MRs. In this sense, the active locking techniques we described in the previous sections would help to achieve such control, thus the development of optomechanics experiments using active locking techniques is worth to study in future works that are beyond the scope of this thesis.

Lastly, we also observed nonlinear phenomena (FWM, Raman, and Brillouin), simultaneously to the optomechanical vibrations even when they are competitive processes. In some cases, the oscillations occur well before other optical nonlinear effects. For certain locking conditions at high launched optical power, we observed an amplification of the vibrations and a suppression of the optical nonlinearities.

(IV). Chaos Transition

As we have mentioned, these type of MRs support both optical and mechanical resonances and, in some conditions, there is a transfer of energy between them. For large optical powers, the acousto-optic interaction excited by the WGMs can behave in a chaotic way. In this section of the work we will show some brief experimental results about the transition to chaos of the optomechanic system. The chaos route in WGM MRs induced by the RP have been reported before [24, 25]. The experiments were performed for different MR geometries to show that the phenomena are not limited to specific MR shape. Here, we will study this phenomena in silica bubble MRs. Up to our knowledge, these are the first experimental results obtained for this type of MRs.

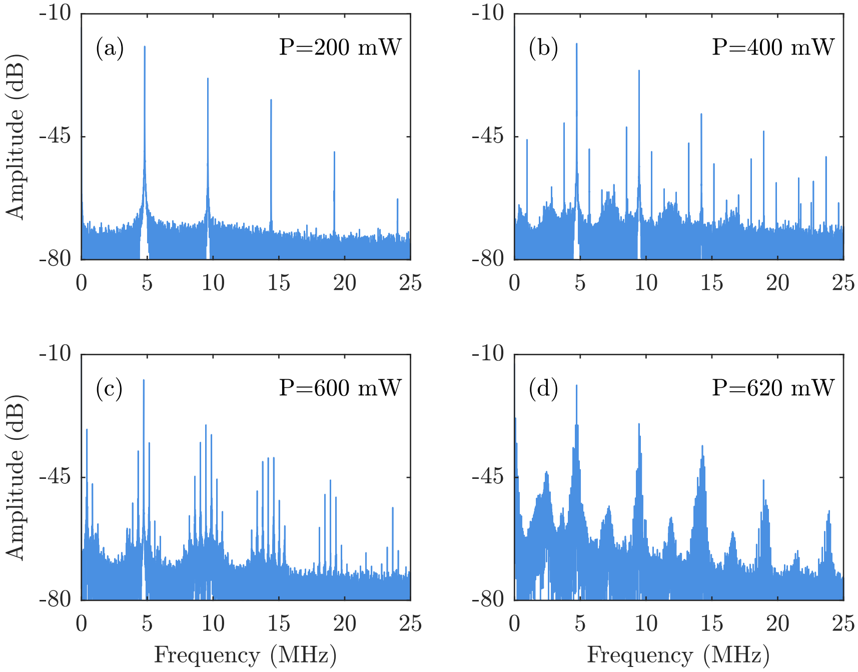

Figure 6.25: Transition to chaos as the launched pump power is increased: (a) 200 mW, (b) 400 mW, (c) 600 mW, (d) 620 mW. Bubble MR of 520 µm diameter and 4.26 µm wall thickness.

The chaos route depicted in Fig. 6.25 was measured for a bubble MR of 520 µm of diameter and wall thickness of 4.26 µm. The fundamental optomechanical mode oscillated at 4.74 MHz, as it can be observed in Fig. 6.25a: a fundamental frequency and a single series of harmonics is observed for 200 mW of pump power. At higher input powers, see Figs. 6.25b and 6.25c, new vibrational frequencies arose in a quasi-period doubling (launched powers of 400 mW and 600 mW). This set of discrete lines developed in a continuum of frequencies when the optical power was increased beyond this point, see Fig. 6.25d. This behavior is characteristic of chaotic systems, and a more detailed study can be found in [25, 29]. Here, we will not characterize this phenomenon in detail, but we find it of interest for further experiments. We measured this route to chaos for bubble MRs of different sizes, and we observed that for the largest ones, this transition to chaos falls directly into the continuum, skipping the sequences of discrete frequencies of quasi-period doubling.

We checked that the optomechanical vibrations, together with their chaos transition, affect not only the confined WGM resonance that excites the mechanical mode, but any WGM propagating in the MR. To do so, we performed two experiments:

(i) We measured the response of the reflected WGM coupled to the mechanical mode for different input powers, and we observed the same type of optical traces showed in Fig. 6.25.

(ii) Additionally, we performed a pump and probe characterization, similarly to the one shown in Fig. 6.23. The results, see Fig. 6.26, depict that both optical traces show the same modulation frequencies and transition to chaos, thus, this modulation is induced by a true mechanical vibration of the MR that is composed by all the frequencies.

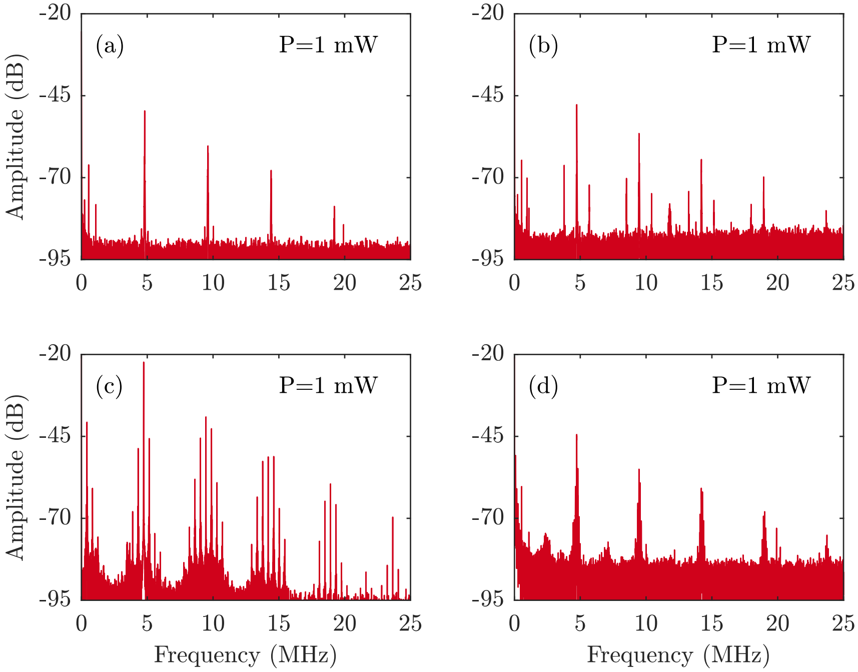

Figure 6.26: Transition to chaos of the probe signal ($P = 1\,\mathrm{mW}$) as the power of the pump signal was increased. Pump power: (a) 200 mW, (b) 400 mW, (c) 600 mW, (d) 620 mW. Bubble MR of 520 μm diameter and 4.26 μm wall thickness.

References

[1] T. J. Kippenberg, S. M. Spillane, and K. J. Vahala. "*Kerr-Nonlinearity Optical Parametric Oscillation in an Ultrahigh-Q Toroid Microcavity*", Physical Review Letters, **93**, p. 083904 (2004).

[2] H.-B. Lin, J. D. Eversole, and A. J. Campillo. "*Continuous-wave stimulated Raman scattering in microdroplets*", Optics Letters, **17**, pp. 828–830 (1992).

[3] Q. Lu, S. Liu, X. Wu, L. Liu, and L. Xu. "*Stimulated Brillouin laser and frequency comb generation in high-Q microbubble resonators*", Optics Letters, **41**, pp. 1736–1739 (2016).

[4] D. Farnesi, A. Barucci, G. C. Righini, S. Berneschi, S. Soria, and G. Nunzi Conti. "*Optical Frequency Conversion in Silica-Whispering-Gallery-Mode Microspherical Resonators*", Physical Review Letters, **112**, p. 093901 (2014).

[5] P. Del'Haye, K. Beha, S. B. Papp, and S. A. Diddams. "*Self-Injection Locking and Phase-Locked States in Microresonator-Based Optical Frequency Combs*", Physical Review Letters, **112**, p. 043905 (2014).

[6] S. Spillane, T. Kippenberg, and K. Vahala. "*Ultralow-Threshold Raman Laser Using a Spherical Dielectric Microcavity*", Nature, **415**, pp. 621–3 (2002).

[7] A. Schliesser, P. Del'Haye, N. Nooshi, K. J. Vahala, and T. J. Kippenberg. "*Radiation Pressure Cooling of a Micromechanical Oscillator Using Dynamical Backaction*", Physical Review Letters, **97**, p. 243905 (2006).

[8] K. J. Vahala. "*Optical microcavities*", Nature, **424**, pp. 839–846 (2003).

[9] V. S. Ilchenko and M. L. Gorodetsky. "*Thermal Nonlinear Effects in Optical Whispering Gallery Microresonators*", Laser Physics, **2**, p. 1004 (1992).

[10] T. Carmon, L. Yang, and K. J. Vahala. "*Dynamical thermal behavior and thermal self-stability of microcavities*", Optics Express, **12**, pp. 4742–4750 (2004).

[11] H. Rokhsari, S. M. Spillane, and K. J. Vahala. "*Loss characterization in microcavities using the thermal bistability effect*", Applied Physics Letters, **85**, pp. 3029–3031 (2004).

[12] F. Vanier, M. Rochette, N. Godbout, and Y.-A. Peter. "*Raman lasing in As2S3 high-Q whispering gallery mode resonators*", Optics Letters, **38**, pp. 4966–4969 (2013).

[13] T. Carmon, T. J. Kippenberg, L. Yang, H. Rokhsari, S. Spillane, and K. J. Vahala. "*Feedback control of ultra-high-Q microcavities: application to micro-Raman lasers and micro-parametric oscillators*", Optics Express, **13**, pp. 3558–3566 (2005).

[14] R. Drever, J. Hall, F. Kowalski, J. Hough, G. Ford, A. Munley, and H. Ward. "*Laser Phase and Frequency Stabilization Using an Optical Resonator*", Applied Physics B, **31**, pp. 97–105 (1983).

[15] L. Stern, I. Goykhman, B. Desiatov, and U. Levy. "*Frequency locked micro disk resonator for real time and precise monitoring of refractive index*", Optics Letters, **37**, pp. 1313–1315 (2012).

[16] P. Merrer, O. Llopis, and G. Cibiel. "*Laser Stabilization on a Fiber Ring Resonator and Application to RF Filtering*", IEEE Photonics Technology Letters, **20**, pp. 1399–1401 (2008).

[17] J. P. Rezac and A. T. Rosenberger. "*Locking a microsphere whispering-gallery mode to a laser*", Optics Express, **8**, pp. 605–610 (2001).

[18] E. Rivera-Pérez, I. L. Villegas, A. Díez, M. V. Andrés, J. L. Cruz, and A. Rodríguez-Cobos. "*Measurement of Pump-Induced Temperature Increase in Doped Fibers Using Whispering-Gallery Modes*", IEEE Photonics Technology Letters, **25**, pp. 2498–2500 (2013).

[19] G. Lin, A. Coillet, and Y. K. Chembo. "*Nonlinear photonics with high-Q whispering-gallery-mode resonators*", Advances in Optics and Photonics, **9**, pp. 828–890 (2017).

[20] G. P. Agrawal. "*Nonlinear fiber optics*", Elsevier Science, Burlington (2013).

[21] D. Farnesi, A. Barucci, G. C. Righini, G. N. Conti, and S. Soria. "*Generation of hyper-parametric oscillations in silica microbubbles*", Optics Letters, **40**, pp. 4508–4511 (2015).

[22] M. Aspelmeyer, T. J. Kippenberg, and F. Marquardt. "*Cavity optomechanics*", Reviews of Modern Physics, **86**, pp. 1391–1452 (2014).

[23] T. Kippenberg and K. Vahala. "*Cavity Opto-Mechanics*", Optics Express, **15**, pp. 17172–17205 (2007).

[24] T. Carmon, H. Rokhsari, L. Yang, T. J. Kippenberg, and K. J. Vahala. "*Temporal Behavior of Radiation-Pressure-Induced Vibrations of an Optical Microcavity Phonon Mode*", Physical Review Letters, **94**, p. 223902 (2005).

[25] T. Carmon, M. C. Cross, and K. J. Vahala. "*Chaotic Quivering of Micron-Scaled On-Chip Resonators Excited by Centrifugal Optical Pressure*", Physical Review Letters, **98**, p. 167203 (2007).

[26] T. J. Kippenberg, H. Rokhsari, T. Carmon, A. Scherer, and K. J. Vahala. "*Analysis of Radiation-Pressure Induced Mechanical Oscillation of an Optical Microcavity*", Physical Review Letters, **95**, p. 033901 (2005).

[27] M. Asano, Y. Takeuchi, W. Chen, Ş. K. Özdemir, R. Ikuta, N. Imoto, L. Yang, and T. Yamamoto. "*Observation of optomechanical coupling in a microbottle resonator*", Laser & Photonics Reviews, **10**, pp. 603–611 (2016).

[28] S. Berneschi, D. Farnesi, F. Cosi, G. N. Conti, S. Pelli, G. C. Righini, and S. Soria. "*High Q silica microbubble resonators fabricated by arc discharge*", Optics Letters, **36**, pp. 3521–3523 (2011).

[29] L. Bakemeier, A. Alvermann, and H. Fehske. "*Route to Chaos in Optomechanics*", Physical Review Letters, **114**, p. 013601 (2015).

7 Conclusions

The study of the WGMs presented in this thesis was organized in two main topics. In the first part, we characterized the strain-optic and thermo-optic effect in different optical fiber devices, by means of the WGMs. This allowed us measuring different parameters of the materials that conformed the MRs, such as strain-optic coefficients, temperature profiles along their lengths, or loss coefficients. A theoretical proposal to characterize the magneto-optic effect in fibers using WGMs was also provided. In the second part, we presented novel locking techniques based on the mentioned strain- and thermo-optic effects, to excite and observe optical and optomechanic nonlinear effects. Within the variety of nonlinear phenomena that can be efficiently excited in WGM-based MRs, we focused on the characterization of optomechanical vibrations in silica microbubbles.

In Chapter 2, we provided a theoretical description of WGMs in cylindrical, anisotropic MRs. We studied the propagation and confinement of WGM resonances in uniaxial, and gyrotropic media. We gave a description of the main features of WGMs that determine their performance: loss sources that can be found in this type of MRs, Q-factor, and the coupling between a microfiber and a MR. This theoretical framework was provided to give a full description of the different effects characterized through this work, and it allowed us to compare our experimental results with theoretical simulations. Based on the analysis developed for uniaxial media, we derived how the response of WGMs was affected by strain and temperature. On the other hand, we presented a theoretical description of the magneto-optical effect in cylindrical MRs with gyrotropic anisotropy. We proposed a possible experimental implementation using different dielectric materials and techniques, although it was not possible to carry out the experiments, due to the lack of materials with a proper Verdet constant.

In Chapter 3, we detailed the general experimental setup used throughout all this thesis work, and the procedures that we carried out to excite and measure the WGM resonances in MRs of different geometries and materials. Besides, the fused-and-pull technique employed for the fabrication of microfibers and cylindrical MRs was also described. We reported the excitation and observation of high Q-factor WGM resonances in silica and polymer MRs. In particular, we showed the implementation of our technique for the excitation of WGMs in conventional optical fibers, and in polymer structures fabricated by a two-photon polymerization method.

In Chapter 4, we studied the strain-optic effect in optical fibers under axial stretch by means of the WGM resonances of the fiber itself. We theoretically described the effect in cylindrical, silica MRs, and predicted that the anisotropy induced by the strain affects differently each polarization, the TE and TM. The simulations showed a strong modal anisotropy: the shift rate for TE modes was ~ 1.7 times the one for TM modes. These simulations were confirmed experimentally by measuring the shift of WGM resonances, showing that the proposed technique enables a direct measurement of the anisotropic behavior induced by the strain. By combining the theoretical description and the experimental technique, we were capable to determine the strain-optic coefficients, p_{11} and p_{12}. Our results for SMF28 fiber were $p_{11} = 0.116$ and $p_{12} = 0.255$ at $1531\,\mathrm{nm}$. We also characterized PMMA fibers and measured their Pockels' coefficients, being $p_{11} = 0.283$ and $p_{12} = 0.282$, at $1550\,\mathrm{nm}$. Both results are in good agreement with the values previously reported. One of the main advantages of the technique is that allows the determination of the dispersion of the strain-optic coefficients. We measured the dispersion of silica for 1064 and $1531\,\mathrm{nm}$, and the dispersion of PMMA from 800

to 2000 nm. In both cases, dispersion was negligible in the studied optical range.

In Chapter 5, we characterized the thermal behavior of different optical fiber devices by exploiting the thermal sensitivity of the WGM resonances; those optical fiber devices were irradiated PS fibers, LPGs, and active fibers doped with rare-earth elements. We provided a theoretical description of the thermo-optic effect in WGM resonances, to show how a temperature variation affects to their spectral position. In all the experiments, the heating of the optical fiber devices was achieved by illuminating the core of the fiber itself with pump signals of moderate power (~ 1 W). Thus, these results are of interest when one considers to use such devices in optical systems that support a considerable amount of optical power, such as cavity lasers.

First, we studied the attenuation losses generated by the UV-irradiation of PS fibers. Our technique, based on measuring the thermal shift of the WGM resonances, allows an accurate, direct characterization of the absorption losses, in addition to the uniformity of the UV-irradiation process, thanks to its low detection limit, $\sim 0.03\,^{\circ}$C. By combining our results with a conventional technique for the measurement of the attenuation, we were able to determine the absorption and scattering contributions to the overall losses separately. We characterized different PS fibers, and observed that the scattering losses increase faster than the absorption ones. One of the main characteristics of the WGM-based technique is its axial resolution, $\sim 200\,\mu$m in fibers, that enables a point to point characterization of the optical fiber device, and the measurement of the losses in a short section of fibers. By exploiting this feature, we were able to detect inhomogeneities produced during the UV-irradiation.

Second, we measured the thermal profile induced by an illuminating signal of moderate power on a LPG. We observed that the heating was not homogeneous along the fiber device, but proportional to the light guided by the fundamental mode of the fiber. The thermal profiles of the LPG under different illumination conditions were measured, and the results show that the gradient is more pronounced as the laser wavelength gets closer to the resonance wavelength ($\sim 4\,^{\circ}$C temperature difference in 5 mm of grating length). These temperature profiles can induce chirps that may affect the spectral properties of the LPGs, in applications were high powers are required.

Finally, we characterized the heating of active fibers doped with different concentrations of Ho and co-doped with Yb, fibers that are employed in the design of all-fiber laser cavities emitting at 2 μm, a hot topic at the moment in the field of fiber lasers. We studied the temperature increment when they were illuminated with pump signals at different wavelengths, 975 and 1125 nm. We showed that the heating for the fibers doped with Ho (11.1 °C and 18.0 °C for 400 mW), in the range of pump powers studied, was in accordance with the concentration ratio of the dopant for each fiber, ~ 1.5. On the other hand, the fiber co-doped with Yb reached temperatures that exceeded 200 °C for the 975 nm pump, temperature that can be critical in practical applications. The information provided by the WGM-based technique can be employed to design new active fibers with different concentration and dopants minimizing the thermal effects.

To conclude, in Chapter 6, we presented the implementation of a passive and two novel active locking techniques to match the laser wavelength to the WGM resonance in order to overcome an undesired detuning between them. This detuning might be due to the nonlinear thermal effects and other spurious instabilities, such as vibrations of the setup. We first described the thermal nonlinearities that appear when the laser and a WGM resonance are spectrally matched. A detailed description and an experimental demonstration of the broadening and narrowing suffered by the WGM resonances was showed. We experimentally implemented a passive locking technique reported in the literature based on the meta-stable equilibrium, which allowed us to study some interesting effects. To implement our active locking techniques, we developed an electronic feedback device that allowed us to perform the locking by correcting and compensating the relative spectral position between the laser and the WGM resonance. The feedback device can be employed, as usual, to correct the laser operational wavelength in order to stabilize the system, but also to control the amount of power coupled to the MR.

Since in many applications a constant operational laser wavelength is preferred, we developed and tested two novel active locking techniques that operate at constant laser wavelength. While the conventional active lockings are centered on tuning the wavelength of the laser that excites the WGM resonances, our approaches consisted on tuning the properties of the MR itself, this is, on tuning the resonance wavelength of the WGMs. The first one was based on the strain-optic effect, by applying an axial stretch to an optical fiber (that played the role of a cylindrical MR), in order to tune the spectral position of the WGM resonances. The second one is based on the thermo-optic effect, by controlling the temperature increment induced by an auxiliary pump source in a doped fiber. The second locking technique is an all-optic one that can be implemented in MRs with different geometries. In this way, it is possible to perform an active locking, and the requirements on the laser system, which is usually one of the most expensive devices, are reduced.

We employed the passive and active pump-locking techniques to excite and observe different optical nonlinear phenomena in spherical, silica MRs: stimulated Raman scattering, four-wave mixing, and stimulated Brillouin scattering. We studied the performance of the nonlinear spectra over the time using passive locking and our active alternatives, and we concluded that our approaches provided more control on the generation of nonlinear phenomena, and more temporal stability of the signal.

By employing techniques to lock WGM resonances, we enabled the existence of high circulating powers located within the MRs. Due to the strong electromagnetic field, optomechanic vibrations can be induced due to radiation pressure. We characterized the vibrational modes excited in bubble MRs of different sizes, by employing a passive locking technique. Up to our knowledge, this is the first time such phenomena is reported in this type of MRs. We observed the coupling between the WGMs and the mechanical modes supported in the MRs, and we identified two series of vibrations of the system: the ones corresponding to the microbubble itself, in the MHz range, and those related to the structure microbubble and capillary, in the kHz range. We also studied the coexistence of optical nonlinear phenomena and the vibrational effects, and we observed that they are competitive phenomena: in some conditions they can coexist, while for some other parameters, optomechanical resonances suppress optical nonlinear effects. Lastly, we characterize the evolution of the vibrational modes and their transition to chaos, as the circulating power increases.

From the theoretical descriptions and the experiments developed in this thesis, different ideas have arose to carry out a variety of experiments as a future work. For example, by employing the experimental technique based on the strain-optic effect, we are able to measure the strain-optic coefficients of novel materials. By employing the experimental technique based on the thermo-optic effect, we are capable to characterize the contribution of the absorption and scattering losses in active doped fibers to optimize their performance. Also, the novel active locking techniques open the path to characterize a great variety of nonlinear phenomena, with a better control on the parameters that determine their spectral response. The experimental generation of light sources at a wide range of wavelengths by exciting different optical nonlinear effects can be achieved now in our experiments, thanks to the advantages of the active locking techniques. Moreover, we can also carry out a more detailed study of optomechanical phenomena in MRs with different geometries.

Publications

Articles in journals

- X. Roselló-Mechó, M. Delgado-Pinar, A. Díez, and M. V. Andrés, *"Measurement of Pockels' coefficients and demonstration of the anisotropy of the elasto-optic effect in optical fibers under axial strain"*, Optics Letters, **41**, 2934-2937 (2016).
- N. B. Tomazio, A. J. G. Otuka, G. F. B. Almeida, X. Roselló-Mechó, M. V. Andrés, and C. R. Mendonça, *"Femtosecond laser fabrication of high-Q whispering gallery mode microresonators via two-photon polymerization"*, Journal of Polymer Science Part B: Polymer Physics, **55**, 569-574 (2017).
- L. Poveda-Wong, J. L. Cruz, M. Delgado- Pinar, X. Roselló-Mechó, A. Díez, and M. V. Andrés, *"Fabrication of long period fiber gratings of subnanometric bandwidth"*, Optics Letters, **42**, 1265-1268 (2017).
- X. Roselló-Mechó, M. Delgado-Pinar, J. L. Cruz, A. Díez, and M. V. Andrés, *"Measurement of UV-induced absorption and scattering losses in photosensitive fibers"*, Optics Letters, **43**, 2897-2900 (2018).
- X. Roselló-Mechó, D. Farnesi, G. Frigenti, A. Barucci, A. Fernández-Bienes, T. Garcia-Fernández, F. Ratto, M. Delgado-Pinar, Miguel V. Andrés, G. Nunzi-Conti, and S. Soria, *"Parametrical Optomechanical Oscillations in PhoXonic Whispering Gallery Mode Resonators"*, Scientific Reports, **9**, 7163 (2019).

- X. Roselló-Mechó, M. Delgado-Pinar, J. L. Cruz, A. Díez, and M. V. Andrés, *"Measurement of PMMA strain-optic coefficients from* 800 *to* 2000 *nm by means of Whispering Gallery Modes"*, In preparation.

- X. Roselló-Mechó, M. Delgado-Pinar, J. L. Cruz, A. Díez, and M. V. Andrés, *"Novel active locking techniques of Whispering Gallery Modes resonances for improving the generation of nonlinear phenomena"*, In preparation.

- X. Roselló-Mechó, D. Farnesi, G. Frigenti, M. Delgado-Pinar, M. V. Andrés, G. Nunzi-Conti, and S. Soria, *"PhoXonic microbubbles: optomechanical route to chaos and chaos transfer"*, In preparation.

Communications to Conferences

Invited Talks

- X. Roselló-Mechó, M. Delgado-Pinar, J.L. Cruz, A. Díez and M.V. Andrés, *"WGM for the measurement of absorption and scattering loss in UV-irradiated photosensitive fibers"*, 5th MC Meeting and 4th Annual Conference of the COST (MP1401 Action), Warsaw, October 2018.

- X. Roselló-Mechó, D. Farnesi, G. Frigenti, A. Barucci, A. Fernández-Bienes, T. Garcia-Fernández, F. Ratto, L. Cavigli, M. Delgado-Pinar, M. V. Andrés, R. Pini, G. Nunzi-Conti, and S. Soria, *"Microbubble resonators as efficient PhoXonic enhancement platforms"*, 21st Photonics North Conference, Quebec, May 2019.

- X. Rosello-Mech, G. Frigenti, M. Delgado-Pinar, M. V. Andrés, G. Righini, G. Nunzi Conti, and S. Soria, *"Optomechanical oscillations in microbubble resonators: Enhancement, suppression and chaotic behaviour"*, 21th International Conference of Transparent Optical Network, Angers, July 2019.

- X. Roselló-Mechó, M. Delgado-Pinar, A. Díez, J. L. Cruz y M. V. Andrés, *"WGM for the measurement of absorption and scattering loss in UV-irradiated photosensitive fibers"*, 8th International Conference on Advanced Optoelectronics and Lasers (CAOL 2019), Sozopol, September 2019.
- X. Roselló–Mechó, D. Farnesi, A. Barucci, G. Frigenti, F. Ratto, M. Delgado-Pinar, M.V. Andrés, S. Pelli, R. Pini, G. Righini, G. Nunzi-Conti, S. Soria, *"Parametrical Optomechanical Oscillations in Microbubble Resonators: Suppression and Enhancement of Nonlinear Phenomena"*, 101° Congresso della Società Italiana di Fisica, Rome, September 2019.

Oral contributions

- N. B. Tomazio, A. J. G. Otuka, G. F. B. Almeida, X. Roselló-Mechó, A. Díez, M. V. Andrés, and C. R. Mendoça, *"Femtosecond laser fabrication of polymeric optical resonators"*, Latin America Optics and Photonics Conference (LAOP 2016), pp. LTh3C.5, Medellín, August 2016.
- X. Roselló-Mechó, M. Delgado-Pinar, A. Díez, J. L. Cruz, and M. V. Andrés, *"Medida de las pérdidas inducidas por radiación UV en fibras fotosensibles"*, XII Reunión Nacional de Óptica (RNO 2018), pp. 209, Castellón, July 2018.
- X. Roselló–Mechó, D. Farnesi, A. Barucci, G. Frigenti, A. Fernández-Bienes, F. Ratto, M. Delgado-Pinar, M. V. Andrés, T. García-Fernández, G. Nunzi-Conti, S. Soria, *"Parametrical Optomechanical Oscillations: transition to chaos"*, IEEE workshop on complexity in engineering (COMPENG 2018), pp. 14-15, Florence, October 2018.
- S. Soria, G. Nunzi-Conti, D. Farnesi, A. Barucci, F. Ratto, G. Frigenti, X. Rosello-Mecho, M. V. Andrés, M. Delgado-Pinar, and G. C. Righini, *"Parametrical optomechanical oscillations in microbubble resonators: Suppression and enhancement of nonlinear phenomena"*, Proc. SPIE 10904, Laser Resonators, Microresonators, and Beam Control XXI, San Francisco, March 2019.

Poster contributions

- X. Roselló-Mechó, M. Delgado-Pinar, A. Díez, and M. V. Andrés, *"Anisotropic Elasto-optic Effect in Optical Fibers under Axial Strain: Experimental Observation by means of Whispering Gallery Modes Resonances"*, Latin America Optics and Photonics Conference (LAOP2014), ISBN: 978-1-55752-825-4, Cancún, November 2014.

- X. Roselló-Mechó, M. Delgado-Pinar, A. Díez, and M. V. Andrés, *"Experimental characterization of the anisotropy of the elasto-optic effect in optical fibers under axial strain"*, Conference on Lasers and Electro-Optics 2015 (CLEO/Europe), pp. CH-p.32, Munich, June 2015.

- X. Roselló-Mechó, M. Delgado-Pinar, A. Díez, and M. V. Andrés, *"Surface Waves Resonances of a Standard Optical Fiber: characterization of the elasto-optic effect"*, Reunión Nacional de Optoelectrónica (OPTOEL 2015), pp. SII-04, Salamanca, July 2015.

- X. Roselló-Mechó, M. Delgado-Pinar, A. Díez, and M. V. Andrés, *"Surface Waves Resonances of a Standard Optical Fiber: characterization of the elastooptic effect"*, International OSA Network of Students (IONS 2015), pp. 70, Valencia, September 2015.

- N. B. Tomazio, X. Roselló-Mechó, A. J. G. Otuka, G. F. B. Almeida, A. Díez, M. V. Andrés, and C. R. Mendoça, *"Femtosecond laser induced two-photon polymerization of whispering gallery mode microresonators"*, Laser Resonators, Microresonators, and Beam Control XVIII, San Francisco, February 2016.

- X. Roselló-Mechó, M. Delgado-Pinar, A. Díez, and M. V. Andrés, *"Anisotropic elasto-optic effect in optical fibers under axial strain: a perturbative approach"*, Latin America Optics and Photonics Conference (LAOP 2016), pp. LTu4A.37, Medellín, August 2016.

- X. Roselló-Mechó, M. Delgado-Pinar, A. Díez, and M. V. Andrés, *"A perturbative approach to the elasto-optic effect in optical fibers under axial strain"*, IEEE 7th International Conference on Advanced Optoelectronics and Lasers (CAOL 2016), pp. 72-74, Odessa, September 2016.

- X. Roselló-Mechó, M. Delgado-Pinar, L. Poveda-Wong, J. L. Cruz, and M.V. Andrés, *"Measurement of thermal profiles in LPGs by using Whispering Gallery Modes Resonances"*, IX Reunión Iberoamericana de Óptica y XII Reunión Iberoamericana de Óptica, Láseres y Aplicaciones (RIAO 2016), pp. 309, Pucón, November 2016.

- X. Roselló-Mechó, M. Delgado-Pinar, L. Poveda-Wong, J.L. Cruz, A. Díez, and M.V. Andrés, *"Thermal effects in LPG generated by moderate power signals"*, Third International Conference on Applications of Optics and Photonics 2017 (AOP), pp. 64, Faro, May 2017.

- L. Poveda-Wong, J.L. Cruz, M. Delgado-Pinar, X. Roselló-Mechó, A. Díez, and M. V. Andrés, *"Long period fiber gratings of subnamometric bandwidth: fabrication with a UV laser"*, Third International Conference on Applications of Optics and Photonics 2017 (AOP), pp. 64-65, Faro, May 2017.

- X. Roselló-Mechó, M. Delgado-Pinar, L. Poveda-Wong, Jose Luis Cruz, A. Díez, and M. V. Andrés, *"Measurement of UV-induced Losses andThermal Effects in Photosensitive Fibers Using Whispering Gallery Modes"*, Conference on Lasers and Electro-Optics 2017 (CLEO/Europe), pp. CH-P.2, Munich, June 2017.

- X. Roselló-Mechó, M. Delgado-Pinar, L. Poveda-Wong, J.L. Cruz, and M. V. Andrés, *"Measurement of UV-induced Losses and Thermal Effects in Photosensitive Fibers Using Whispering Gallery Modes"*, Reunión Nacional de Optoelectrónica (OPTOEL 2017), pp. 64-66, Santiago de Compostela, July 2017.

- L. Poveda-Wong, J.L. Cruz, M. Delgado-Pinar, X. Roselló-Mechó, A. Díez, and M. V. Andrés, *"Subnanometric bandwidth long period gratings in the 1500 nm spectral region"*, Reunión Nacional de Optoelectrónica (OPTOEL 2017), pp. 19-22, Santiago de Compostela, July 2017.
- X. Roselló-Mechó, M. Delgado-Pinar, J.L. Cruz, A. Díez and M.V. Andrés, *"Characterization of UV-induced absorption and scattering losses in photosensitive fibers"*, Latin America Optics and Photonics Conference (LAOP 2018), Lima, November 2018.
- X. Roselló-Mechó, M. Delgado-Pinar, A. Díez, and M. V. Andrés, *"Measurement of PMMA Pockels' coefficients in the near-infrared range by using Whispering Gallery Modes resonances"*, 11ª Reunión Española de Optoelectrónica, Zaragoza, July 2019.

Book publications

- M. Delgado-Pinar, X. Roselló-Mechó, E. Rivera-Pérez, A. Díez, J. L. Cruz, and M. V. Andrés, *Whispering Gallery Modes for accurate characterization of optical fibers parameters", Book: " Applications of Optical Fibre for Sensing"*, InTech - Open Access Publisher, pp. 137-151, (2019). DOI: 10.5772/intechopen.81259